ER13065-535

UR-1059

PRECISION MEASUREMENT OF x, Q^2 AND A-DEPENDENCE OF $R=\sigma_L/\sigma_T$ AND F_2 IN DEEP INELASTIC SCATTERING"

BY

S. R. DASU

THE UNIVERSITY OF ROCHESTER

DEPARTMENT OF PHYSICS AND ASTRONOMY

ROCHESTER , NEW YORK

PRECISION MEASUREMENT OF x, Q^2 AND A-DEPENDENCE OF $R=\sigma_L/\sigma_T$ AND F_2 IN DEEP INELASTIC SCATTERING

by

Sridhara Rao Dasu

Submitted in Partial Fulfillment
of the
Requirements for the degree
DOCTOR OF PHILOSOPHY

Supervised by Professor Arie Bodek
Department of Physics and Astronomy
The University of Rochester

April 14, 1988

VITAE

The author was born on November 25, 1961, in Hyderabad, India. He received a B. Sc. degree in Physical Sciences from the Osmania University in 1981. He was awarded a M. Sc. degree in Physics by the University of Hyderabad in 1983. He began graduate studies in the Department of Physics and Astronomy of the University of Rochester in the Fall of 1983. During his tenure at University of Rochester, he has been employed as a teaching assistant, and as a research assistant working on the Experiment E140 at the Stanford Linear Accelerator Center. In the summer of 1987 he was awarded the David Dexter Prize of the Department of Physics and Astronomy. His thesis advisor has been Professor Arie Bodek.

ACKNOWLEDGMENTS

The experiment reported in this thesis is a collaborative effort of thirty physicists from The American University, California Institute of Technology, Fermi National Accelerator Laboratory, Lawrence Livermore National Laboratory, University of Massachusetts, Stanford Linear Accelerator Center, Stanford University and the University of Tel-Aviv. I am grateful to the members of this group for their dedication and outstanding efforts in building the detector components, and in obtaining the data sample used in this analysis. I acknowledge the support of the SLAC staff whose technical assistance was crucial to the success of this experiment.

I owe special thanks to Professor Steve Rock of American University, who invested many hours overseeing my analysis efforts, and offering invaluable advice. I wish to thank my fellow members of the University of Rochester group, Mr. Pawel de Barbaro and Dr. Karol Lang, whose efforts were especially crucial in setting up the analysis program of this experiment. The toroid calibration and other results of Mr. Robert Walker, and the floating wire results of Ms. Lisa Clogher are highly appreciated. I am indebted to another member of our University of Rochester group, Dr. Witek Krasny, for his work on radiative corrections, and theoretical calculations. I am grateful to Dr. Y. S. Tsai for valuable discussions about radiative corrections. I also wish to thank Dr. J. G. Gomez for providing me with data obtained in the SLAC experiment E139.

I am most grateful to Professor Arie Bodek for his invaluable guidance, constructive criticism, and constant encouragement, which have not only made this thesis possible, but also enabled me to learn the art of High Energy Physics in this short span of 3 years. As my closest collaborator, he has made the many long hours spent on this project fruitful and enjoyable.

It is a pleasure to thank Ms. Betty Cook, Mr. Ovide Corriveau, Ms. Pat Fitzpatrick, Ms. Lynn Hanlon, Ms. Connie Jones, Mr. Eric Jones, and Ms. Judy Mack for their assistance during my tenure both at Rochester and SLAC.

Finally, I wish to thank my parents, and my wife to whom I dedicate this thesis.

This research was supported by Department of Energy Contracts No. DE-AC02-76ER13065, No. DE-AC02-76ER02853, No. DE-AC03-96SF00515 and W-7405-ENG-48; and National Science Foundation Contracts No. PHY84-10549 and PHY85-05682.

ABSTRACT

We report on results for the quantities: the ratio $R=\sigma_L/\sigma_T$ of the longitudinal (σ_L) and transverse (σ_T) virtual photon absorption cross section, the structure function F_2, the difference R^A-R^D, and the cross section ratio σ^A/σ^D, measured in deep inelastic electron scattering from targets of deuterium, iron and gold.

The results for R obtained at x=0.2, 0.35 and 0.5 show a clear falloff with increasing Q^2, in the range $1 \le Q^2 \le 10$ GeV^2. The x and Q^2 dependence of the quantity R, and the scaling behavior of F_2 are inconsistent with the naive parton model, and the perturbative Quantum Chromodynamics predictions. However, when the effects due to target mass à la Georgi and Politzer are included with the QCD predictions the results are in good agreement. The possible spin-0 diquark content of the nucleons, and any large effects from higher twist terms, beyond those from kinematic target mass effects, are therefore not required to explain our data.

The results on the differences R^A-R^D are consistent with zero, and are in agreement with the models for the EMC effect, including those based on Quantum Chromodynamics, which predict negligible difference. These results indicate that there are no significant spin-0 constituents or higher twist effects in nuclei as compared to free nucleons. The EMC effect is confirmed with very small errors and all data (electron and muon scattering) are now in agreement. Our results indicate that this effect is due to a non-trivial difference in the quark distributions between heavy nuclei and the deuteron.

TABLE OF CONTENTS

LIST OF TABLES

LIST OF FIGURES

I. INTRODUCTION AND MOTIVATION

A. Deep inelastic scattering

The world of elementary particles is now described quite successfully by what is termed as the "Standard Model". For example, the excellent agreement between Quantum Electrodynamics (QED) calculations for g-2 and precision measurements of g-2 for electrons and muons, the successful unification of the weak and electromagnetic interactions within a single theory that contains massive vector bosons and their subsequent discovery, and the qualitative predictions of the gauge theory of strong interactions that are in agreement with experiment, all support the varacity of the Standard Model. While the success of QED might be termed phenomenal, the non-abelian gauge theories describing weak and strong interactions require additional testing.

In particular, Quantum Chromodynamics (QCD), which describes the realm of strong forces between quarks and gluons, is plagued with computational difficulties, and is difficult to confirm in an unambiguous manner. In agreement with the expectation of a color confinement phase in QCD, searches for free colored quarks have failed. This observation supports the notion that the normal phase of hadronic matter is composed of only colorless composites of quarks and gluons (e.g., the hadrons). Crucial tests of the Standard Model, and searches for new physics phenomena, require that we understand the structure of these complex bound states, i.e. the proton and the neutron, in terms of quarks. The initial discovery of asymptotic freedom, i.e. the decrease of the strong coupling constant α_s with increasing momentum transfer squared (Q^2) has made it possible to turn to perturbative QCD calculations for guidance in dealing with hadronic phenomena. The ability to evolve the structure functions of nucleons measured at low Q^2 to higher Q^2 values, has been extremely useful in the interpretation of experimental results from hadron colliders. Additional measurements are needed to verify predictions of QCD, and to derive conclusions from upcoming experiments. Also further experimentation is needed, to gain a more complete understanding of the nuclear structure, in particular to ascertain the role of quarks and gluons in such a complex medium of bound nucleons.

The electron, the muon and their neutrinos, have proved to be effective tools to probe the structure of nucleons. In the process of electron-nucleon scattering, the leptonic part of the interaction can be calculated accurately within the framework of Quantum Electrodynamics (QED), and hence the results can be unambiguously interpreted in terms of the structure of the probed nucleons. The early elastic electron-nucleon scattering experiments [I.1], for instance, have shown that nucleons have finite size, and electric and magnetic moments, and that nucleon form factors fall rapidly with increasing momentum transfer, suggesting a composite picture of the nucleon. The early deep inelastic electron-proton, electron-deuteron scattering experiments [I.2] at the Stanford Linear Accelerator Center (SLAC) suggested that nucleons were indeed made of point-like spin 1/2 constituents. These "partons" were eventually identified as quarks.

The approximate scaling of the proton structure functions, verified by a large angle inelastic e-p experiment [I.3] in the region of momentum and energy transfers significantly greater than the proton mass, provided the most straightforward and convincing evidence for this hypothesis.

There are two structure functions F_1 and F_2 which parameterize the hadronic vertex in a deep inelastic electron-nucleon collision. The separation of the structure functions from the cross section measurements requires precise knowledge of the quantity R, the ratio of the longitudinal and transverse virtual photon absorption cross sections. In addition to testing the predictions of QCD for R, a measurement of the kinematic dependence of R also reduces errors on structure function data accumulated in previous SLAC experiments. The purpose of the experiment, described in this thesis, was to measure R to a good precision. The values of F_1 and F_2 extracted in this experiment are also compared with the calculations of scaling violations within the framework of QCD. The ideal choice for such measurements was to use the electron beams at SLAC and the 8-GeV spectrometer.

The recent discovery [I.4] of the difference in the cross sections for lepton-deuterium and lepton-iron scattering, known as the EMC effect, has sparked considerable activity in the study of deep inelastic scattering from nuclear targets. The difference $R^A - R^D$, and the cross section ratio σ^A/σ^D are also discussed in this thesis.

B. Kinematics

In this deep inelastic scattering experiment (SLAC E140), unpolarized electrons of energy E impinged on a nuclear target. The scattered electrons of energy E' were detected by a spectrometer set at an angle θ. In the first Born approximation, such a process (see Fig. I.1) occurs through the exchange of a single virtual photon of energy $\nu = E - E'$ with invariant four-momentum transfer squared $q^2 = -Q^2 = -4EE'\sin^2\theta/2$ (mass of electron has been neglected). The hadronic final state is unknown except for its invariant mass squared $W^2 = M^2 + 2M\nu - Q^2$, where M is the mass of proton. When the hadronic part of the matrix element is parameterized in terms of two structure functions W_1 and W_2, the differential cross section for this process can be written as,

$$d^2\sigma/d\Omega dE' = \sigma_M\,[W_2(\nu,Q^2) + 2W_1(\nu,Q^2)\tan^2\theta/2], \qquad \text{(I.1)}$$

where $\sigma_M = (4\alpha^2 E'/Q^4)\cos^2\theta/2$.

Alternatively, one could view this process as virtual photon absorption. Unlike the real photon, the virtual photon can have two modes of polarization. In terms of the cross section for the absorption of transverse (σ_T) and longitudinal (σ_L) virtual photons, the differential cross section can be written as,

$$d^2\sigma/d\Omega dE' = \Gamma\,[\sigma_T(\nu,Q^2) + \epsilon\,\sigma(\nu,Q^2)], \qquad \text{(I.2)}$$

where,

$$\Gamma = \frac{\alpha}{4\pi^2}\,\frac{KE'}{Q^2E}\left(\frac{2}{1-\epsilon}\right),\quad \epsilon = \left[1+2(1+\nu^2/Q^2)\tan^2(\theta/2)\right]^{-1},\ \text{and}\ K = \frac{W^2-M^2}{2M}.$$

The quantities Γ and ϵ represent the flux and the degree of longitudinal polarization of the virtual photons respectively. The quantity R, is defined as the ratio σ_L/σ_T, and is related to the structure functions by,

$$R(\nu^2,Q^2) = \frac{\sigma_L}{\sigma_T} = \frac{W_2}{W_1}\left(1+\frac{\nu^2}{Q^2}\right)-1. \qquad (I.3)$$

R can also be written in terms of dimensionless combinations $x=Q^2/(2M\nu)$, $F_1=MW_1$, $F_2=\nu W_2$ and $F_L=F_2-2xF_1+(4M^2x^2/Q^2)F_2$ (the longitudinal structure function) as,

$$R(x,Q^2) = \frac{F_2}{2xF_1}\left(1+\frac{4M^2x^2}{Q^2}\right)-1 = \frac{F_L}{2xF_1}. \qquad (I.4)$$

C. Kinematic dependence of $R(x,Q^2)$

In the naive parton model [I.5], the proton is regarded as a collection of N free partons, each carrying a momentum fraction x_i ($i=1,2,\ldots,N$) of the longitudinal momentum of the proton. If, at high Q^2, the mass of the partons and the interactions amongst partons are neglected, the structure functions are given by the incoherent sum of point particle (photon-parton scattering) contributions, and therefore F_1 and F_2 are functions of $x=Q^2/(2M\nu)$ alone (the Bjorken scaling). The quantity x represents the momentum fraction carried by the struck parton. In this model Callan-Gross relation, i.e. $F_2=2xF_1$, holds. The structure functions are given by $F_2=2xF_1=\sum_i e_i^2\, q_i(x)$, where e_i and $q_i(x)$ are parton electric charge, and momentum distribution function respectively. If the partons are spin-1/2, R can be written as [I.5],

$$R(x,Q^2) = \frac{4M^2x^2}{Q^2}. \qquad (I.5)$$

Whereas, when the partons are spin-0, the transverse virtual photon absorption cross section is zero, and R is infinity. In a more realistic model when the effects due to the finite transverse momentum p_t and mass of the partons (parameterized in Δ), are included the result for R is [I.5],

$$R(x,Q^2) = \frac{4(M^2x^2+p_t^2-\Delta^2)}{(Q^2+p_t^2)}. \qquad (I.6)$$

Therefore, R is a sensitive measure of the spin and the transverse momentum of the nucleon constituents, and mass scales involved in the hadronic matter.

Experimentally it was observed that the Bjorken scaling is not realized exactly, i.e. there was a weak Q^2 dependence of the structure functions, in the SLAC Q^2-range ($1 \le Q^2 \le 20$ GeV^2). The importance mass scales in hadronic matter (e.g. the target hadron mass, the masses of hadronic constituents, the interaction mass scale, and the non-perturbative mass scales expressing the "size" of hadrons) was apparent. The existence of mass scales signifies a breakdown in the scaling of structure functions. The non-perturbative mass scales expressing the size of hadrons of (~1 fm) are typically around 200 MeV, and the valence quark masses are even smaller, and therefore the breakdown of scaling in SLAC Q^2 range of 1-20 GeV^2 is not due to these effects. The advent of the non-abelian gauge theory of strong interactions, Quantum Chromodynamics (QCD), enabled calculation of interaction effects. The discovery of asymptotic freedom, i.e. the logarithmic fall of coupling constant α_s with Q^2, was crucial in establishing that the perturbative calculations within QCD are possible. The perturbative QCD calculations predict [I.6] that scaling is violated logarithmically in Q^2. The target hadron mass (M=0.938 GeV) effects are proportional to M^2/Q^2, and are significant at SLAC values of Q^2 even in the context of naive parton model(see equation (I.5)). However, it was observed that modified scaling variables including M^2/Q^2 term, for example ω' variable [I.7], restored scaling of the structure function F_2. The correct scaling variable including the complete energy-momentum conservation and the target recoil is given by the Nachtman variable ξ [I.8],

$$\xi = \frac{2x}{1+\sqrt{(1+4M^2x^2/Q^2)}}. \qquad (I.7)$$

The kinematic target mass corrections to the quark-parton model structure functions [I.9] were first calculated in the framework of free field operator-product expansion formalism by Georgi and Politzer (GP). The QCD and target mass effect contributions to R are described in detail in Chapter IV and Appendix D. These calculations of R at x=0.5 as a function of Q^2, and at Q^2=10 GeV^2 as a function of x are shown in Figs. I.2a,b. The x and Q^2 dependence of $R(x,Q^2)$, calculated within the framework of QCD, and in QCD including the GP target mass effects, is shown in Figs. I.3a,b and I.4a,b. The quark-gluon interaction effects are important at low values of x when the sea quarks and gluons dominate, whereas the GP target mass effects are

important at large values of x where the valence quarks dominate. An accuracy of 0.03-0.06 on the R data enables testing of the validity of these calculations.

Whether the quark interactions within the nucleons, when probed at a Q^2 of few GeV^2, are dominated by perturbative or non-perturbative QCD contributions is still an open question. Various groups [I.10] have addressed this question, and have come up with models where non-perturbative effects, in particular those due to diquark formation, dominate at low Q^2 ($Q^2 \approx 10$GeV^2). The formation of tightly bound spin-0 diquark, contributes significantly to R, particularly at large values of x.

Therefore, a precision measurement of kinematic dependence of $R(x,Q^2)$ provides a crucial test of QCD. In addition, good knowledge of $R(x,Q^2)$ reduces the uncertainty on the structure functions measured in earlier SLAC experiments.

D. The EMC effect

The recent experimental discovery of the difference in structure functions for iron and deuterium (see Fig. I.5), dubbed the EMC effect [I.4], has caused considerable activity in the area of deep inelastic scattering from nuclear targets. That F_2^{Fe}/F_2^D is different from unity was quickly confirmed by the reanalysis of old MIT-SLAC data [I.11], comparing deuterium and the steel empty target cross sections, and by further experimentation at SLAC for various other targets in experiment E139 [I.12]. The BCDMS muon scattering data [I.13] also confirmed this effect. All these experiments have reported that the ratio F_2^{Fe}/F_2^D decreases to values smaller than unity at x values larger than 0.3, eventually increasing at large values of x due to fermi momentum of the nucleons in nuclei. However, at low x the picture was not as clear, because the SLAC experiments reported values for the ratio which were consistent with unity where as the EMC results [I.14] showed an increase at small values of x (see Fig. I.5). This nagging discrepancy has caused much theoretical speculation.

On the theoretical front, numerous explanations for EMC effect have been proposed. It was the first time that the interplay between the quark-gluon degrees of freedom and those of the nucleus were observed clearly. Consequently explanations based on a variety of hypotheses, some invoking the details of the QCD confinement scales and others based purely on the conventional nuclear physics were proposed [I.15]. Some of these models[I.16] predict a large $R^A - R^D$ (≈ 0.15) whereas others [I.17] including those based on QCD predict negligible difference. Although all these models explain the fall in the EMC ratio of structure functions at moderate x ($0.3<x<0.7$), they differ considerably in the predictions for $x<0.3$ and on the predictions for Q^2 dependence. Therefore studies of the differences in R for heavy nuclei versus deuterium, and the studies of low x-region and the Q^2 dependence for the ratio F_2^{Fe}/F_2^D are needed to identify the correct model.

E. Experimental Status

The measurement of R poses special experimental difficulties as one needs precision knowledge of cross sections over a range of ϵ values at each x and Q^2. Therefore, one needs to plan the experiment specially to enable accurate cross section measurements at a variety of kinematics. However, most results on R [I.2-3,I.18-19] in deep inelastic region have been byproducts of experiments which were designed to concentrate on other aspects of structure functions, (e.g. $F_2(x,Q^2)$, F_2^n/F_2^p, A-dependence of F_2). These experiments did not have sufficient range in ϵ (or equivalently in angle), and also in some cases cross sections were obtained using different spectrometers and detectors, which introduced additional normalization errors.

The early SLAC results [I.2,3] that R was about 0.2 supported the idea that electrons were scattering from spin-1/2 constituents and provided evidence against vector meson dominance models which predicted large values for R that increase with Q^2. The second generation of deep inelastic experiments [I.18,19] at SLAC have revealed a weak kinematic variation in R and supporting the idea that partons were spin-1/2, but could not rule out a small spin-0 contribution due to large uncertainty in the measurement. The results from that analysis of SLAC experiments E49B and E87 [I.18] are plotted in Fig. I.5. Both the experiments used the 8 GeV/c spectrometer, but were done at different times using different targets. These data were augmented by the data taken in the experiment E49A, which used the 20 GeV/c spectrometer. The typical systematic error on these measurements is about 0.07 but varies from 0.03 to 0.23. The results from the experiment E89 [I.19], which used both the 1.6 GeV/c and 20 GeV/c spectrometers, are also plotted on Fig. I.5. These data include possible normalization errors in the systematic error only. The normalization errors dominate the systematic error of 0.1. These SLAC results on R were not precise enough to test the QCD based theoretical predictions for the x and Q^2 dependence, due to large statistical and systematic errors on the data.

In connection with the low x discrepancy between the EMC and SLAC σ^{Fe}/σ^{D} data, the models predicting differences in R for Fe and D_2 were proposed. With the assumption that R is same for Fe and D_2 the ratio of differential cross sections is the same as the ratio of structure functions. However, if R is different for Fe and D_2 the effect is more pronounced for the SLAC data, compared to the CERN data, on the ratio F_2^{Fe}/F_2^{D}, because (a) SLAC cross section measurements were obtained at lower ϵ compared to CERN measurements, and (b) at SLAC values of Q^2 the values of R are known to be larger than zero, whereas at CERN values of Q^2 they are essentially negligible. In fact with an assumption that the difference $R^{Fe}-R^{D}=0.15$ the SLAC data agrees with EMC data (see Fig. I.6) [I.20]. The results from the SLAC experiment E139 have hinted that such an A dependence of R was possible, although the data are clouded by the large errors.

F. Summary

The motivation for precision deep inelastic scattering

measurements at SLAC were three fold. First, there was no earlier experiment specially tuned to measure R, and therefore the errors on available R data were rather large. With the addition of recent high statistics muon and neutrino data to the SLAC electron data, one of the large errors left on the separation of structure functions F_1 and F_2 was due to R. Secondly, the precision measurement of R and its kinematic dependence is a good test of Quantum chromodynamics. These QCD contributions are rather small and therefore a precision measurement was necessary to observe any deviations from QCD. The large values for R reported by earlier experiments in the SLAC Q^2-range, although clouded by large errors, have caused speculations about significant spin-0 (e.g. diquark) content for the nucleons, and large primordial transverse momentum for quarks. The importance of higher twist terms was needed to be understood. Third, further experimentation was necessary for the understanding of EMC effect. In particular, a measurement of $R^{Fe}-R^{D}$ could determine the relative abundance of spin-0 clusters in Fe compared to D_2, and thereby discriminate between various models of EMC effect. A clarification of the experimental discrepancy between the EMC and SLAC measurements of σ^{Fe}/σ^{D} was needed. SLAC experiment E140 was designed and executed with the intention of answering these questions. The cross section data obtained at various x and Q^2 values, and ϵ-ranges listed in Table I.I, enabled a measurement of R accurate to ±0.04 (statistical error) and ±0.04 (systematic error). In addition precision results for the structure functions F_1 and F_2, the differences $R^{A}-R^{D}$, and the ratios F_2^{A}/F_2^{D} were obtained.

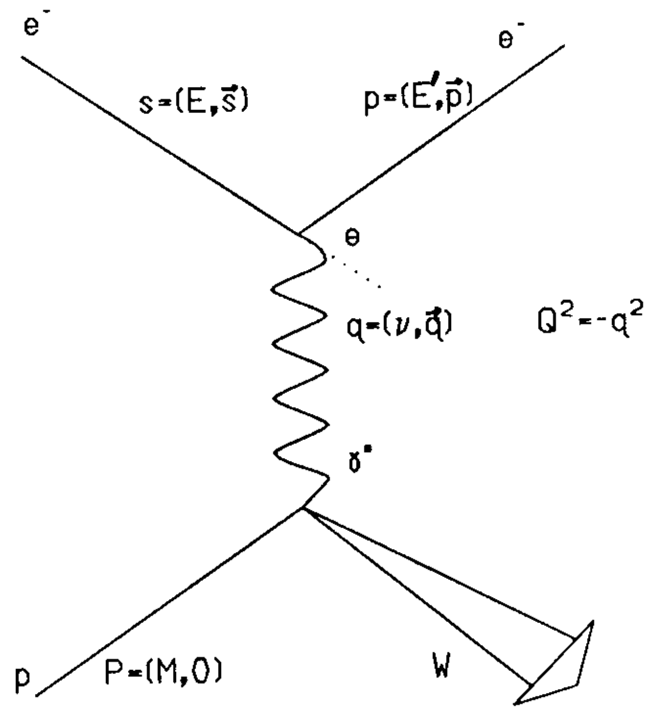

I.1 The Feynman diagram for deep inelastic electron-nucleon scattering in the first Born approximation is shown along with the notation used for kinematic variables.

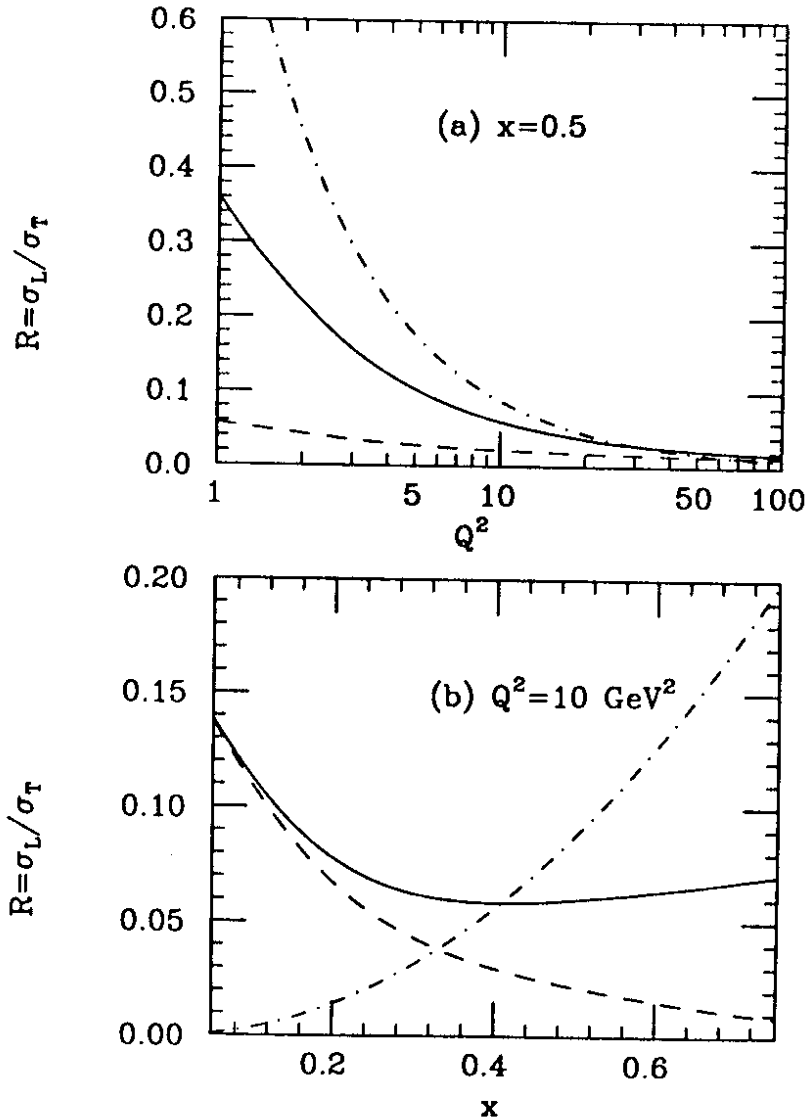

I.2 The theoretical predictions for R are plotted versus (a) Q^2 and (b) x at fixed x=0.5 and Q^2=10 GeV^2 respectively. The dot-dash curve is the prediction from naive parton model, the dash curve is the perturbative QCD prediction and the solid curve is the QCD prediction including the target mass effects.

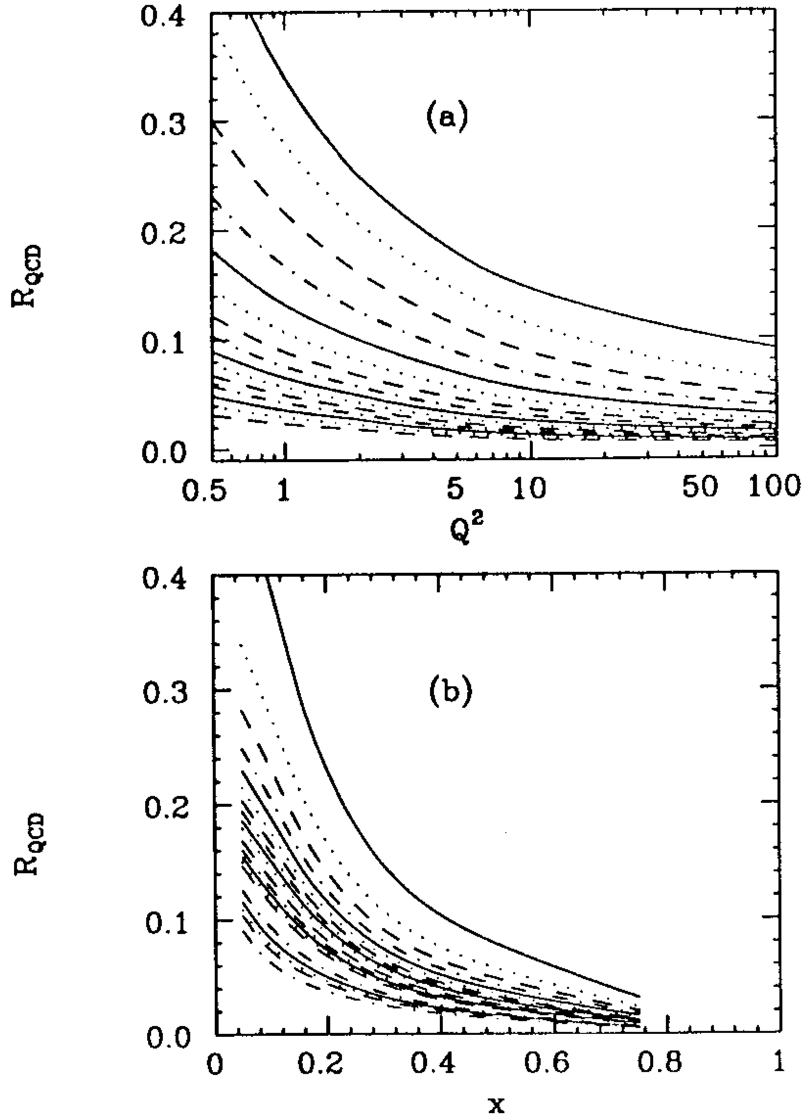

I.3 The perturbative QCD predictions for R to the order α_s are shown (a) at different x in the range $0.05 \leq x \leq 0.75$ as a function of Q^2, and (b) at different Q^2 in the range $0.5 \leq Q^2 \leq 100$ GeV^2 as a function of x.

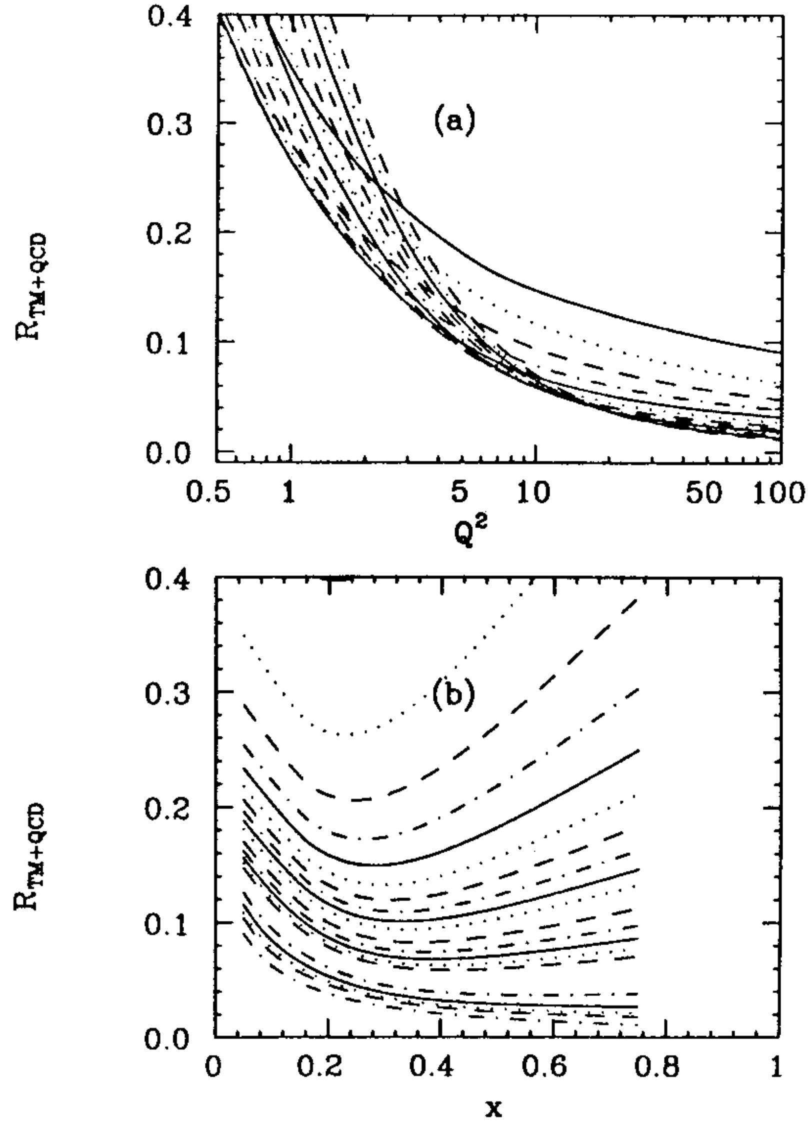

I.4 The predictions for R calculated in the framework of perturbative QCD including the target mass corrections, are shown (a) at different x in the range $0.05 \leq x \leq 0.75$ as a function of Q^2, and (b) at different Q^2 in the range $0.5 \leq Q^2 \leq 100$ GeV^2 as a function of x.

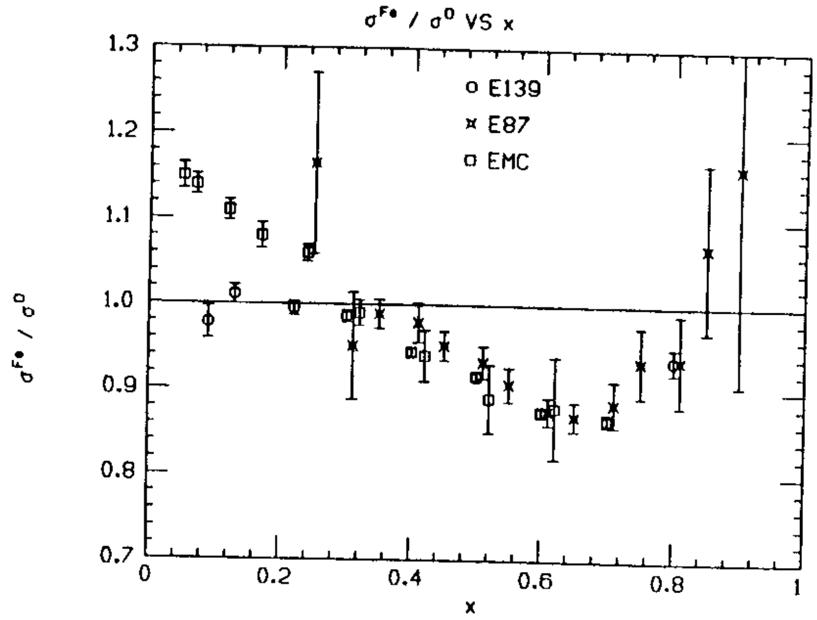

I.5 The EMC effect data as of Jan 1986; The differential cross section ratio σ^{Fe}/σ^{D} is plotted as function of x. The data are from SLAC experiments E139 and E87, and the original data from EMC. At x less than 0.2 there is an apparent disagreement between these data. The EMC data are from J. J. Aubert et al. (1983). The new EMC data (1986) are in better agreement with SLAC data

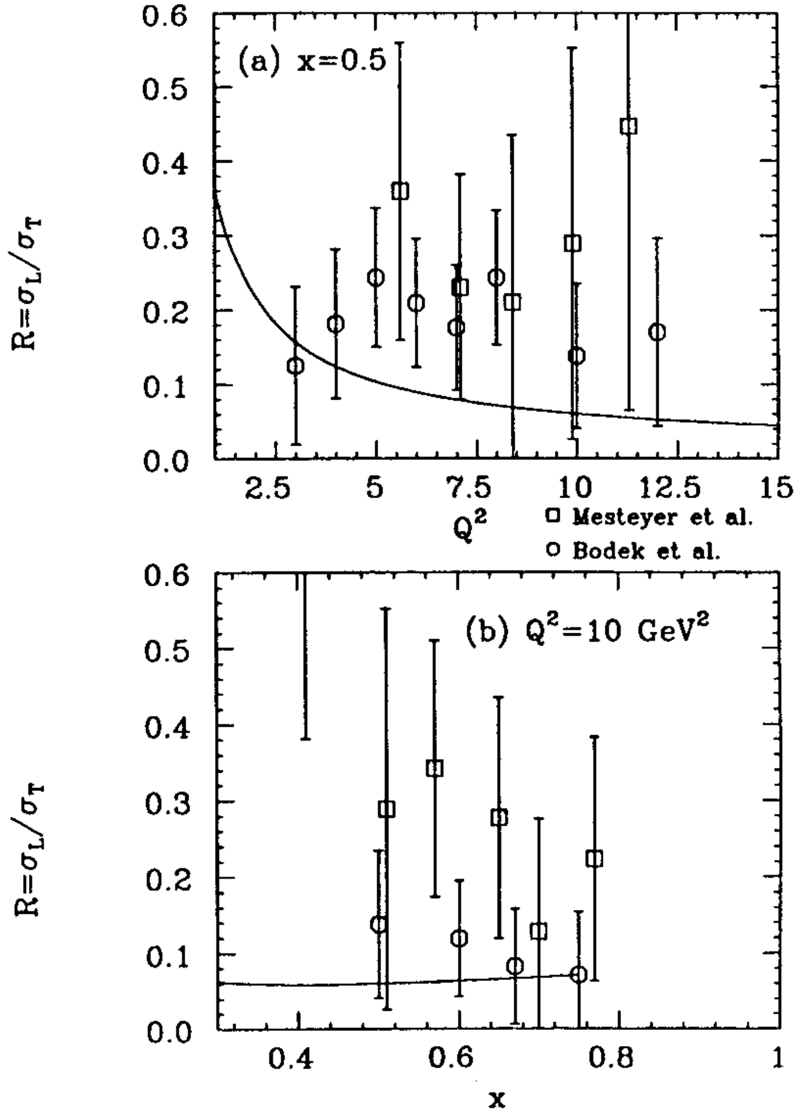

I.6 A sample of pre-E140 SLAC data on R (a) at x=0.5 and (b) at Q^2=10 GeV^2, is plotted versus Q^2 and x respectively. These data are systematically above the QCD predictions including the target mass effects and is consistent with a constant value of R=0.2.

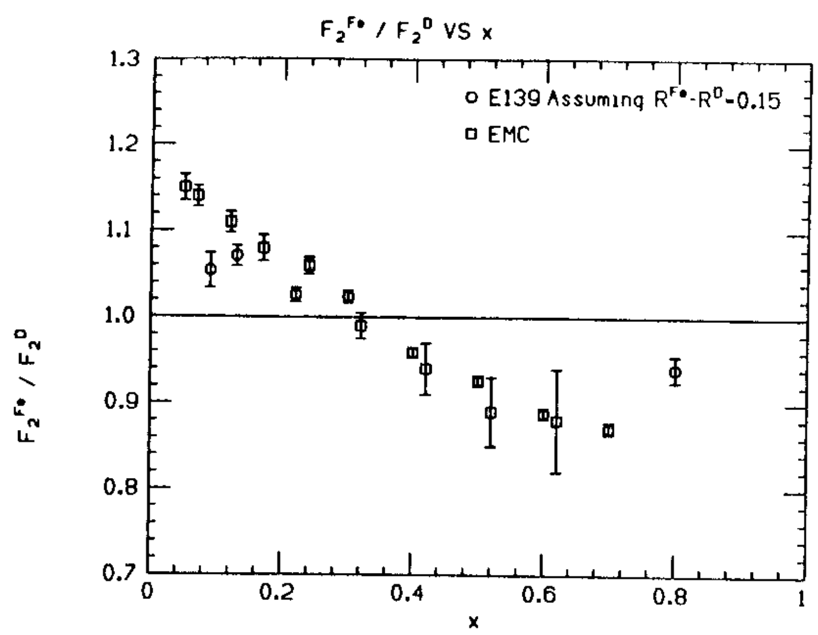

I.7 The cross section ratio data from Fig I.5 are converted to structure function ratio F_2^{Fe}/F_2^D assuming and R difference of $R^{Fe}-R^D=0.15$. The old EMC data are unaffected. The data from SLAC-E139 are then above unity below x of 0.2, in agreement with old EMC data, and therefore the speculation on R being different for heavy nuclei versus D_2.

TABLE I.I

Kinematic range of E140

x	Q^2	No. of ϵ-points	ϵ_{min}	ϵ_{max}	Targets
0.20	1.0	5	0.49	0.85	D_2, Fe(6%), Fe(2.6%), Au
	1.5	5	0.48	0.80	D_2, Fe(6%)
	2.5	3	0.35	0.72	D_2, Fe(6%)
	5.0	4	0.32	0.57	D_2
0.35	1.5	5	0.60	0.84	D_2, Fe(6%)
	2.5	5	0.51	0.87	D_2, Fe(6%)
	5.0	4	0.45	0.78	D_2, Fe(6%)
0.50	2.5	5	0.42	0.93	D_2, Fe(6%), Fe(2.6%)
	5.0	4	0.40	0.86	D_2, Fe(6%)
	7.5	2	0.37	0.74	D_2
	10.0	3	0.35	0.70	D_2

REFERENCES

[I.1] "Electron Scattering and Nuclear and Nucleon Structure", edited by Robert Hofstadter (Benjamin, Menlo Park, California, 1963).

[I.2] E. D. Bloom et al., Phys. Rev. Lett. 23, 930 (1969); M. Breidenbach et al., Phys. Rev. Lett. 23, 935 (1969).

[I.3] G. Miller et al., Phys. Rev. D 5, 528 (1972)

[I.4] J. J. Aubert et al., Phys. Lett. B 123, 275 (1983).

[I.5] R. P. Feynman, "Photon Hadron Interactions", (Benjamin, Menlo Park, California, 1972).

[I.6] G. Altarelli and G. Martinelli, Phys. Lett. B 76, 89 (1978).

[I.7] E. D. Bloom and F. J. Gilman, Phys. Rev. D 4, 2901 (1971).

[I.8] P. H. Frampton, UCLA Preprint UCLA/76/TEP/6 (1976).
O. Nachtmann, Nucl. Phys. B 63, 237 (1973).
H. Georgi and H. D. Politzer, Phys. Rev. Letters 36, 1281 (1976) and erratum 37, 68 (1976).

[I.9] H. Georgi and H. D. Politzer, Phys. Rev. D14, 1829 (1976);
A. De Rujula et al., Ann. Phys. 103, 315 (1977);
R. Barbieri et al., Nucl. Phys. B 117, 50 (1976);
A. J. Buras et al., Nucl. Phys. B 131, 308 (1977);
P. W. Johnson and Wu-Ki Tung, Neutrino '79 Proceedings, Bergen, Norway, (1979).

[I.10] S. Ekelin and S. Fredriksson, Phys. Lett. 162 B, 373 (1985).

[I.11] A. Bodek et al., Phys. Rev. Lett. 50, 1431 (1983); 51, 534 (1983).

[I.12] R. G. Arnold et al., Phys. Rev. Lett. 52, 724 (1984); SLAC-PUB-3257 (1983).

[I.13] G. Bari et al., Phys. Lett. B 163, 282 (1985).

[I.14] The latest results from the EMC collaboration report that the ratio F_2^{Fe}/F_2^D is closer to unity than their old results. See M. Dueren and T. Sloan, Proceedings of the International Europhysics Conference on High Energy Physics (Uppsala, 1987), Editor Olga Botner.

[I.15] E. Berger and F. Coester, Ann. Rev. Nucl. Part. Sci. 37, 463 (1987).

[I.16] Bo-Qiang Ma and Ji Sun, Print-86-1217, Beijing University, China (1986).

[I.17] F. E. Close et al., Phys. Lett. B 129, 346 (1983) - QCD model;
R. D. Smith, Phys. Lett. B 182, 283 (1986) - convolution model.

[I.18] A. Bodek et al., Phys. Rev. D 20, 1471 (1979).

[I.19] M. D. Mesteyer et al., Phys. Rev. D 27, 285 (1983).

[I.20] S. Rock, Proceedings of the XXII International Conference on High Energy Physics, (Leipzig, 1984).
I. A. Savin and G. I. Smirnov, Phys. Lett. 145 B, 438 (1984).

II. THE EXPERIMENT

A. Introduction

The deep inelastic scattering experiment E140 was performed at the Stanford Linear Accelerator Center (SLAC) in the last quarter of 1985. This experiment was specifically designed to measure $R=\sigma_L/\sigma_T$ with a precision of ± 0.03 (statistical) and ± 0.04 (systematic). The extraction of R at any (x,Q^2) point involves measurement of cross sections over a range of ϵ values (i.e. cross sections for different E, E′ and θ settings should be measured). An error of 1% on the cross sections with an ϵ-separation of 0.3, results in an error of 0.03 on R. The difficulty in the measurement of R is due to the dramatic variation of deep-inelastic scattering cross sections and backgrounds in the kinematic range where 1% measurements are needed. The important factors which limited the kinematic range ($0.2 \leq x \leq 0.5$ and $1 \leq Q^2 \leq 10\ \mathrm{GeV}^2$) of this experiment, below the range of x and Q^2 accesible at SLAC energies, were:

(a) the ability to measure incident beam flux at various beam intensities,

(b) the control over pion and non-scattering backgrounds at all kinematic settings,

(c) the use of single spectrometer to avoid normalization errors between cross sections at different ϵ-points (scattered energy and angle were limited to $1 \leq E' \leq 8$ GeV and $11 \leq \theta \leq 46°$), and

(d) the ability to calculate radiative corrections accurately.

Various improvements were made to the existing equipment in the End Station A at SLAC to enable accurate cross section measurements as discussed in this chapter. The computer controlled pusle-by-pulse beam steering system [II.1] installed in a previous experiment, and detailed studies of the calibration of toroidal beam charge monitors [II.2] in this experiment, were crucial. A floating wire study [II.3] of the 8 GeV spectrometer optics provided an accurate measurement of the momentum dependence of the acceptance. The improved components of the detector included a refurbished Hydrogen Cherenkov counter, and a new lead glass shower counter. These detectors enabled an electron detection efficiency of 99.5% while maintaining pion misidentification level below 10^{-5}.

B. Experimental setup

The electron pulses from the Nuclear Physics Injector, for beam energies upto 5 GeV, and, from the Main Injector, for higher beam energies, were accelerated through the Stanford Linear Accelerator. These beams were directed into the End Station A by a series of bending magnets (see Fig. II.1) located after the beam switchyard. After entering the experimental hall, the electrons passed through the toroidal charge monitors and impinged on a target placed on the pivot (see Fig. II.1). The scattered electrons of selected momentum between 1 and 8 GeV were detected using the 8 GeV/c spectrometer (Fig. II.2), which was positioned at angles which ranged between 11 and 46° during the experiment. The detector package in the spectrometer "hut" consisted of a threshold H_2-gas Cherenkov counter, three planes of plastic scintillator detectors, a ten-plane multi-wire proportional chamber and a total absorption lead-glass shower counter. When triggered, the electronics modules located in the counting house above the End Station A read the data from the detectors, and logged them on a computer. These data enabled measurement of cross section at various kinematic settings.

The data taking strategy was such that minimum time was wasted in setting up the experiment to measure cross sections at various kinematics. The setting up of spectrometer angle θ and energy E' typically took five minutes, compared to about few hours for changing the energy E. Therefore, different θ and E' settings were spanned at a fixed E. To minimize any time dependent systematic errors, data were taken rotating between various targets (Fe, D_2, ...), in runs which typically lasted two hours.

The following sections describe the detectors, the data taking procedure and, the measures taken to ensure a good measurement of cross section.

C. Beam steering and charge monitors

The transport of the electron beams from the accelerator to the experimental hall via the A-bend (see Fig. II.1) was controlled by the Main Control Center. Beams of energies between 3.75 and 19.5 GeV were supplied during this experiment, at required currents. The ability to adjust the beam current between 0.1 and 30 mA, in short period of

time, was especially important in the control of the dead time and background contamination. The incident beam energy was measured using a flip-coil in a bending magnet, and by a shunt. The incident beam energy spread was controlled by varying the width of lead collimator slits, located between the two 12° bends after the beam switch yard. These slits were placed during the data taking such that the energy spread was less than ±0.1%. When the beams of required energy were made available by the accelerator operators, they were first observed, at low intensity, on two ZnS screens, on which they formed elliptical spots. The ZnS screens were located in the beam pipe in the End Station A, and were aligned with the center of the target and the beam position monitors. The strengths of the bending magnets along the beam pipe in the End Station were adjusted manually so that the beam passed through the center of the target. The computer controlled beam steering system was then calibrated. This procedure was repeated at every energy change of the incident beam, and when the beams were turned on after accelerator shutdown.

The position and angle of the electron beams transported to the End Station A were continuously monitored and controlled using a beam steering system consisting of a microwave-cavity, and two wire array secondary emission monitors (SEM's). The LSI computer which read the pulse-by-pulse beam position information from microwave cavity and SEM's, corrected any missteering of the beam by adjusting the field of the bending magnets. The incident electrons were normal to the target within ±0.003°. The LSI also accumulated histograms of instantaneous beam positions and angles to enable offline calculation of the incident beam angles.

The electron beam charge was measured using two independent but identical toroidal charge monitors. Electron beam pulse passing through the beam pipe in End Station A induced current, proportional to the charge carried by the pulse, into the toroidal coils surrounding the pipe. This signal was amplified and fed into two sets of electronics which analysed the signal to find charge in each pulse. Both these toroidal charge monitors were equipped with a calibration systems consisting of a precise capacitor which was charged to a known voltage, and then discharged through an additional winding around the toroid. The calibration and zero drift of these systems were checked often (typically every two hours, i.e. between two data taking runs). The detailed analysis of calibration runs will be reported in the thesis of R. C. Walker [II.2]. Fig. II.3a shows the calibration corrections to the raw charge measurement for each data run. The jumps in these numbers correspond to the times when a burnt capacitor was replaced. Fig. II.3b shows the difference between the charge as measured by the two independent monitors. From these data it is inferred that the run-to-run error on the charge measurement was $\pm 0.2\%$, whereas over longer periods (i.e. after few runs) the uncertainty was $\pm 0.3\%$. The absolute calibration of the toroids was known to about $\pm 1\%$.

C. Targets and density monitors

Three liquid targets, two empty target replicas and three solid

targets were used in this experiment. The liquid deuterium at 21°K flowed through two targets, each of length 20cm and 10cm at a pressure of 20psi, while the third long target, also of 20cm length, had liquid hydrogen. Two empty target replicas of length 20cm and 10cm were used to measure background counts from the liquid target endcaps. The solid targets were made of iron (2.6% and 6% radiation lengths) and gold (6% r.l.).

Most inelastic data for liquid targets were obtained off the 20cm-D_2 target. The inelastic data obtained using the 20cm-H_2 target were rendered useless because of the collapse of an aluminum tube located inside the target. In the rest of this thesis the 20cm-D_2 and 20cm-empty replica are called as deuterium and empty targets respectively. The deuterium target, shown in Fig. II.4, consisted of a cylindrical aluminum tube, with axis along the direction of beam. The distance between the two endcaps soldered to the ends of the target tube, defined the deuterium target region. Liquid deuterium flowed in the direction of the beam through a thin aluminum tube placed insided the target (For the hydrogen target the flow was reversed and causing the tube to collapse). Two vapor pressure bulbs and platinum resistance probes were located at the inner ends of the target to measure the target temperature, and were read every 10s by the computer. The empty target was identical to the deuterium target in construction but for two extra radiators place at the two endcaps to account for the radiation lengths of deuterium.

The solid targets were located on a movable frame (see Fig II.4). Thermocouples were connected to the targets to measure the temperature. The target thickness was measured using precision gauges before and after the experiment. The error on these measurements is ±0.0005 cm. The relative error on the 2.6% rl iron and 6% rl gold targets are larger than the 6% rl iron. Most of the solid target data were obtained using the 6% rl iron target. The 2.6% rl Fe target was used to check the accuracy of the external radiative corrections. For the results on the ratio σ^{Fe}/σ^{D} and the difference $R^{Fe}-R^{D}$, the difference in radiation lengths of the deuterium target (2.6%rl) and the iron target (6%), had to be taken in to account. Beam currents were adjusted such that the data taking conditions for these two targets were similar at each kinematic setting. Table II.I shows the details of the target lengths and radiators in the beam line.

E. Spectrometer

The 8 GeV/c spectrometer at End Station A has been used in many wide angle scattering experiments at SLAC [II.4]. Its rigidity and ability to swing to wide range of angles (11° to 46° in this experiment) were important to attain the required ϵ-separation in this experiment. This focussing spectrometer (see Fig. II.5) has 2 bending and 3 focussing magnetic elements and a sheilded enclosure-"hut" to house the detectors mounted on a carriage that swings to various angles around the pivot. The motion along the railing was activated easily, from the counting house, by a microprocessor controlled motor. Optical properties of these magnets were studied extensively in 1969 using electron beams. It has been used to focus 1 to 8 (GeV/c)

electrons in previous experiments successfully. It was designed to measure the scattered energy E' and angle θ with good acceptance for particles which scatter from extended targets placed at its pivot. The charged particles entering the spectrometer are bent by 30° in vertical direction to suppress the background in the "hut". Additional background suppression is achieved by placing concrete shielding over the bending magnets. The focussing is line-to-point in the horizontal plane and point-to-point in the vertical. Fig. II.6 shows the optical properties of the spectrometer.

A detailed study of the optics of the spectrometer using floating-wire method were performed recently [II.3]. This experiment involved precision study of the behaviour of a wire carrying current (which simulates a charged particle traversing the spectrometer) floating in the magnetic field of the spectrometer. From this study the coefficients of the transfer matrix, which maps the measured coordinates of the particle at the focussing plane in the spectrometer to the particle coordinates at the target, were determined. Also, the momentum dependence (in the range 1 - 8 GeV/c) was studied. For the results reported in this thesis, the 1967 optics measurements were used with a correction factor to account for a change of acceptance with momentum measured in the floating-wire study (see Appendix A for details).

F. Particle detectors

1. Introduction

The purpose of particle detectors housed in the spectrometer "hut" was to identify the electrons, discriminate against pions and other particles, and determine the energy and angle of the electrons. The following detectors, were placed along the particle path (see Fig II.7): a threshold Hydrogen gas Cherenkov counter, ten-plane multiwire proportional chamber with a layer of plastic scintillator detectors after the sixth chamber, five-layer segmented lead glass shower counter with two sets of plastic scintillator detectors after the first and last layers. The Cherenkov counter, and the shower counter were rebuilt for this experiment.

2. The threshold hydrogen gas Cherenkov counter

The two meter long Cherenkov counter chamber was filled with high purity hydrogen gas (less than 1 ppm O_2) at 1 atm pressure. At this pressure threshold for Cherenkov light from pions is above 8 GeV/c. Hydrogen gas was chosen because the knock-on electron rate in it is very small. Oxygen contamination in hydrogen causes absorption of the ultra-violet light and therefore, precautions were taken to avoid air leaks into the chamber. For instance the "hood" which houses the photo-multiplier tube was filled with N_2. The chamber was also purged once a week with N_2 and H_2 to avoid any degradation in the quality of H_2. Cherenkov light produced when a charged particle traverses the counter, is focussed on to the face of the photo-multiplier tube by spherical mirror located at the end of the chamber. The mirror was rebuilt and coated with MgF_2 to reflect ultra-violet light in addition to the visible light. The mirrors were aligned accurately using laser

beams before the counter was installed in the "hut". A quantacon (RCA 8854) photo-tube, which has a high gain and good efficiency was installed in the hood. The surface of this tube was coated with a wave length shifter to convert the ultra-violet photons to visible light for which the photo-cathode is more sensitive. With these improvements, an electron efficiency of 99.7% was achieved while maintaining the pion misidentifcation level below 1 in 10^4. An average of 7 photo-electrons were detected per electron passing the chamber.

3. The Multiwire Proportional Wire Chambers

Ten planes of proportional wire chambers were located just after the Cherenkov counter. Each chamber had an active 35 cm high and 93 cm wide area. The anode wires were oriented either horizontally or at ±30 degrees to the vertical. Angular orientation "vertical" chambers enabled additional information on the angle of the particle track in addition to the vertical coordinate measurement. The detailed description of the wire chambers is available in references [II.1] and [II.5]. The wire chambers were operated in a proportional mode using a gas mixture, "magic gas", of 65.75% argon, 30% isobutane, 4% dimethyl acetal formaldehyde, and 0.25% bromotriflouromethane.

The chambers were numbered sequentially in the direction of the particle path. The even numbered chambers had 176 horizontally oriented anode wires. The odd numbered chambers 1, 5 and 9 had 480 wires each oriented at +30° to the vertical, when viewed in the direction of particle path. The other two chambers 3 and 7 had wires at -30° with respect to the vertical. The anode wires in the odd numbered chambers were instrumented in pairs. At the typical operating voltage of about 3.6 kV, each chamber had an average efficieny for electrons of about 98%. Ten chambers of such high efficiency were more than required for accurate particle tracking. The combinatorial problem of track finding, usually yielded multiple tracks due to the signals from the low energy particles. The algorithm used the information from the shower counter segments and scintillation counters to purge pion and non-physical tracks. The overall tracking efficiency but was better than 99%. A correction factor for the efficiency was calculated for each run and applied to the data.

4. Scintillation counters

Three planes of plastic scintillation counters were used to help in triggering, and in aiding particle identification in ambiguous cases. The first layer of counters (SF) was vertical segmented in to five 6 inch wide strips, and was located between the 5th and 6th wire chambers. The middle (SM) and rear (SR) counters were segmented horizontally and were viewed by photo-tubes on either side. SM was located between the 1st and 2nd layer of lead glass shower counter, and SR was located at the rear end of the lead glass. SF and SM were part of the electron trigger. SR was used only in special studies, and in efficiency calculations to veto on pions.

5. Shower Counter

The lead glass shower counter was segmented both horizontally (X) and in the beam (Z) direction. Care was taken to fill in the gaps by staggering the blocks of lead glass. Fig. II.8 shows a schematic diagram of the shower counter. The first row of six lead glass blocks (PR) each of thickness 3.2 rl. It was instrumented with photo-multiplier tubes (PMT; Amperex type XP2041) on the top. A row of seven 6.8 rl thickness blocks were placed after the SM counters, and were monitored by PMT's on the top (TAU) and the bottom (TAD). The next three rows (TB, TC and TD) each of 6.8 rl thickness, were viewed by PMT's located on the top. The PR, TA and TB rows together had enough radiation lengths to absorb most of the shower from electrons upto 4 GeV but the TC row was also necessary for electrons of higher energy. TD counters were not used in the electron energy determination but were of use in discriminating against pions which started shower in the PR.

Details of shower energy calculation procedure are described in the Appendix B. The resolution achieved with this counter was $18\%/\sqrt{E'}$(GeV) FWHM. The advantage of additional e/π discrimination allowed by the segmentation of the lead glass more than compensated for the slight loss in the resolution due to the calibration difficulties. Fig. II.9 shows the shower spectrum with a cut on the Cherenkov counter pulse height, for the worst case of pion background (e/π=120) showing a clear separation of pions and electrons. The background of pions (which was 0.2% for the worst case) under the electron peaks was estimated and subtracted for each run.

G. Electronics and Data Logging

The electronics data aquisition system was designed using commercially available NIM and CAMAC modules. The electronics system was divided into three separate groups viz. 1) fast electronics for event reading, 2) detector monitor electronics, and 3) beam steering and toroid charge monitor electronics.

The purpose of the fast electronics was to form a high efficiency trigger for electrons and to discriminate against pions (which would otherwise have swamped the data aquisition system at most kinematic settings) and to read the event information from all the detectors. The raw detector signals from the spectrometer were carried to the counting house ~100m away by either fast heliax cables (for trigger components) or by regular coaxial cables. The raw signals were then divided using linear fan outs (see Fig. II.10). One channel was fed through discriminators and continued to trigger logic, TDCs and scalers, and the other was fed to the Analog-to-Digital converters for spectrum analysis. As shown in Fig. II.10 SF, PR....SR were made of linear sums of the individual counters SF1...SF6, PR1....PR6, respectively. The Cherenkov and TA signals were shortened to about 20 ns in width, using clip lines with resistive termination. The discriminator pulse hight threshold was set as following: PR=30mV, TAD=100mV, Cherenkov=50mV, SF=50mV and SM=50mV. These sum pulses were used in trigger building. The schematic diagram in Fig. II.10 also shows the trigger logic. There were two kinds of triggers for electrons in addition to triggers for pions etc. which were used in

test runs. One trigger, called Electron-Lo, was composed of Cherenkov signal in coincidence with at least two out of the following three signals: SF, PR or SM. The other, named Electron-Hi, demanded coincidence of at least three signals among Cherenkov, PR, SM and TAD. Electron-Hi was an efficient trigger at high electron energies as it demanded either a high signal from the shower counter, or both Cherenkov and the shower counter signals. However, at low energies there was possibility of inefficiency of the shower component of this trigger due to stringent requirement of shower counter signal, and was compensated by the Electron-Lo. The final "ELECTRON" trigger required at least one of the triggers Electron-Lo or Electron-Hi has fired. The trigger efficiency achieved during the experiment was better than 99.9999%. The "PION" trigger demanded a coincidence between SF and SM, and was pre-scaled by a factor of 2^8 to reduce the number of pure pion events logged on the tape. A pulse generator was used to generate infrequent "RANDOM" triggers which were useful in monitoring zero drifts of ADC's. PRETRIGGER was generated whenever an ELECTRON, PION or RANDOM trigger fired within the beam gate. Due to limitations in the speed with which the computer could read the event information from the CAMAC electronics, the PRETRIGGER was combined with a veto to form TRIGGER which limited the actual event logging rate to a maximum of one per 1.6 μs beam pulse. Provisions were made to measure the computer dead time are described below. The TRIGGER generated an ADC gate of 100 ns wide, a TDC common start signal, a gate for MWPC data reading, and a TTL signal for computer inturrupt. A dedicated PDP-11 micro-computer read the data from various CAMAC crates which housed

ADCs, latches and TDCs, and wrote to rotating buffers of memory which was shared with main End Station A VAX-11/780 computer. The VAX computer wrote the information from this memory bank to a magnetic tape, and also analysed a sample of the data online.

The scalers were read directly by VAX through a separate CAMAC link every 10 s. The 120 channels of scalers counted not only the triggers and individual pulses from every detector channel, but also coincidences between various signals, for instance the PTC signal which is a coincidence of PR, TAD and Cherenkov. Additional ELECTRON and PTC discriminator signals of 40, 60, and 80 ns in width were counted to determine the electronics dead time correction. The detector high voltages, magnets, target temperatures etc. were monitored directly by VAX. There was a computer link to Accelerator Main Control Center to get information about A-bend magnets, and incident electron energy.

The toroidal charge monitors and beam steering system described earlier were connected to a dedicated LSI-11 micro-computer. The LSI-11 was in turn interfaced to the online VAX computer. The toroid information and condensed beam steering information was read by VAX at a slow rate on this link. The experimental control was through a SLAC designed "switch system" which allowed setting up the spectrometer, detector and the target by computer control and executing experimental runs. A dedicated console was used for warning the shift operators about any malfunction of any component be it detector, electronics or spectrometer magnets. This system also allowed displaying various histograms of interest on a video screen. A sample of the data was

analysed online to verify that the experiment was proceeding properly, and to provide estimates of the cross section. Also a brief summary of the analysed data was written on the disk so that detailed online analysis to obtain cross sections and R was done during the data taking. These on-line results allowed decisions to be made regarding the relative allocation of running time at the various kinematic points.

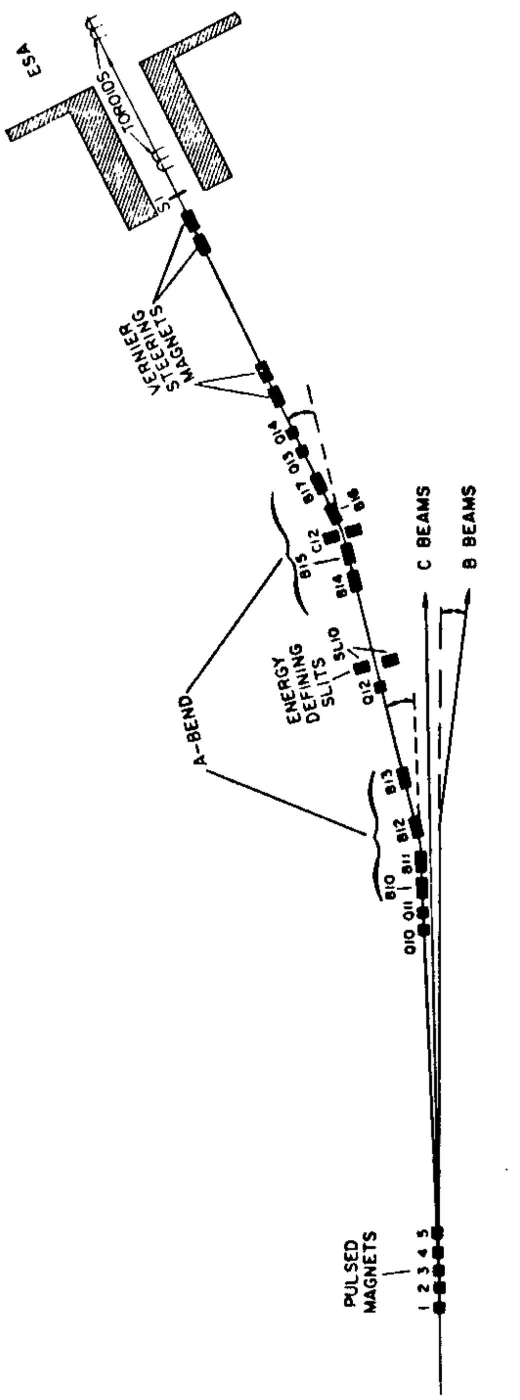

Fig. II.1 The beam transport system from Stanford Linear Accelerator to the End Station A.

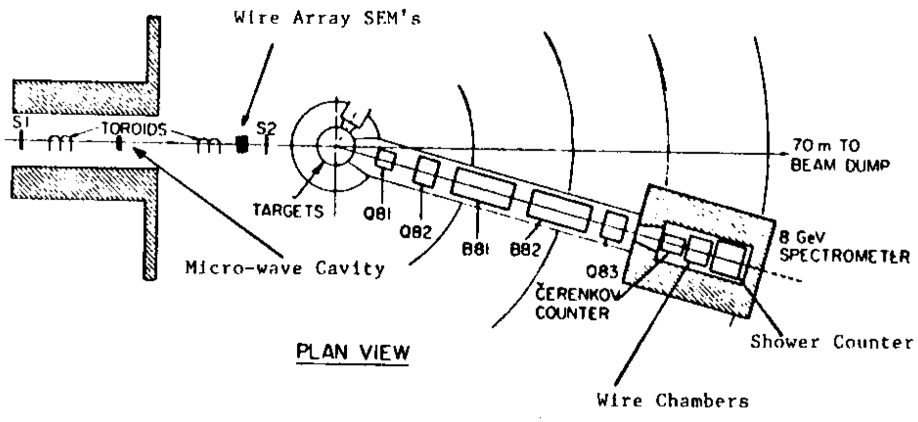

Fig. II.2 The experimental setup in the End Station A.

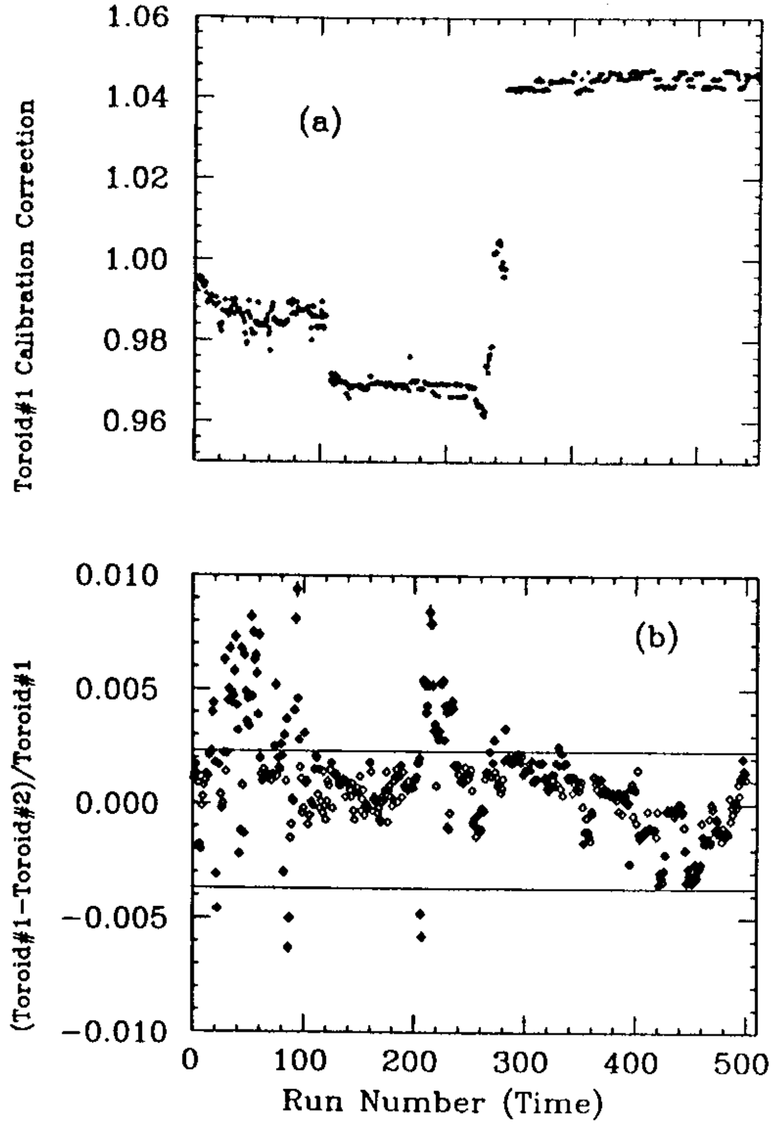

Fig. II.3 (a) Toroid calibration corrections for system 1 are plotted versus time (arbitrary units) . (b) The difference in beam charge as measured by toroid system 1 and 2 (normalized to system 1) is plotted versus run number (time). The band shown corresponds to ±0.3% difference.

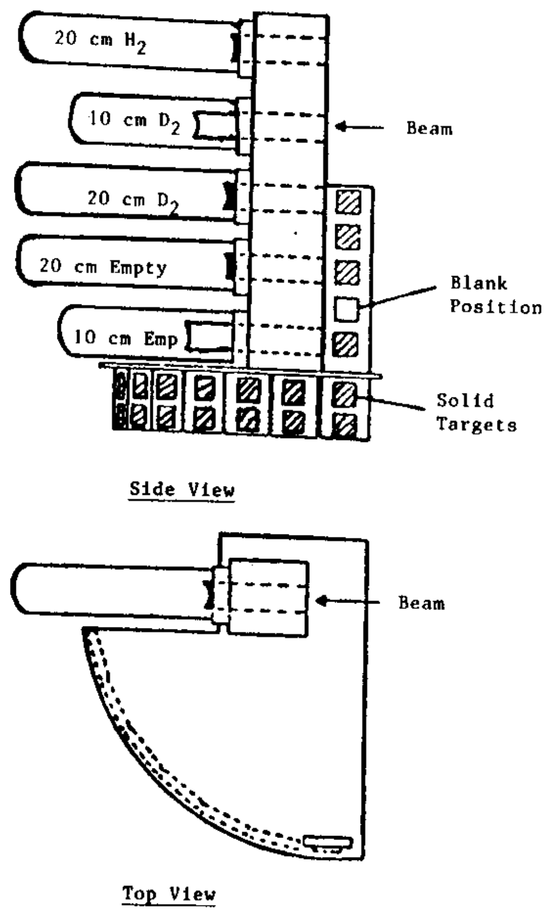

Fig. II.4 Schematic view of target assembly.

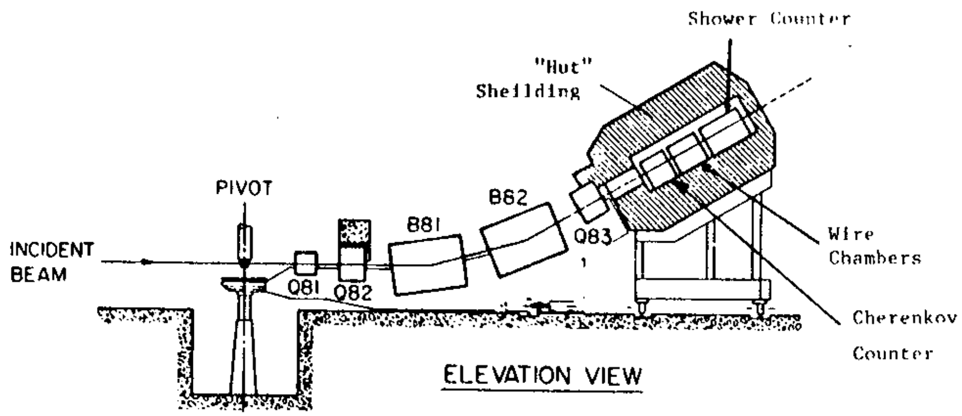

Fig. II.5 An elevation view of 8 GeV spectrometer showing the magnet and detector systems.

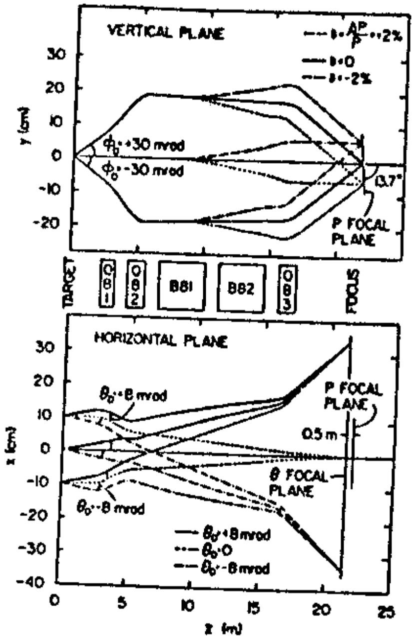

Fig. II.6 First order optical properties of the 8 GeV spectrometer. The spectrometer focuses point-to-point from target to focal plane in the vertical plane. Particles with the same fractional momentum deviation $\delta=\Delta p/p$ from the central momentum are brought to a focus in a tilted focal plane as shown above. In the horizontal plane the spectrometer focuses line-to-point, and so particles with the same horizontal angle θ_0 at the target are imaged onto the same horizontal position on the focal plane.

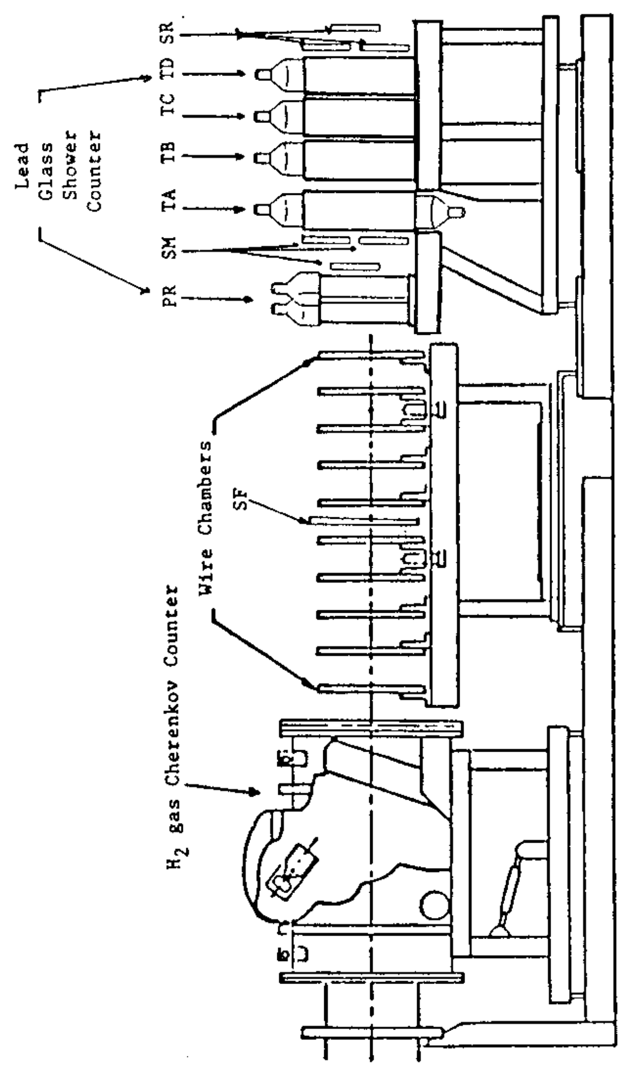

Fig. II.7 The 8 GeV spectrometer particle detectors. The threshold H_2 gas Cherenkov counter and the lead glass shower counter provided particle identification and triggering (with the scintillation counters). Ten planes of multi-wire proportional chambers allowed charged particle tracking.

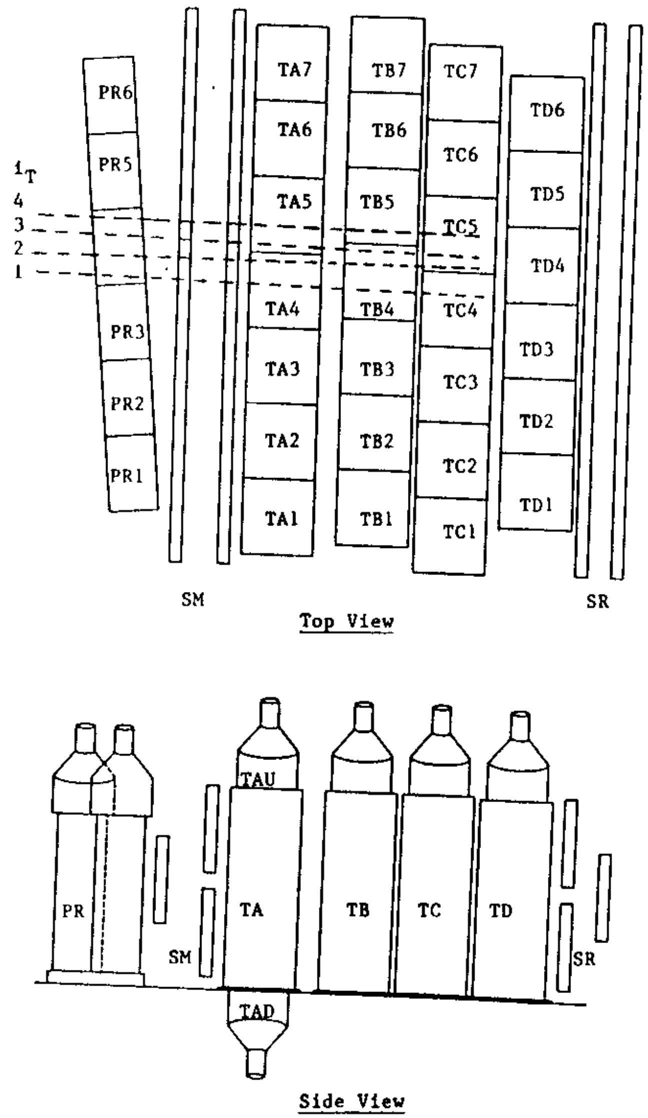

Fig. II.8 A shematic diagram of the lead glass shower counter shows the segmentation and staggering of the lead glass blocks. The track types defined in the Appendix B are also indicated.

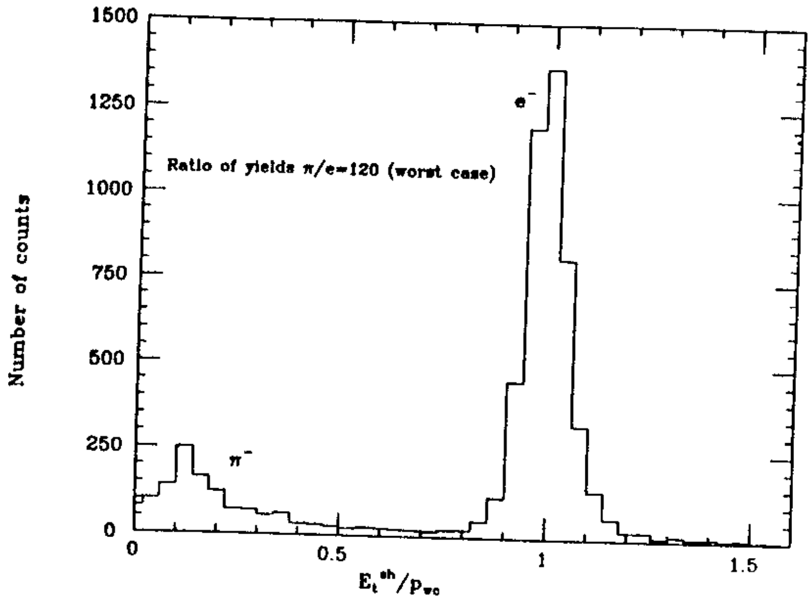

Fig. II.9 Shower counter spectrum with a requirement of high signal in Cherenkov counter (50 ADC channels), and a single track in the wire chambers, is shown for the worst case of pion background, $\pi/e = 120$. A clear separation of electron and pion peaks is seen. Horizontal axis is shower energy E_t^{sh} normalized to the momentum of the track as determined by the wire chambers, p_{wc}.

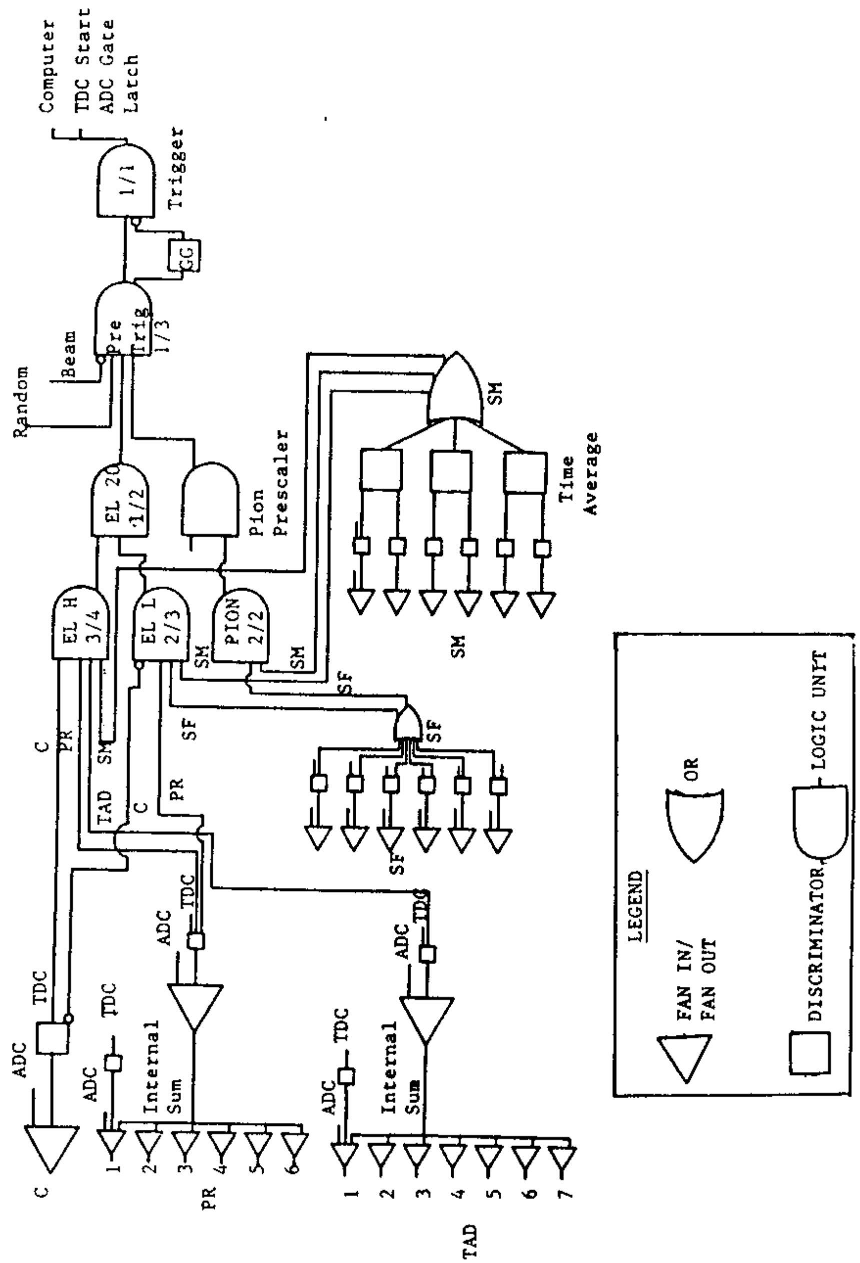

Fig. II.10 A schematic diagram of the Electronics data aquisition system.

TABLE II.Ia

Deuterium and Empty target dimensions†

Component	Deuterium	Empty replica
Target length (cm)	20.086	20.045
Flow separator (Al)	0.000288	0.000288
Cell Wall (Al)	0.000864	0.000864
Insulation (mylar)	0.000221	0.000221
Front endcap (Al)	0.000864	0.014001
Back endcap	0.000864	0.014001

† Except for target length, which is in cms, all other dimensions are in radiation lengths.

TABLE II.Ib

Solid target dimensions

Target	Thickness (cm)	(%)
Fe (6%)	0.1067 ±	0.5
Fe (2.6%)	0.0470 ±	1.1
Au (6%)	0.0198 ±	2.6

TABLE II.Ic

Material before/after target

Component	Thickness (rl)
Material before	0.00103
Material after	0.00940

REFERENCES

[II.1] A. F. Sill, Ph. D. thesis (1987), The American University; J. G. Gomez, Ph. D. thesis (1987), The American University.

[II.2] R. C. Walker, Ph. D. thesis (in preparation), Cal Tech.

[II.3] L. Clogher et al., SLAC-PUB (in preparation for submission to Nucl. Ins. Meth.); and L. W. Whitlow, Ph. D. thesis (in preparation), Stanford University.

[II.4] E. D. Bloom et al., Phys. Rev. Lett. 23, 930 (1969); M. Breidenbach et al., Phys. Rev. Lett. 23, 935 (1969). A. Bodek et al., Phys. Rev. D 20, 1471 (1979).

[II.5] P. Bosted and A. Rahbar, SLAC preprint NPAS-TN-85-1, (Feb 1985).

III DATA ANALYSIS

A. Introduction

Data analysis was carried out off-line in two separate cycles. The first cycle of analysis, using software adopted with minor modifications from earlier SLAC experiments [III.1], yielded preliminary results which were presented at conferences [III.2]. With the experience gained in the first pass analysis, the software was modified significantly to yield precision results described in this thesis. The schematic description of the analysis structure is given in Fig. III.1. The high density tapes written during the data taking were rewritten after sorting out the toroid calibration runs and bad runs from the regular data runs. The analysis of toroid calibration runs will be described in detail in the thesis of R. C. Walker [III.3]. The data runs were first processed to reconstruct the electron events. This process was CPU-intensive, and was therefore done once and the results were written to a giant RUNSUMMARY table. This organized data base was then used to calculate acceptance of the spectrometer (described in Appendix A), and to calculate cross sections and final results. All of this analysis was performed on Digital Equipment Corporation VAX 11/780 computers at Rochester and SLAC. Radiative corrections were calculated in separate programs on IBM mainframe system at SLAC, and on Rochester's new VAX 11/8800.

B. Event Analysis

The edited tapes typically consisted of several data runs. Within each run two types of data were logged, event-type and non-event-type. Event type data were written to tape for every trigger, whereas non-event-type data were written at regular intervals to include scalar readings, toroid current readings etc.

The steps involved in event-type data analysis were:

1) The information from latches was used to classify the event into electron, pion or random-type. The full analysis was done only for the electron-type events, although pion-type events were used in test runs. Random-type events were analysed to obtain ADC pedestals. ADC pedestals did not fluctuate by more than one channel (~10MeV) during the entire period of data taking. These fluctuations were of no consequence for the shower energy calculation.

2) The shower counter ADC information was used, after subtracting the pedestals, along with the block shower calibration coefficients (see Appendix B) to obtain the energy deposited in each block of the shower counter E_b^{sh} (shower-sum energy).

3) Reconstruction of tracks seen by the wire chambers was next step. Tracks were constructed demanding hits in at least 7 out of the 10 chambers with at least 3 hits in either horizontally wired or vertically wired chambers. If tracks were found with this configuration, it was checked if at least one of them pointed to a shower counter block which had energy deposition,

otherwise tracks were constructed demanding hits in at least 6 chambers with alteast 2 of each kind.

4) Corresponding to each track the shower energy E_t^{sh} (shower-track energy) was calculated using the shower-track calibration coefficients (see Appendix B).

5) Kinematic quantities ($\Delta p/p$, $\Delta\theta$, ϕ etc) were calculated for each track, using spectrometer transfer matrix coefficients listed in Table A.I. The momentum of the detected particle calculated from the track coordinates is given by $p_{wc}=p+\Delta p$.

6) Often events had multiple tracks at this stage, either due to combinatorics of track finding algorithm or due to pions and other charged particles entering the spectrometer. To purge the tracks to yield a single good track (corresponding to an electron), shower energy, the time of flight between the Cherenkov and middle scintillator, reconstructed interaction point, and goodness of fit criteria were used. Ambiguous events with one electron and a pion or with two electrons were a small percentage (<<1%), and in those cases electron was associated randomly with one of the tracks.

7) Flags were then defined to identify electron events, and to enable calculation of efficiencies. Some of these criteria are listed below:

a) Single good track was found in the wire chambers,

b) Track was within the good fiducial region,

c) Cerenkov signal was greater than 50 ADC channels,

d) Shower-track energy $E_t^{sh} > 0.7\ p_{wc}$,

e) Reconstructed kinematic quantities were within acceptance of the spectrometer i.e. $|\Delta p/p| < 3.5\%$, $|\Delta\theta| < 6$ mr and $|\phi| < 28$ mr,

f) Particle originated from the target i.e. The reconstructed x-position at the pivot corresponded to the target coordinates,

g) PR signal was large,

h) PR and Cerenkov signal combination was large,

i) TA signal was large,

j) Time of flight between Cerenkov and middle scintillator SM (TOF) corresponded to an electron flight time,

k) Shower-sum energy $E_b^{sh} > 0.7\ p$,

l) Event was within good fiducial region defined by SM/SF grid and TAU/TAD time of flight difference; Cuts k and l were important for wirechamber inefficiency study, and

m) The event was CLEAN, i.e. it had less than 3 tracks before purging.

8) Various combinations of the cuts defined above were demanded, and the events passing those cuts were accumulated in an array. These numbers enabled calculation of efficiencies as described below.

9) Finally, an electron event was deemed to have been found if the cuts a-f (above) have passed. The event was then histogrammed vs $\Delta p/p$, $\Delta\theta$ and ϕ. In addition, histograms and plots of selected quantitities, e.g. shower energy, Cerenkov ADC, reconstructed $\Delta p/p$ etc, were accumulated.

Non-event data consisted of information about beam pulse repitition rate and energy, or toroid current readings, or LSI beam steering information, or high voltage levels on the detectors, or scalar readings, or target temperature readings. Consistency checks were done and then the data was accumulated for the entire run. At the end of this analysis for a run, all the accumulated information was written into the direct access RUNSUMMARY file. Also the histograms and plots made for diagnosis were written to disk.

C. Cross section calculation

Cross sections for each run were calculated using the information from the run summaries on the direct access file. This process involved calculating the number of misidentified pions, salvaging good electrons from ambiguous events, estimating efficiencies of detectors, calculating corrections to the cross section due to dead time etc. and organizing the runs into (x,Q^2,ϵ) sets. Measured backgrounds (electrons from processes other than deep inelastic scattering, and due to scattering off endcaps of liquid D_2 target) were subtracted, and electron cross sections obtained at similar kinematics were averaged. Radiative corrections (described in detail in Appendix C) were applied to these experimental cross sections to obtain final Born cross sections at various x, Q^2 and ϵ.

The measured cross section formula was given by

$$\sigma_{meas} = \frac{d^2\sigma}{d\Omega dE'} = \frac{N_e - N_\pi + N_a}{\Delta\Omega\Delta E' Q n_t} \frac{C_c C_e C_k C_n C_a}{A E_c E_w E_s},$$

where $(N_e - N_\pi + N_a)$ was the total number of electrons detected in solid angle $\Delta\Omega$ with energy between $E'-\Delta E'$ and $E'+\Delta E'$, Q was number of incident electrons, n_t was number of target nucleons per unit area, A was the acceptance factor, and C's and E's were correction factors and efficiencies respectively. Correction factors were applied for all known effects which were larger than 0.1%, and were namely: computer dead time (C_c), electronics dead time (C_e), kinematic correction (C_k) to adjust cross section to nominal (x,Q^2) setting, neutron excess correction (C_n) for iron and gold targets, and correction to account for variation of cross section within the spectrometer acceptance (C_a),i.e. the bin centering correction. The quantities E_c, E_w and E_s were efficiencies of Cerenkov counter, wire chambers and shower counter respectively. These, and corrections to target density, spectrometer momentum and angle setting are discussed below. The corrections to the acceptance factor A are described in Appendix A.

The raw number of electrons N_e detected in the good acceptance region defined by $|\Delta p/p|<3.5\%$, $|\Delta\theta|<6$mr and $|\phi|<28$mr, was obtained by summing the counts in the histogram written to the disk. The pion contamination N_π was then subtracted. This subtraction was less than 0.2%, even for the worst run with π/e yield of 120. Pion contamination was obtained by extrapolating the low shower energy tail to the region of $E_t^{sh}/p_{wc} > 0.7$ [III.4]. A small fraction of events (less than 0.1%) failed the cut f (i.e their reconstructed particle position at the target did not correspond to the target coordinates), although they were unambiguosly identified as electrons which passed through the central portion of the detector(cut 1 was true). These events signalled a failure in the tracking program which retained a random track, and purged the good electron track, and therefore the reconstructed quantities were wrong. These events N_a were added to the electron counts.

The average of the two toroid readings, after corrections for any calibration changes, was used for determining the number of incident electrons (Q).

The total acceptance $A_{tot}=\Delta\Omega.(\Delta E'/E')$ within the good acceptance region defined above was 0.0366 mr^2. The liquid target was 20cm long, and therefore the acceptance A_{tot} was smaller at large angles. The correction to take this effect in to account (< 0.4% at the largest angle of 46°) was determined using Monte Carlo simulation of the spectrometer, as described in Appendix A. The spectrometer momentum was monitored at every setting using an NMR probe which measured the magnetic field. There was a systematic effect due to a polynomial fit used to set the current in the magnet coils. This effect was measured with the NMR probe. In addition the spectrometer momentum setting was studied in the floating wire experiment (see Appendix A), and a correction factor was applied.

The values for number of nucleons per unit area n_t were obtained from target thicknesses listed in Table II.I. The liquid D_2 density measurements discussed in the thesis of A. Bodek [III.5], were used in these calculations. Corrections to D_2 target density due to fluctuations, as measured by the vapor pressure bulbs, from nominal

values at 21°K were applied. The fluctuations due to beam heating during the data taking were studied in separate data runs, and are described later.

Computer dead time (C_c) was determined in three different ways, which agreed very well. The first method was to use scalars to determine th fractional number of PR, TAD and C coincidences (PTC) missed by the computer. The second method consisted of using the long gate (1.6μs) ADC histogram for the PTC discriminator pulse. The fraction of times the ADC pulse was higher than single event pulse gave the correction to account for the events missed by the computer. The third method was to assume Poisson statistics for events to occur within a beam spill and to estimate probability for multiple events knowing the probability for single event occurance. Corrections from the first method were applied to obtain final results. These corrections were a maximum of 18%, and were the biggest correction to the measured cross section. However, the error on the cross section due to these corrections was only at the level of 0.2%, due to high statistics on our data. The fraction of multiple electron events provided an additional check over the computer dead time correction.

Electronics dead time (C_e) was also determined using the PTC scalars. The PTC pulses of different gate widths (20ns, 40ns, 60ns and 80ns) were counted separately, and these were extrapolated to 0ns to estimate the corrections for the finite width. These corrections C_e were small, at a maximum of 0.5%.

Kinematic correction (C_k) was applied to correct the cross section for slight offsets in the settings of the spectrometer energy and angle compared to the nominal values, so that all ϵ points had the same (x,Q^2). This correction, obtained using the fit to old SLAC inelastic data [III.6], was typically 0.5%, and was 2% for the worst case. The error on cross section due to this correction is estimated to be negligible.

Iron and gold cross sections were converted to cross section per nucleon by applying a neutron excess correction C_n. Final cross section σ_{meas} for Fe and Au targets represents the cross section per nucleon, of a hypothetical nucleus (atomic mass A) with an equal number of (A/2) protons and neutrons. The cross section ratio $\sigma_n/\sigma_p(x)=1+0.875x$ was obtained from a fit to previous SLAC data [III.6]. There was a 2% Hydrogen contamination in the liquid Deuterium target. A correction factor using σ_n/σ_p fit was applied to correct for this proton excess.

Cross section varied by upto 5%, often non-linearly, within the spectrometer acceptance. A center-of-bin correction factor C_a was used to obtain the cross section at the central setting of the spectrometer. C_a was calculated using the fit to old SLAC data, and our data binned in $\Delta p/p$, $\Delta\theta$ and ϕ. If the acceptance function (see Appendix A) is given by $A(\Delta p/p,\Delta\theta,\phi)$, and the fit cross section (The original fits for Born cross section were modified by a parameterization of variation of radiative corrections within the spectrometer to obtain the fit to "measured" cross section) is $\sigma_F(\Delta p/p,\Delta\theta,\phi)$ and σ_F^c in the bins and at the central setting respectively, the correction factor C_a is given by:

$$C_a = \frac{\sum_i \sigma_F(i)\ a(i)}{\sigma_F^c}. \qquad \text{Index 'i' runs over } \Delta p/p, \Delta\theta \text{ and } \phi.$$

Efficiency of wire chambers for track reconstruction was determined by counting number of good electron tracks reconstructed for potentially good electrons defined by the Cerenkov, shower and scintillators alone (i.e with flags SHSUM, SGOODFID, PR, TA, C). This efficiency E_w varied between 99.6% and 100%, and was computed run-by-run and applied to the cross section. The fraction of zero track events in the data provided an additional check on the accuracy of the wire chamber efficiency calculation. The efficienceis of Cerenkov and shower counters were calculated using the data from runs where the pion background was small. Run by run calculation of these efficiencies, to the accuracy required, was not possible as it was difficult to identify a clean sample of electrons demanding signals from one of these two counters alone. Efficiency of Cerenkov E_c and shower counter E_s, with the cuts defined earlier were each 99.7%.

The special runs for which data were taken with the spectrometer polarity reversed, and from the empty target replica, and the target boiling test runs were analysed the same way as the regular electron runs.

The data were accumulated in many small runs to reduce systematic effects due to any time dependent fluctuations in incident beam position, angle, energy, charge monitors, detector efficiencies and duty cycle. The cross sections obtained at similar kinematic setup were then averaged (weighted by the statistical error). The background from processes other than deep inelastic scattering, and in case of liquid target the background from scattering off the target end caps, were subtracted.

The flux of electrons from processes other than deep inelastic was measured. This contribution was dominated by the charge-symmetric processes [III.7], e.g. π^0-decay to two γs followed by e^+-e^- pair production, and was determined by reversing spectrometer polarity and measuring positron yeilds, when electrons were incident on the target. Other contributions, in particular non-charge symmetric decay of charged kaons, were estimated to be negligible. If the positrons from the decay of kaons were detected in the detector, they must have done so after the bending magnets in the spectrometer, as there was limited decay volume between the target and the first bending magnet. This implies that the positrons are decay products of K^+s of momentum equal to the spectrometer setting. The positron energy spectrum is then expected to have a falling energy distribution. Fig III.2a,b show the shower spectra for the runs for which e^+/e^- yield was 13% (the highest in our data). These distributions do not substantiate the speculation that positron yield was dominated by K^+ decays. In addition the reconstructed target position for the good positron tracks ($E_t^{sh}/p_{wc} >$ 0.7, $C >$ 50 ADC channels) corresponded to the actual target position, suggesting that these particles have originated from the target, and were not product of decays after the target. In an earlier experiment by L. S. Rochester et al. [III.7] positron yields with incident electrons, and electron yields with incident positrons were measured, and were found to be equal within experimental uncertainty. These assertions imply that the "positron" subtraction accounts for

electrons from processes other than deep inelastic scattering to the level of ±5% accuracy. This subtraction ranged from 13% for 6% rl iron target at some kinematic settings to 0% at others. Positron yields were measured at all kinematic settings were the subtraction was greater than 0.5%. Where the positron yield was not measured a subtraction was made using a fit to such positron yields measured in previous measurements at SLAC. Figs. III.3a-u show the ratio of yields e^+/e^- versus ϵ for all x,Q^2 points along with the fits that were used to subtract when the data from our experiment was not available.

The electron contribution, to the data off liquid D_2 target, from the scattering in the aluminum target endcaps was determined using an empty target replica. To ensure the same rate in data taking, and to account for radiative effects as well as to increase the counting rate, additional aluminum was added at the front and the back of the target end caps, to make the total radiation lengths of the replica identical to the target when D_2 flowed through. This subtraction was 1.2% on average and was determined to 10% accuracy.

The final cross section after these subtractions, includes contributions to the scattering from higher order processes. However, only the Born cross section (see Equation (I.1)) is of interest in determining the structure functions and R. The radiative corrections (described in detail in the Appendix C) were applied to obtain final Born cross sections at each kinematic setting. Table III.I shows final cross sections (before and after radiative corrections were applied) for all the kinematic points. Both the statistical and point-to-point (i.e. ϵ-dependent) systematic errors are shown.

B. Systematic errors

Care was taken in the design, execution and analysis of this experiment to reduce systematic effects. The effects which changed cross section with ϵ were crucial in the determination of R. On the other hand, R^A-R^D results were sensitive to the variation of cross section ratio σ^A/σ^D with ϵ. Large angle and small E'/E regions, which correspond to the low ϵ points are particularly sensitive to the background subtraction, the acceptance correction, and the radiative correction errors. Therefore, the experiment was optimized such that, even in these worst kinematic regions, the errors were acceptable. Table III.II summarizes the systematic errors from various sources for differential cross section (σ), and the ratio σ^A/σ^D. The point-to-point errors were studied in detail, but the absolute errors on σ ($\Delta_{abs}\approx 3.3\%$), in particular those from absolute value of acceptance are still under inveeitigation. The absolute normalization error, Δ=1.1% on the ratio σ^A/σ^D, is dominated by the target length measurement (Table II.I), and "external" radiative corrections (see Appendix C), and is well determined. The effects on R and R^A-R^D are also indicated in Table III.II assuming an average ϵ separation of 0.35. Steps taken to minimize the errors from each of those sources are explained below.

1. Beam steering: The beam position was observed, when freshly tuned beam entered the End Station A, on the ZnS roller screens at two places, and the steering magnets were adjusted such that the beam

hit the center of the target. The microwave cavity and wire array secondary emission monitors (SEM) readouts were calibrated, and the computer (LSI) control was enabled. The beam was monitored by the LSI continuously, and histograms of the position and angle in x and y directions were accumulated on a pulse-by-pulse basis. The average x, y positions, and dx/dz and dy/dz at the two SEM's were recorded on the tape. This information yielded the measure of uncertainty in the incident beam angle to be 0.003°. In addition data was taken, between every few regular data runs, without any target on the pivot (FRAME RUNS) to check if there were any steering problems which caused scattering from the frame on which targets were mounted. These runs were consistent with no gross mis-steering of the beam, which could cause such events.

2. Beam charge: The total incident charge was measured using two precision toroidal charge monitors. These monitors were usually calibrated between every two data runs. In addition long calibration runs which spanned all gain and attenuator settings were taken. This information yielded two independent measurements of charge, although using identical instruments. The difference of the two toroid readings versus run number (time) is plotted in Fig II.3b. The large jumps in the results corresponded to the times when toroid system hardware was changed. The run-to-run fluctuations in the difference were ±0.2%, whereas over a group of runs the differences were ±0.3%.

3. Incident energy: Energy of the incident electron beam was measured using a flip-coil in an A-bend bending magnet. The lead

collimator slits located between the bending magnets were adjusted to allow energy width of $\Delta E \approx \pm 0.5\%$ which defines an upper bound on the error. After all the known corrections to the scattered energy and angle were applied, the elastic peak positions, measured in this experiment [III.8] using H_2 target, were used to determine the uncertainties in E. The error on the incident energy is estimated to be $\pm 0.1\%$.

4. Scattered energy: Spectrometer momentum calibration was studied by NMR studies of the magnetic fields, and by a wire float experiment (see Appendix A). The ability to reset momentum between 1 and 8 GeV/c is estimated to be $\pm 0.05\%$.

5. Scattering angle: Detailed survey of the spectrmeter, scattering chamber and the beam line were carried out before and after the experiment. The absolute error in spectrometer angle was $\pm 0.003°$, with a $\pm 0.0015°$ uncertainty in the reproduceability.

6. D_2 target density: Local density fluctuations in the liquid target due to heat deposition along the beam path were studied. Data were taken at substantially larger beam currents and duty cycle than nominal values for regular runs. Table III.III shows the cross sections obtained for these runs, and the average for the regular runs taken at the same kinematic setting. The variation in cross sections was less than the statistical errors, and therefore the effect from possible local heating of D_2 is determined as $\pm 0.2\%$ by scaling down to the normal beam current and duty cycle.

7. Acceptance: Acceptance studies are described in detail in Appendix

A. Monte Carlo study of spectrometer optics yielded an angle dependence of acceptance for the long D_2 target which was atmost 0.4% at the largest angle of 46°. The error on this correction is estimated to be $\pm 25\%$, which yields 0-0.1% error on cross sections. The error on the momentum dependence of acceptance, studied in the floating wire experiment, is estimated to be $\pm 0.1\%$.

8. e^+/e^- background: Background to deep inelastic scattering of electrons was estimated to be dominated by the photo-produced π^0 decays to two photons and subsequent photon-conversion at the end of the target. The possible kaon decay background as discussed earlier was negligible. The error due to the assumption of charge-symmetry of background is estimated to be typically 0.1%.

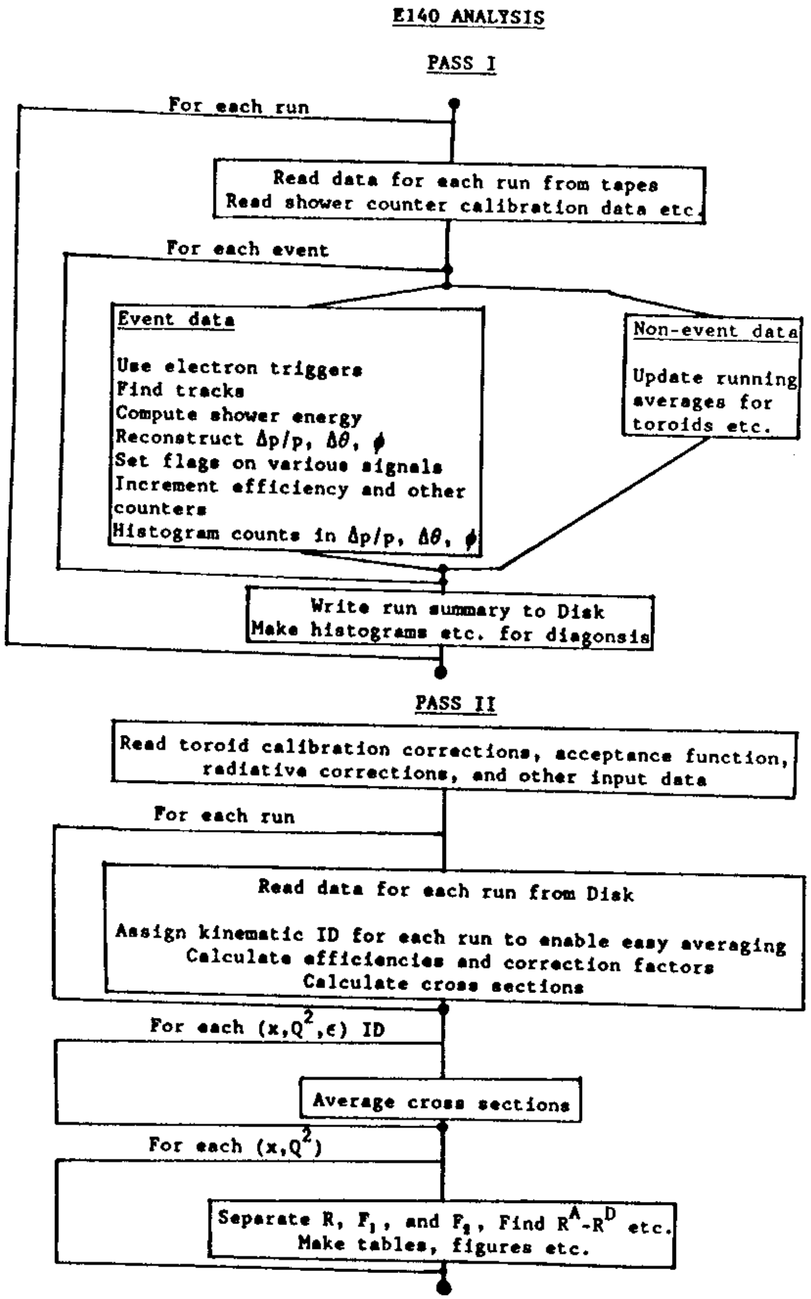

Fig. III.1 Flow chart of the analysis programs.

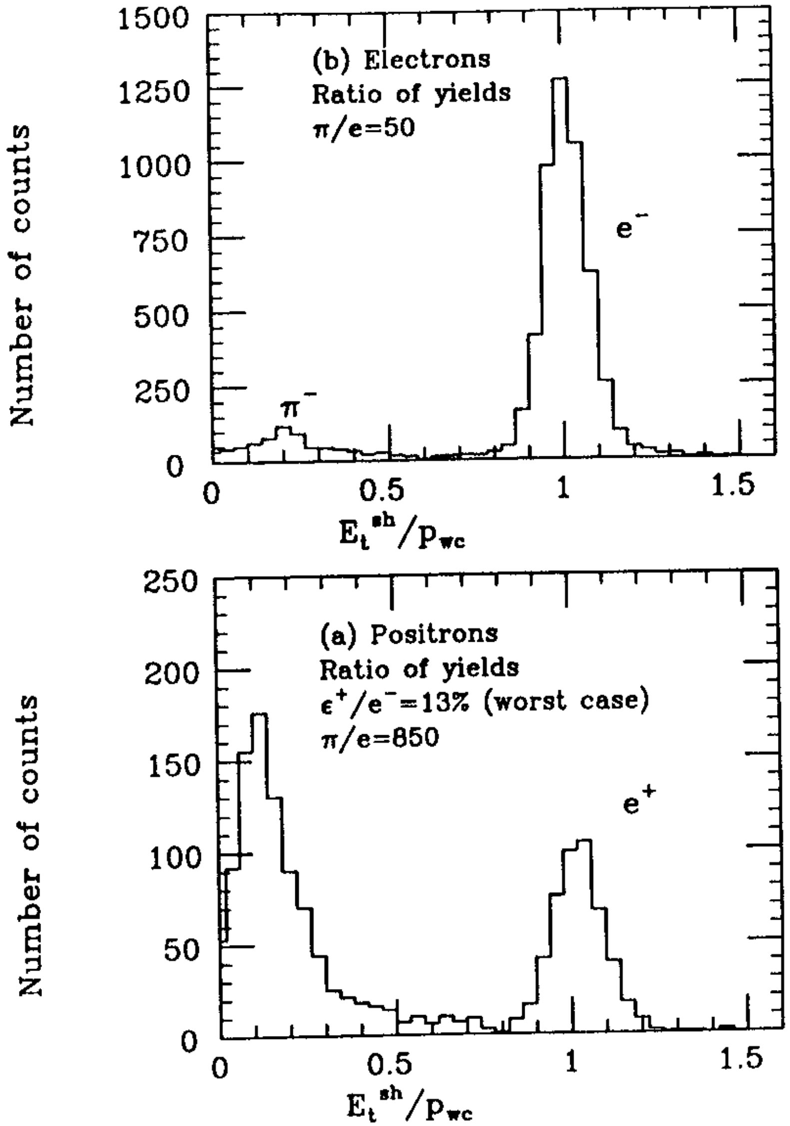

Fig. III.2 (a) Positron shower counter spectrum (cut on high Cherenkov signal and requiring a single track in the wire chambers) for the run with worst case of yields e^+/e^- (13%). The positron peak is clearly visible, and the background tail from the low energy region is less than 10%. Even if kaon contribution to the tail is 10%, the positron background is still accurate to 0.13% (there is additional statistical uncertainty on the e^+ background). (b) Electron shower counter spectrum at similar kinematics. The low energy background is identical to the positron spectrum.

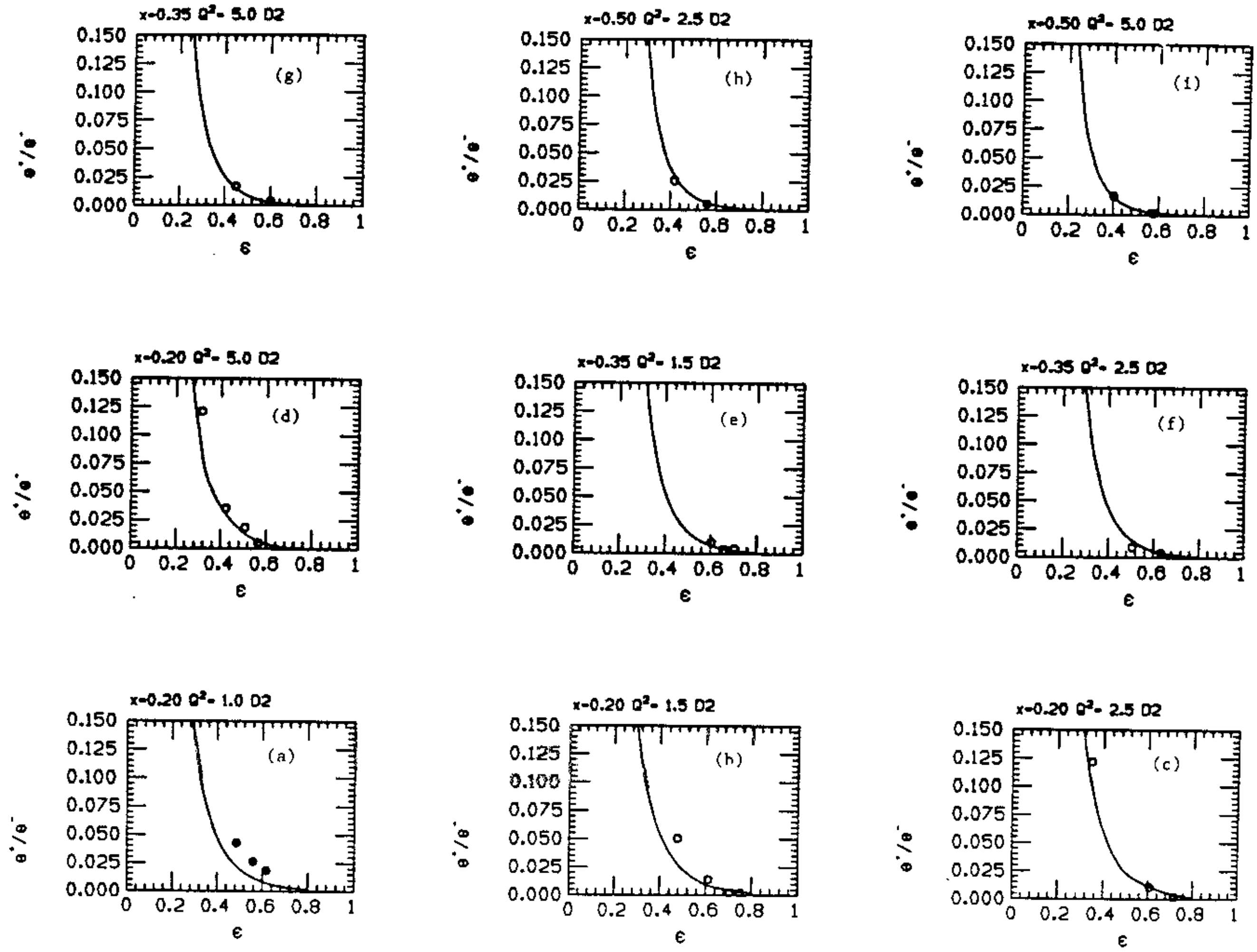
x=0.35 Q²= 5.0 D2
(g)
x=0.50 Q²= 2.5 D2
(h)
x=0.50 Q²= 5.0 D2
(i)
x=0.20 Q²= 5.0 D2
(d)
x=0.35 Q²= 1.5 D2
(e)
x=0.35 Q²= 2.5 D2
(f)
x=0.20 Q²= 1.0 D2
(a)
x=0.20 Q²= 1.5 D2
(h)
x=0.20 Q²= 2.5 D2
(c)
ε

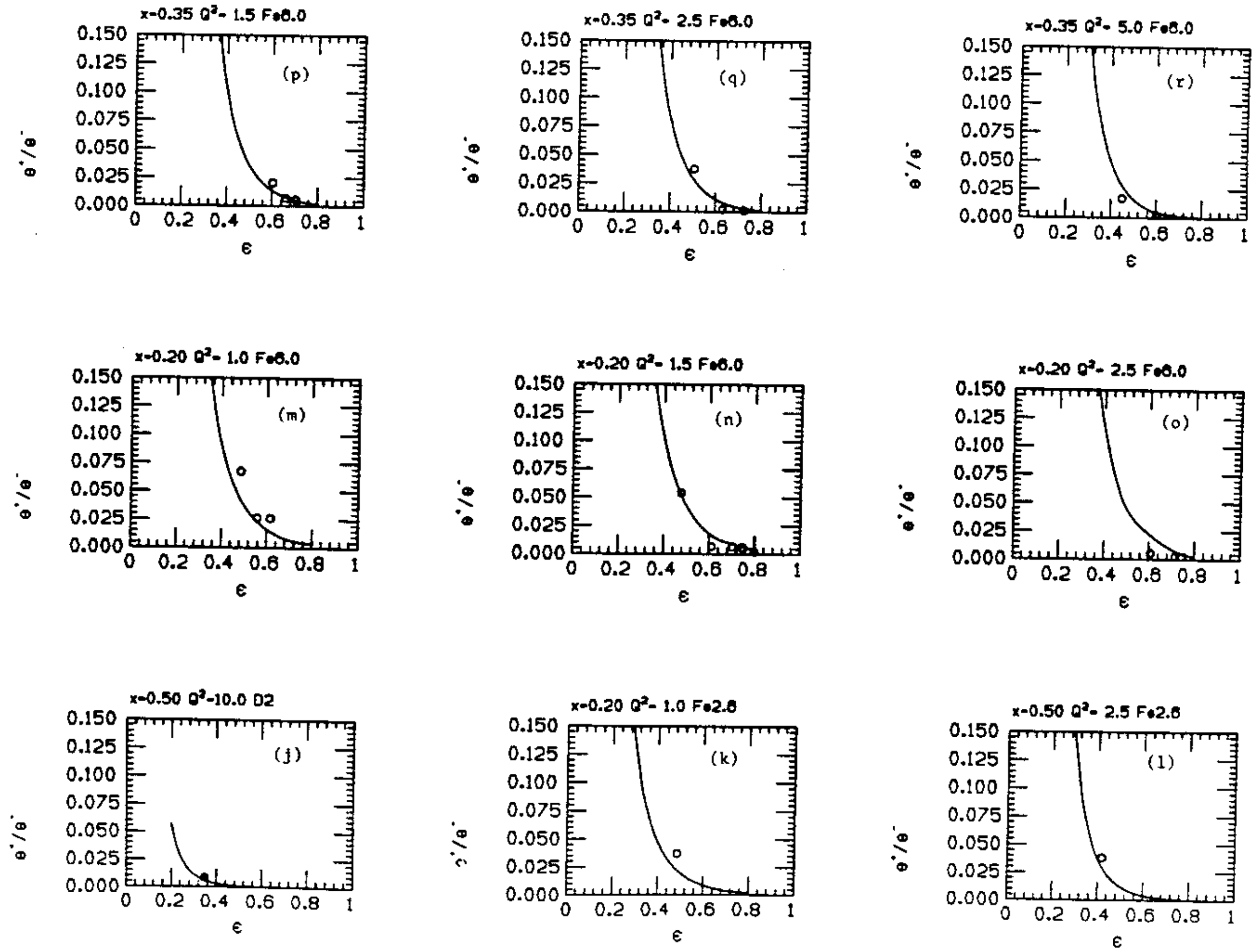
x=0.35 Q²= 1.5 Fe6.0
(p)
x=0.35 Q²= 2.5 Fe6.0
(q)
x=0.35 Q²= 5.0 Fe6.0
(r)
x=0.20 Q²= 1.0 Fe6.0
(m)
x=0.20 Q²= 1.5 Fe6.0
(n)
x=0.20 Q²= 2.5 Fe6.0
(o)
x=0.50 Q²=10.0 D2
(j)
x=0.20 Q²= 1.0 Fe2.6
(k)
x=0.50 Q²= 2.5 Fe2.6
(l)
ε

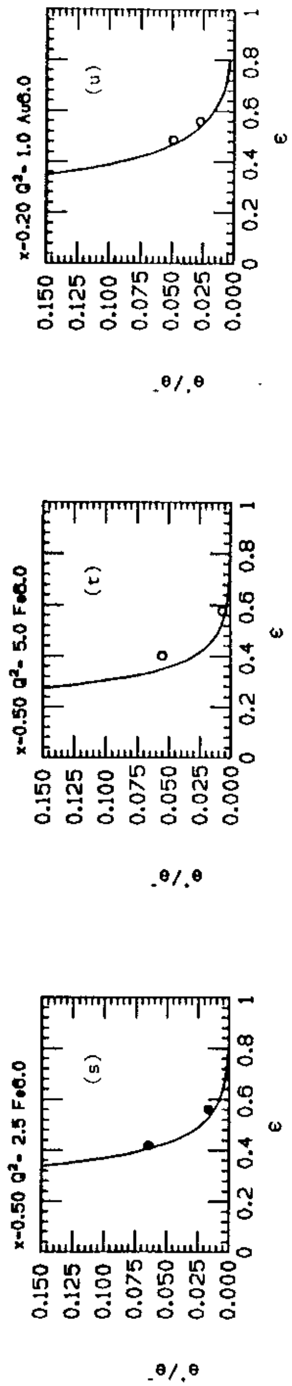

Fig. III.3 The ratios of yields e^+/e^- measured in this experiment are plotted versus ϵ for each (x,Q^2) setting. The solid line is a fit to e^+/e^- data obtained using data from earlier SLAC experiments. When the positron data were not taken this fit was used for subtraction.

TABLE III.I

Raw and radiatively corrected cross sections (in nb/sr GeV)

ϵ	E	E′	θ	Radiat. corr.	σ_{raw}	σ
D_2 :						
x=0.20 Q^2= 1.0						
0.485	3.748	1.084	28.728	0.777	23.5541	18.3063 ± 0.1612
0.559	4.006	1.342	24.906	0.806	30.7876	24.8241 ± 0.2251
0.616	4.251	1.586	22.205	0.828	39.3695	32.5861 ± 0.2709
0.846	6.251	3.586	12.124	0.914	145.9230	133.4028 ± 0.8858
0.792	5.507	2.843	14.520	0.891	97.9558	87.3080 ± 0.6656
x=0.20 Q^2= 1.5						
0.748	7.498	3.502	13.727	0.886	47.8351	42.3579 ± 0.2389
0.703	7.002	3.005	15.343	0.870	37.3359	32.4673 ± 0.1960
0.611	6.250	2.253	18.783	0.836	24.1857	20.2265 ± 0.1294
0.476	5.507	1.510	24.519	0.780	14.5505	11.3566 ± 0.1009
0.799	8.251	4.254	11.866	0.906	65.7086	59.5583 ± 0.3464
x=0.20 Q^2= 2.5						
0.348	8.251	1.589	25.220	0.723	5.2198	3.7750 ± 0.0534
0.606	10.243	3.582	14.999	0.851	13.6336	11.6036 ± 0.0430
0.716	11.744	5.083	11.746	0.891	22.6452	20.1656 ± 0.1447

contd.

ϵ	E	E′	θ	Radiat. corr.	σ_{raw}	σ
D_2 :						
x=0.20 Q^2= 5.0						
0.508	18.491	5.169	13.134	0.833	4.2534	3.5422 ± 0.0257
0.566	19.493	6.171	11.702	0.856	5.4133	4.6343 ± 0.0280
0.422	17.255	3.933	15.600	0.791	3.0679	2.4270 ± 0.0186
0.314	16.005	2.683	19.647	0.721	2.0554	1.4826 ± 0.0168
x=0.35 Q^2= 1.5						
0.604	3.748	1.464	30.304	0.936	12.1458	11.3696 ± 0.0807
0.660	4.007	1.723	26.950	0.955	15.4555	14.7569 ± 0.1059
0.704	4.250	1.966	24.459	0.971	18.8426	18.2980 ± 0.1371
0.907	7.002	4.718	12.232	1.074	83.2771	89.4729 ± 1.1421
0.838	5.507	3.223	16.715	1.027	42.9023	44.0649 ± 0.2902
x=0.35 Q^2= 2.5						
0.761	7.498	3.692	17.283	1.009	12.9672	13.0839 ± 0.0807
0.726	7.081	3.274	18.900	0.995	10.5962	10.5454 ± 0.0721
0.633	6.250	2.443	23.345	0.961	6.8143	6.5499 ± 0.0452
0.506	5.501	1.695	30.008	0.915	4.1535	3.8004 ± 0.0299
0.870	9.710	5.904	11.986	1.062	28.0217	29.7646 ± 0.2107

contd.

ϵ	E	E′	θ	Radiat. corr.	σ_{raw}	σ
D_2 :						
x=0.35 Q^2= 5.0						
0.777	15.004	7.391	12.189	1.040	5.8902	6.1241 ± 0.0358
0.704	13.320	5.707	14.735	1.012	3.9642	4.0129 ± 0.0233
0.601	11.753	4.140	18.447	0.976	2.4571	2.3981 ± 0.0143
0.449	10.243	2.630	24.878	0.919	1.3593	1.2496 ± 0.0123
x=0.50 Q^2= 2.5						
0.417	3.749	1.084	46.177	0.965	1.5652	1.5097 ± 0.0139
0.560	4.251	1.587	35.447	1.016	2.6155	2.6579 ± 0.0256
0.865	7.082	4.418	16.250	1.149	13.3384	15.3284 ± 0.0986
0.757	5.502	2.838	23.082	1.089	6.3173	6.8789 ± 0.0609
0.926	9.248	6.584	11.630	1.208	26.3787	31.8682 ± 0.2346
x=0.50 Q^2= 5.0						
0.401	7.084	1.755	36.976	0.985	0.4799	0.4726 ± 0.0063
0.863	13.316	7.987	12.448	1.180	4.4451	5.2469 ± 0.0278
0.578	8.250	2.921	26.331	1.051	0.9348	0.9823 ± 0.0073
0.712	9.710	4.381	19.742	1.099	1.7057	1.8751 ± 0.0137
x=0.50 Q^2= 7.5						
0.372	10.243	2.249	33.152	0.990	0.2363	0.2339 ± 0.0038
0.743	14.991	6.997	15.367	1.129	1.1321	1.2785 ± 0.0129

contd.

ϵ	E	E′	θ	Radiat. corr.	σ_{raw}	σ
D_2 :						
x=0.50 Q^2=10.0						
0.697	18.490	7.832	15.100	1.120	0.6037	0.6764 ± 0.0040
0.504	15.005	4.348	22.578	1.051	0.2657	0.2791 ± 0.0033
0.348	13.319	2.661	30.802	0.991	0.1472	0.1459 ± 0.0018
Fe (2.6% rl) :						
x=0.20 Q^2= 1.0						
0.485	3.749	1.084	28.720	0.797	23.1338	18.4377 ± 0.2523
0.559	4.006	1.342	24.906	0.823	30.5526	25.1570 ± 0.2162
0.616	4.250	1.586	22.210	0.843	38.9312	32.8307 ± 0.2618
0.846	6.250	3.586	12.125	0.924	144.5807	133.5782 ± 0.8793
0.792	5.506	2.842	14.524	0.902	97.0869	87.5724 ± 0.7034
x=0.50 Q^2= 2.5						
0.926	9.248	6.584	11.630	1.196	24.6685	29.4986 ± 0.2194
0.418	3.751	1.086	46.115	0.992	1.3911	1.3796 ± 0.0253

contd.

ϵ	E	E′	θ	Radiat. corr.	σ_{raw}	σ
Fe (6% rl) :						
x=0.20 Q2= 1.0						
0.485	3.749	1.084	28.720	0.745	25.1048	18.7081 ± 0.2420
0.559	4.006	1.342	24.906	0.780	33.5633	26.1727 ± 0.2324
0.616	4.250	1.586	22.210	0.806	40.6238	32.7590 ± 0.3875
0.846	6.250	3.586	12.125	0.918	147.2643	135.2328 ± 0.8936
0.792	5.506	2.842	14.524	0.887	100.0047	88.7342 ± 0.7200
x=0.20 Q2= 1.5						
0.748	7.498	3.501	13.728	0.880	48.9135	43.0439 ± 0.2985
0.703	7.003	3.006	15.341	0.859	39.0388	33.5265 ± 0.1980
0.611	6.250	2.253	18.783	0.816	25.8125	21.0681 ± 0.1286
0.476	5.507	1.510	24.519	0.748	15.8450	11.8521 ± 0.1171
0.799	8.251	4.254	11.866	0.907	66.5867	60.3742 ± 0.3456
x=0.20 Q2= 2.5						
0.348	8.250	1.589	25.224	0.681	5.4209	3.6906 ± 0.0574
0.606	10.243	3.582	14.999	0.834	14.2802	11.9154 ± 0.0722
0.716	11.744	5.083	11.746	0.885	23.3869	20.6903 ± 0.1550

contd.

ϵ	E	E´	θ	Radiat. corr.	σ_{raw}	σ
Fe (6% rl) :						
x=0.35 Q2= 1.5						
0.604	3.749	1.465	30.298	0.958	11.7767	11.2774 ± 0.1099
0.660	4.007	1.723	26.950	0.982	15.1599	14.8794 ± 0.1170
0.704	4.250	1.966	24.459	1.002	18.1889	18.2217 ± 0.1390
0.907	7.002	4.718	12.232	1.133	80.2858	90.9557 ± 1.1261
0.838	5.507	3.223	16.715	1.074	40.8606	43.8843 ± 0.3513
x=0.35 Q2= 2.5						
0.761	7.498	3.692	17.283	1.049	12.4382	13.0514 ± 0.0853
0.726	7.081	3.274	18.900	1.031	10.2372	10.5597 ± 0.0726
0.633	6.250	2.444	23.342	0.989	6.6176	6.5428 ± 0.0582
0.506	5.501	1.695	30.008	0.930	3.9382	3.6617 ± 0.0410
0.870	9.710	5.904	11.986	1.117	26.6173	29.7422 ± 0.1957
x=0.35 Q2= 5.0						
0.777	15.005	7.392	12.188	1.083	5.5656	6.0298 ± 0.0377
0.704	13.320	5.708	14.734	1.050	3.7311	3.9162 ± 0.0280
0.601	11.753	4.140	18.447	1.003	2.3542	2.3622 ± 0.0179
0.449	10.243	2.630	24.878	0.933	1.3015	1.2141 ± 0.0154

contd.

ϵ	E	E´	θ	Radiat. corr.	σ_{raw}	σ
Fe (6% rl) :						
x=0.50 Q2= 2.5						
0.418	3.749	1.085	46.164	1.012	1.3942	1.4109 ± 0.0152
0.560	4.251	1.587	35.447	1.074	2.2743	2.4421 ± 0.0247
0.865	7.082	4.418	16.251	1.236	11.4962	14.2047 ± 0.0938
0.757	5.502	2.838	23.082	1.163	5.5822	6.4949 ± 0.0689
0.926	9.248	6.584	11.630	1.307	22.9321	29.9746 ± 0.2166
x=0.50 Q2= 5.0						
0.401	7.084	1.755	36.976	1.033	0.4324	0.4468 ± 0.0100
0.863	13.314	7.985	12.450	1.271	3.8738	4.9236 ± 0.0380
0.578	8.250	2.921	26.331	1.115	0.8318	0.9274 ± 0.0097
0.712	9.710	4.381	19.742	1.175	1.4876	1.7477 ± 0.0162
Au (6% rl) :						
x=0.20 Q2= 1.0						
0.485	3.748	1.084	28.728	0.757	24.7281	18.7092 ± 0.2711
0.559	4.006	1.342	24.906	0.790	32.3820	25.5753 ± 0.2439
0.616	4.250	1.586	22.210	0.816	40.7876	33.2623 ± 0.2439
0.845	6.250	3.585	12.127	0.925	146.8095	135.7547 ± 0.8684
0.792	5.506	2.842	14.524	0.894	98.9810	88.5088 ± 0.7105

TABLE III.II

Typical systematic uncertainties

SOURCE	UNCERTAINTY	ERROR (±)			
	%	$\Delta\sigma$ %	ΔR	$\Delta(\sigma^A/\sigma^D)$ %	$\Delta(R^A-R^D)$
Incident Energy	0.1	0.3	0.014	0.3	0.014
Beam Steering	0.003°	0.1	0.005	0.1	0.004
Charge Mearsurement	0.3	0.3	0.014	0.1	0.004
D Target Density	0.2	0.2	0.009	0.2	0.010
Scattered Energy	0.05	0.1	0.005	-	-
Spectrometer Angle	0.002°	0.1	0.005	-	-
Acceptance vs p	0.1	0.1	0.005	-	-
D Acceptance vs θ	0.1	0.1	0.005	0.1	0.004
Detector Efficiency	0.1	0.1	0.005	-	-
e^+/e^- Background	0.1	0.1	0.005	0.1	0.004
Neutron Excess	0.2	0.2	-	0.2	-
TOTAL POINT-TO-POINT		0.5	0.025	0.4	0.019
Radiative Corrections					
ϵ-dependent	1.0	1.0	0.030	0.5	0.015
normalization	1.0	1.0	-	-	-
Beam Charge	2.0	2.0	-	-	-
Target Length	1.0	1.0	-	1.0	-
Acceptance	2.0	2.0	-	-	-
TOTAL ABSOLUTE ERROR		3.3	0.030	1.1	0.015

TABLE III.III

D_2 target density study. Cross sections (σ)† obtained at various beam currents (I) and duty cycles (τ) are compared. Nominal value of $I\tau$ was 300 mA/s

$I\tau$	σ
502	1.5345 ± 0.0528
558	1.5744 ± 0.0274
740	1.6041 ± 0.0383
937	1.5848 ± 0.0290
1235	1.5663 ± 0.0473
1546	1.5596 ± 0.0190
1852	1.5605 ± 0.0216
3191	1.5638 ± 0.0140

† Charge symmetric, target endcap background was not subtracted.

REFERENCES

[III.1] R. G. Arnold et al., Phys. Rev. Lett. 52, 724 (1984); SLAC-PUB-3257 (1983).

[III.2] S. Dasu et al., Proceedings of the XXXII International Conference on High Energy Physics, (Berkeley, 1986), Ed. S. C. Loken (World Scientific 1987).

[III.3] R. C. Walker, Ph. D. thesis (in preparation), Cal Tech.

[III.4] The naive extrapolation of the low energy tail of shower spectrum to region $E_t^{sh}/p_{wc} > 0.7$ (see Fig. II.9) over estimates the background, as at the trigger level there is a bias towards the high shower events. Therefore, in order to estimate the pion contamination, an unbiassed sample was chosen by requiring additional signals.

[III.5] A. Bodek, Ph. D. thesis (1968), MIT report no. COO-3069-116.

[III.6] A. Bodek et al., Phys. Rev. D 20, 1471 (1979).

[III.7] L. S. Rochester et al., Phys. Rev. Lett. 36, 1284 (1976).

[III.8] Although the H_2 inelastic data was rendered useless due the collapse of a thin aluminum tube in the target, the elastic peak data could be resurrected. The contributions from the collapsed tube and the endcaps were identical and were in the region $x > 1$. Since the endcap contributions were measured at each elastic kinematic setting, a correction could be made. The positions of elastic peaks measured in this analysis are used to check the calibration of E, E′ and θ. See reference [III.3] for details.

IV $R=\sigma_L/\sigma_T$ AND F_2 EXTRACTION

A. Introduction

The ratio $R=\sigma_L/\sigma_T$ measured in deep inelastic lepton-nucleon scattering is a sensitive measure of the spin and the transverse momentum of the nucleon constituents, and the mass scales involved in the hadronic matter. Within the naive parton model with spin-1/2 partons, R values are expected to be small, and to decrease rapidly with increasing Q^2. With spin-0 partons, R values are expected to be large and to increase with increasing Q^2. Previous measurements [IV.1-3] of the quantity R, at the Stanford Linear Accelerator Center, indicated that scattering from spin-1/2 constituents (e.g. quarks) dominates. However, the results for R were larger than expected (see Fig. I.6), and were consistent with a constant value of 0.2. The errors on those results left room for speculations of additional spin-0 constituents in nucleons [IV.4] (e.g. tightly bound diquarks), and of unexpectedly large transverse momentum (p_T) for quarks. Experiments [IV.2] in the SLAC Q^2 range have also indicated deviations from the scaling of the structure functions $F_{1,2}$ in the variable x. In the theory of Quantum Chromodynamics, scaling violations [IV.5] occur due to quark-gluon interactions and give contributions to the p_T of quarks. Target mass effects [IV.6,7] also introduce violations of scaling, and yield contributions to $F_{1,2}$ which are proportional to powers of M^2/Q^2. These two effects lead to non-zero contributions to R which decrease with increasing Q^2. Since the quality of the previous data was inadequate to test such predictions, we have made precision measurements of the ratio R and the structure functions F_1 and F_2. In addition to testing the QCD theory of nucleon structure, our measurements of R improve the precision of structure functions extracted from previous SLAC data [IV.2].

B. Results

The values of R, F_1 and F_2 were extracted from cross sections measured at various values of ϵ at fixed (x,Q^2) by making linear fits to Σ versus ϵ:

$$\Sigma(x,Q^2,\epsilon) = \sigma_T(x,Q^2) + \epsilon\, \sigma_L(x,Q^2), \tag{IV.1}$$

$$R=\frac{\sigma_L}{\sigma_T},\ F_1=\frac{MK}{4\pi^2\alpha}\sigma_T,\ \text{and}\ F_2=\frac{\nu K}{4\pi^2\alpha}\left(\frac{Q^2}{Q^2+\nu^2}\right)(\sigma_T+\sigma_L)\ \text{where}\ K=\frac{W^2-M^2}{2M}.$$

The values of Σ were weighted by the quadratic sum of statistical and point-to-point (i.e. ϵ-dependent) systematic errors in making the linear fits. The fits at each (x,Q^2) point for all targets are shown in Figs. IV.1a-v. The average χ^2/df for these fits is 0.7, indicating that the estimate of point-to-point systematic uncertainty is conservative. The fits were also made with only statistical errors on cross sections to find the individual contributions to the error. The values for R and F_2, with statistical and systematic errors, obtained for all (x,Q^2) points and targets are shown in Table IV.1. The values of R are <u>insensitive</u> to the <u>absolute normalization</u> of beam flux, target length, radiative corrections and spectrometer acceptance. In

addition to the point-to-point systematic error shown in Table IV.1, there is an uncertainty of $\pm$0.03 on R due to ϵ-dependent errors on radiative corrections. However, the F_2 results require the absolute normalizations (presently known to about $\pm$3.3%), and are still preliminary.

The results for R plotted in Figs. IV.2 and IV.3 were averaged for different targets at same x and Q^2, because the values of the differences R^A-R^D are consistent with zero (discussed in the next chapter). Our R results have small errors compared to previous SLAC experiments [IV.2,3] (see Fig. IV.4) because a) our cross sections were measured to better than $\pm$1% statistical accuracy with large ϵ-separation, b) uncertainties in radiative corrections were reduced to below $\pm$1% level, and c) a single spectrometer with well determined acceptance was used. Our results at x of 0.2, 0.35 and 0.5, show a clear falloff of R with increasing Q^2. The agreement with a constant value of R=0.2 is poor (χ^2=3.4/df). The high Q^2 results from CDHS [IV.8] and BCDMS [IV.9] collaborations for ν-Fe and μ-C/H scattering respectively, are also plotted on Fig. IV.2. These results reinforce the conclusion that R decreases with increasing Q^2. The results plotted against x, for Q^2 values of 1.5, 2.5 and 5 GeV^2, in Figs. IV.3 show only a weak dependence on the variable x in this x-range.

The values of F_1 and F_2 obtained from the Σ versus ϵ fits are plotted against Q^2 at various x in Fig. IV.5 and Fig. IV.6. The results for $F^D_{1,2}$ were corrected by a fit to the EMC effect (correction factors are 1.02, 0.99 and 0.94 at x of 0.2, 0.35 and 0.5 respectively) to compare directly with $F^{Fe}_{1,2}$ calculations. A weak Q^2

dependence, that is a fall of $F_{1,2}(x,Q^2)$ with increasing Q^2, due to scaling violations is evident. Note that only statistical and point-to-point systematic errors are plotted.

As discussed in Chapter I, within naive parton model [IV.10] the Bjorken scaling of the structure functions is exact, i.e. F_2 $(=2xF_1)$ is a function of x alone. Our data show a clear dependence on Q^2, as has been observed in previous experiments [IV.2]. The contribution to R in the naive parton model (see Equation I.5), arises only from the kinematic terms, and as shown in Figs. IV.2a-c and IV.3a-c our data are not in agreement with this prediction (χ^2=7.1/df). Theoretical predictions based on QCD, including the target mass effects, discussed below, are also plotted on Figs. IV.2-6.

C. Comparisions with the theory of scaling violations

1. Perturbative Quantum Chromodynamics

In perturbative QCD (to the order α_s) hard gluon bremsstrahlung from quarks, and photon-gluon interaction effects yield contributions to leptoproduction [IV.5]. Therefore, the calculation of structure functions in QCD requires the knowledge of quark and gluon distribution functions. The quark and gluon x-distributions are extracted from neutrino-nucleon scattering data at high Q^2. Perturbative QCD enables calculation of quark and gluon momentum distributions at other Q^2 values using Altarelli-Parisi equations [IV.11]. The Q^2-evolution of these distributions has been parameterized by various groups [IV.12]. The Q^2-evolution fits for

quark (q), anti-quark ($\bar{q}$) and gluon (G) distribution functions extracted from CDHS were used to calculate quark-gluon interaction [IV.5] and target mass effects [IV.6,7]. Fig. IV.7 shows these quark-gluon momentum distributions at Q^2=5 GeV^2. A factor of 1.12 was applied to renormalize the CDHS quark distributions to the new total ν-Fe cross section measurements [IV.13]. The QCD structure functions are given by [IV.5]:

$$2xF_1^{QCD}(x,Q^2) = \sum_i e_i^2\, x\left[q_i(x,Q^2)+\bar{q}_i(x,Q^2)\right],$$

$$F_L^{QCD}(x,Q^2) = \frac{\alpha_s(Q^2)}{2\pi}\, x^2 \left\{\int_x^1 \frac{du}{u^3}\left[\frac{8}{3}\, 2xF_1^{QCD}(u,Q^2) + 4(\Sigma e_i^2)\, uG(u,Q^2)(1-x/u)\right]\right\} + F_L^{Charm},$$

$$F_2^{QCD}(x,Q^2) = F_L^{QCD} + 2xF_1^{QCD}, \text{ and}$$

$$R^{QCD}(x,Q^2) = F_L^{QCD}/(2xF_1^{QCD}),$$

where, $F_L^{Charm}(x,Q^2) = \dfrac{\alpha_s(Q^2)}{\pi}\, \dfrac{4}{9} \displaystyle\int_{ax}^{1} \frac{du}{u}\, f_c(x/u,Q^2)\, uG(u,Q^2)$,

$$f_c(z,Q^2) = 2z^2(1-z)v - \frac{4m_c^2}{Q^2}\, z^3 \ln\frac{1+v}{1-v}\ ,\quad v^2=1-\frac{4m_c^2}{Q^2}\frac{z}{1-z},\quad a=1+\frac{4m_c^2}{Q^2},\quad m_c=1.25$$

$$\alpha_s(Q^2) = \frac{12\pi}{25\ln(Q^2/\Lambda^2)},\ \Lambda=0.25 \text{ GeV/c and } \Sigma e_i^2=2/3 \text{ for 3 flavors.}$$

The first and second terms in the integrand for F_L^{QCD} correspond to the hard gluon bremsstrahlung and photon-gluon interaction effects respectively. F_L^{Charm} term [IV.14] corresponds to the contribution due to threshold production of charm, i.e. $\gamma^* g \longrightarrow c\bar{c}$. The leading Q^2 dependence of the structure functions is in α_s, and is therefore logarithmic. In this calculation of F_L all kinematic terms of the order M^2/Q^2 were ignored. Our data on R (see Figs. IV.2 and IV.3) are not in agreement with these calculations (χ^2/df=9). The scaling violations in F_2 data (see Fig. IV.6a-c) are also not described completely by these QCD interaction effects alone.

2. Target mass effects

The kinematic effects due to target mass dominate at small Q^2 and large x. These effects have been first calculated in the framework of operator product expansion and moment analysis [IV.6] by Georgi and Politzer (GP). The structure funcutions including these GP target mass effects are given by:

$$2F_1^{QTM}(x,Q^2) = \frac{1}{k}\,\frac{2xF_1^{QCD}(\xi,Q^2)}{\xi} + \frac{2M^2}{Q^2}\,\frac{x^2}{k^2}\,I_1 + \frac{4M^4}{Q^4}\,\frac{x^3}{k^3}\,I_2$$

$$F_2^{QTM}(x,Q^2) = \frac{x^2}{k^3}\,\frac{F_2^{QCD}(\xi,Q^2)}{\xi^2} + \frac{6M^2}{Q^2}\,\frac{x^3}{k^4}\,I_1 + \frac{12M^4}{Q^4}\,\frac{x^4}{k^5}\,I_2$$

$$R^{QTM}(x,Q^2) = \frac{F_2^{QTM}}{2xF_1^{QTM}}\,k^2 - 1$$

where $k = \left(1+\frac{4x^2M^2}{Q^2}\right)^{1/2}$, Nachtman variable $\xi = \frac{2x}{1+k}$, and

$$I_1 = \int_\xi^1 du\,\frac{F_2^{QCD}(u,Q^2)}{u^2} \quad \text{and} \quad I_2 = \int_\xi^1 du \int_u^1 dv\,\frac{F_2^{QCD}(v,Q^2)}{v^2}\ .$$

Note that the target mass effects (ξ-scaling) introduce M^2/Q^2 terms.

Our data for R are in good agreement (χ^2=1.1/df) with QCD theory when the GP target mass effects are included. The weak x dependence of R, observed in our data, is also in agreement with the R^{QTM} predictions (see Figs. IV.3).

However, there has been a controversy [IV.15] regarding this kinematical ξ-scaling analysis of Georgi and Politzer. A natural (but non-unique) resolution of the mathematical inconsistencies in the original GP ξ-scaling analysis was proposed by Johnson and Tung [IV.7]. The technical and numerical differences between the two schemes are discussed in detail in Appendix D.

3. Uncertainties in QCD calculations

The QCD predictions for R are rather insensitive to the absolute normalization of the quark distributions. To check the sensitivity of these R calculations to input quark distributions, R and F_2 values were also calculated using Duke and Owens Set-I (DO) parameterization (see Figs. IV.8 and IV.9). The DO F_2 calculations are in disagreement with our data at low x. Therefore, there is a significant difference between calculated values of R using CDHS versus DO distributions at low x. However, this difference between CDHS and DO distributions does not indicate the theoretical uncertainty in R.

4. Non-perturbative effects

Alternately, scaling violations could possibly be explained by non-perturbative effects. For instance, it has been proposed [IV.4] that tightly bound spin-0 diquark (M_D^2=10 GeV^2) formation dominates at

SLAC values of Q^2 ($1 \le Q^2$ 10 GeV^2). These non-perturbative effects are intertwined with quark-gluon interaction effects at low x ($x \le 0.4$), but are measurable at large x. Our measurements at x=0.5 (see Fig. IV.2a) are consistently smaller than the predictions of Ekelin and Fredriksson.

The perturbative QCD calculations, with only GP kinematic target mass corrections, appear to account for all the $1/Q^2$ dependence of our R data as discussed earlier, and therefore, the speculations that dynamical higher twist contributions to R are large (for $x \lesssim 0.5$ at SLAC values of Q^2) are not favored. However, further experimentation at large x is needed to reach definitive conclusions.

D. Parameterization of R

An emperical parameterization of perturbative QCD calculations of R, with an additional $1/Q^2$ term fitted by our data, is given by:

$$R(x,Q^2) = \left[\frac{\alpha(1-x)^{\beta}}{\ln(Q^2/\Lambda^2)} + \frac{\gamma(1-x)^{\delta}}{Q^2} \right],$$

where, α=1.11, β=3.34, γ=0.11, δ=-1.94 and Λ=0.2 GeV.

The functional form of the fit was inspired by the dominant logarithmic Q^2 dependence of the QCD terms, and $1/Q^2$ dependence of target mass terms. The x-dependence of this parameterization was obtained by making least squares fits.

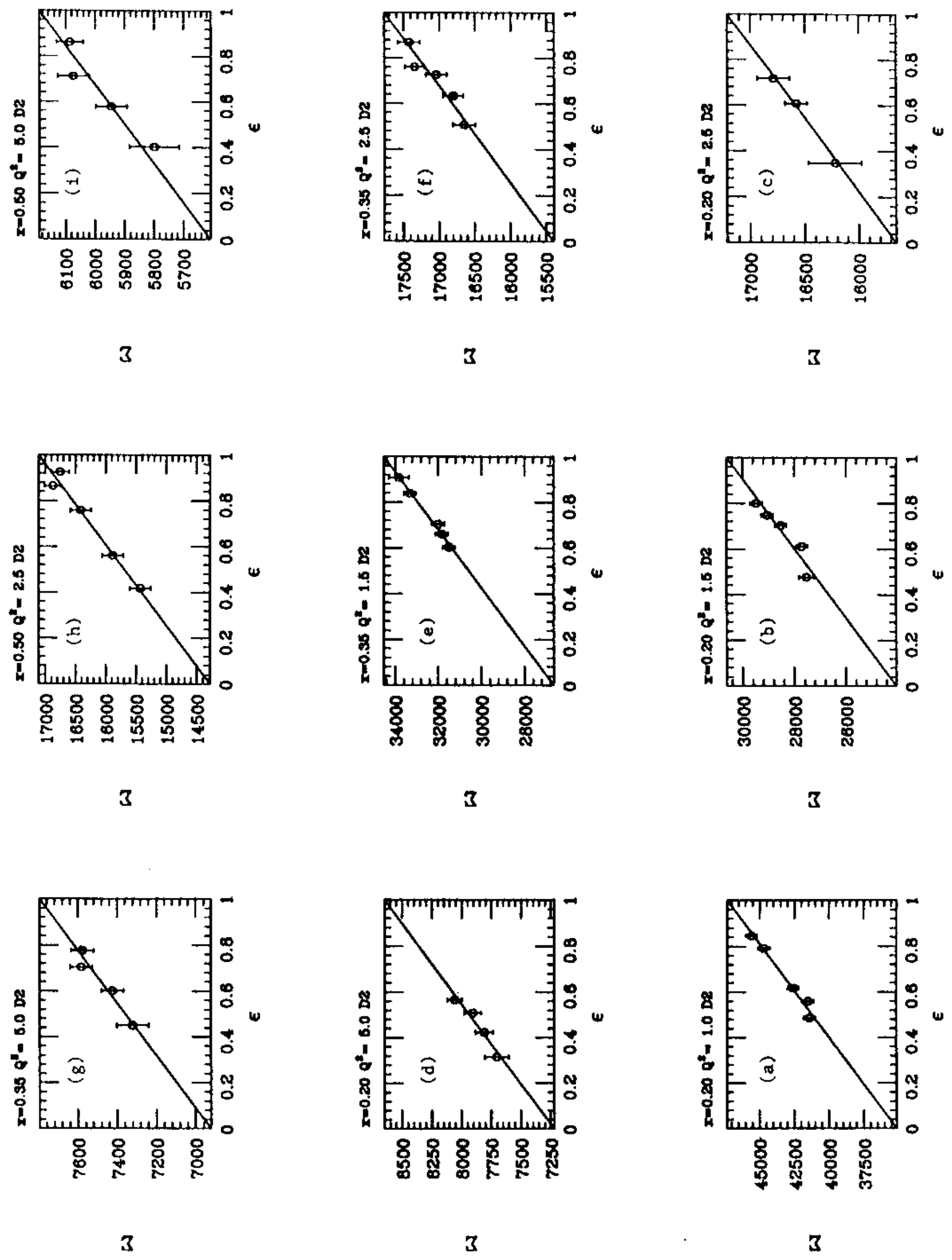

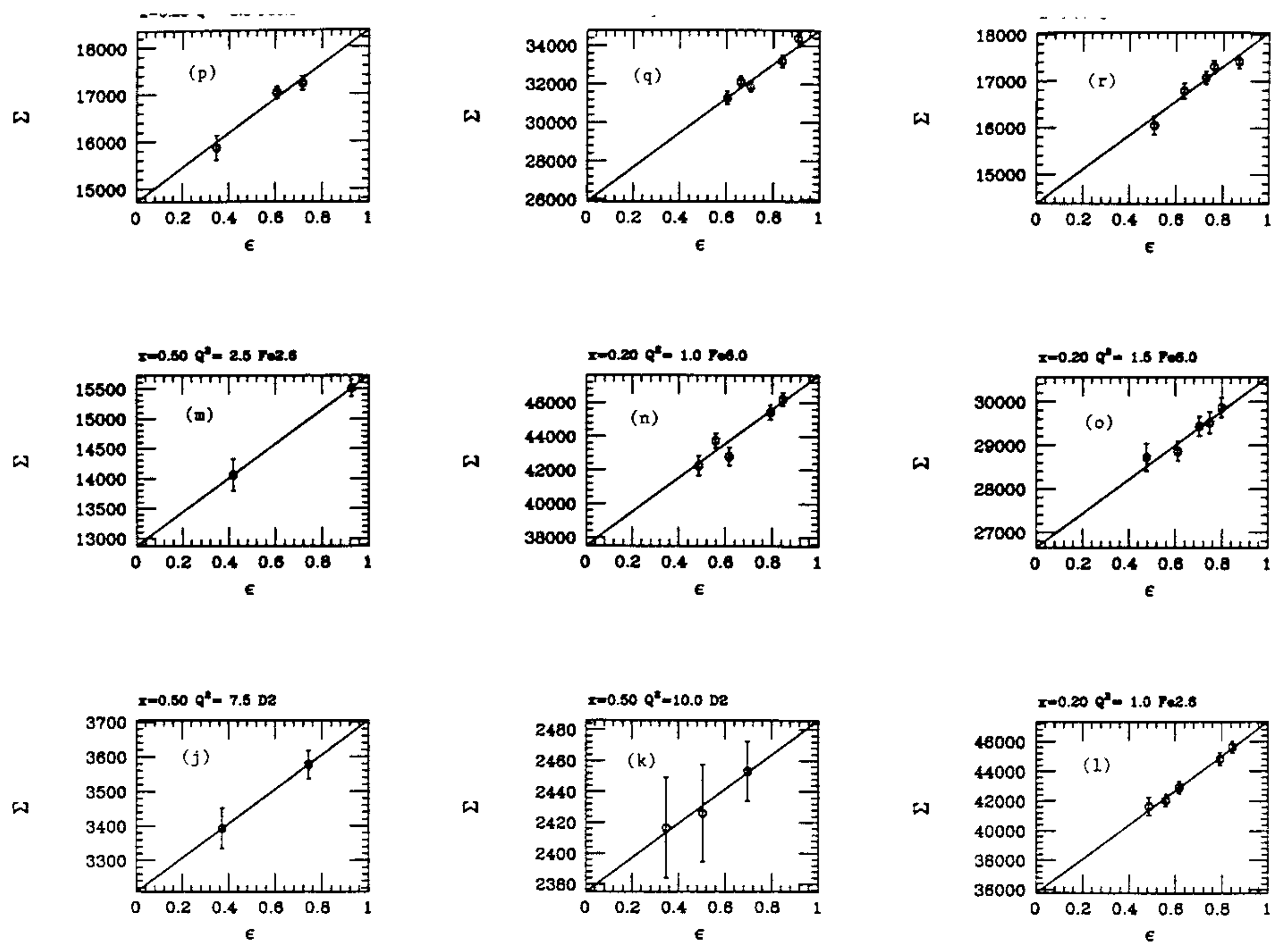

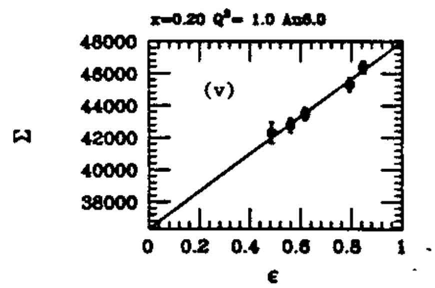

Figs. IV.1 The Σ vs ϵ fits at each (x,Q^2) point, for every target are shown in Figs. a-v. The scale on the y-axis is limited by the values of σ_L and $\sigma_L+\sigma_T$ so that the slope is visible. The errors on the cross sections include both the statistical and point-to-point (ϵ-dependent) systematic errors, added in quadrature. The χ^2/df is excellent ($\langle\chi^2/df\rangle$=0.7), indicating that the point-to-point fluctuations are at the most over estimated. It is to be noted that the errors radiative correction could cause an ϵ-dependent slope, which results in an overall systematic error in R of $\pm$0.03. The results of the fit, R, F_1 and F_2 are listed in Table IV.I in the same order as these figures.

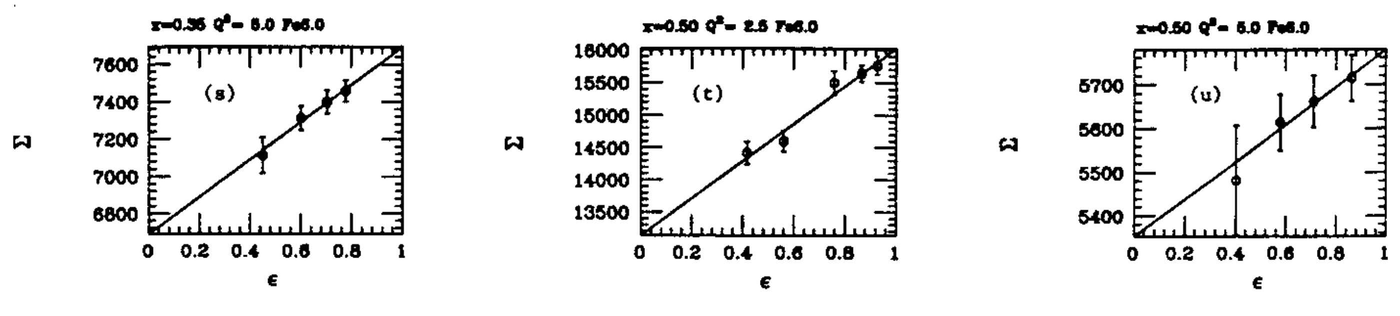

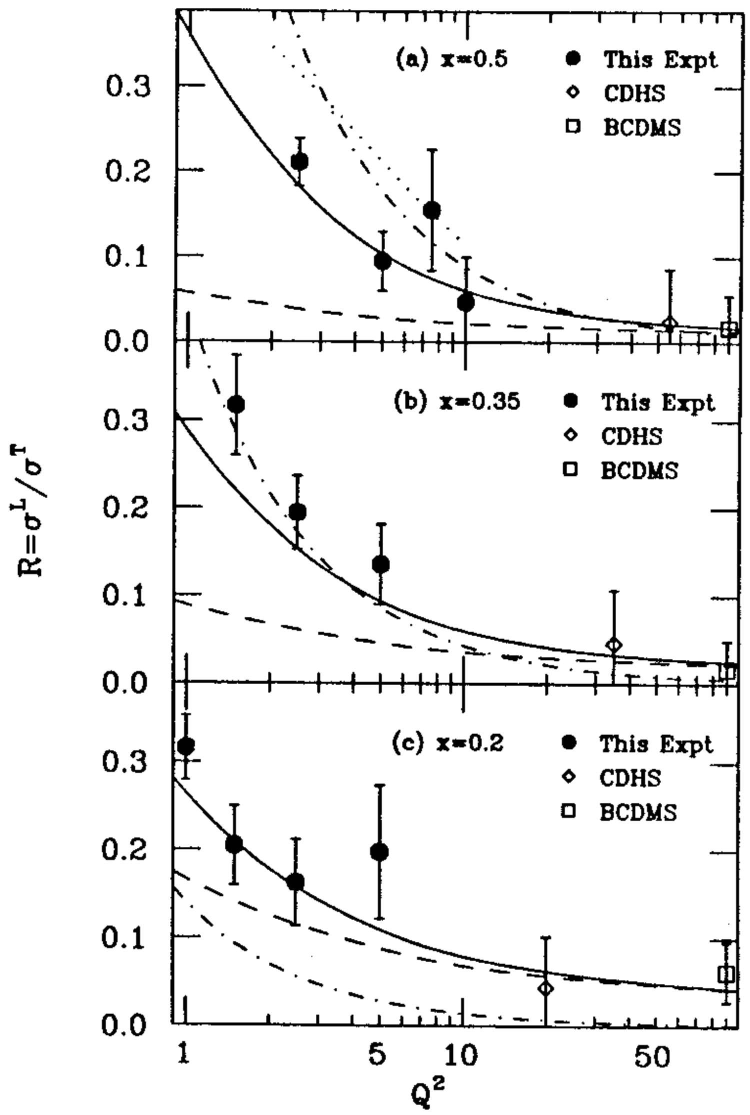

Figs. IV.2 The values of R at different x (0.2, 0.35 and 0.5) are plotted versus Q^2, with all statistical and systematic errors added in quadrature. Predictions from naive parton model (dot-dash curve), perturbative QCD (quark-gluon interaction effects; the dash curve), QCD with Georgi and Politzer target mass effects (solid curve), and Ekelin and Fredriksson diquark model (dot curve at x=0.5) are shown. The data from high Q^2 CDHS (ν-Fe) and BCDMS (μ-C/H) experiments are also plotted.

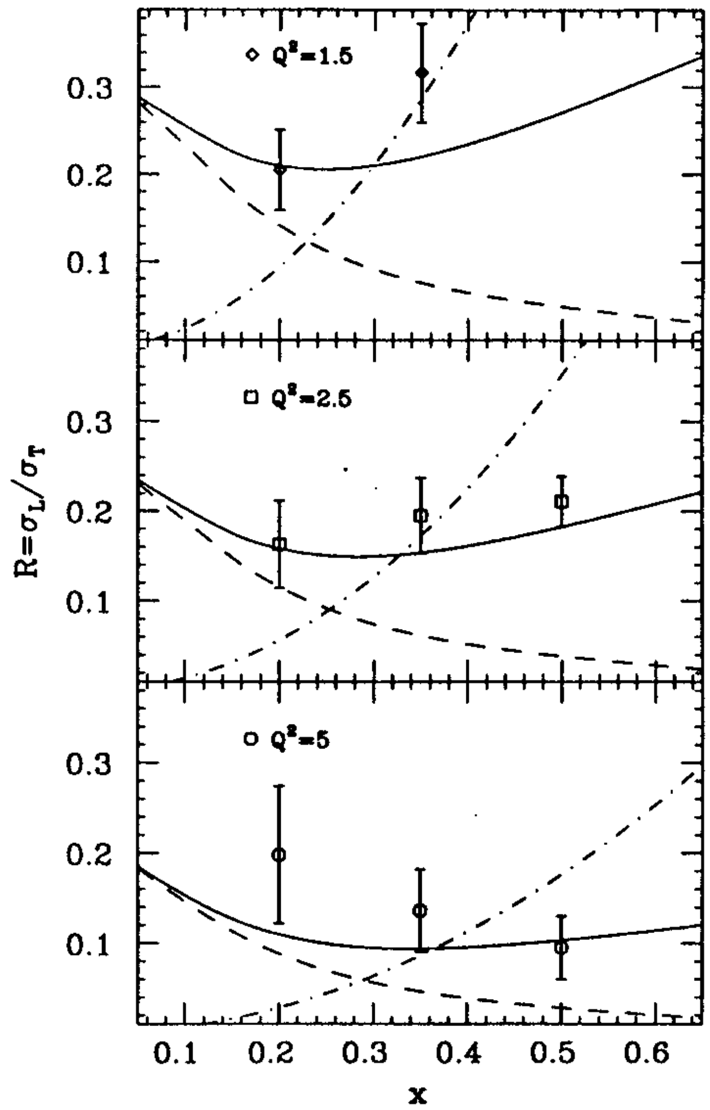

Figs. IV.3 The values of R at $Q^2=1.5$, 2.5 and 5 GeV^2 are plotted against x in (a), (b) and (c) respectively. The errors shown include all statistical and systematic errors added in quadrature. Predictions from naive parton model (dot-dash curve), perturbative QCD (dash curve) and QCD including target mass effects (solid curve) are also plotted.

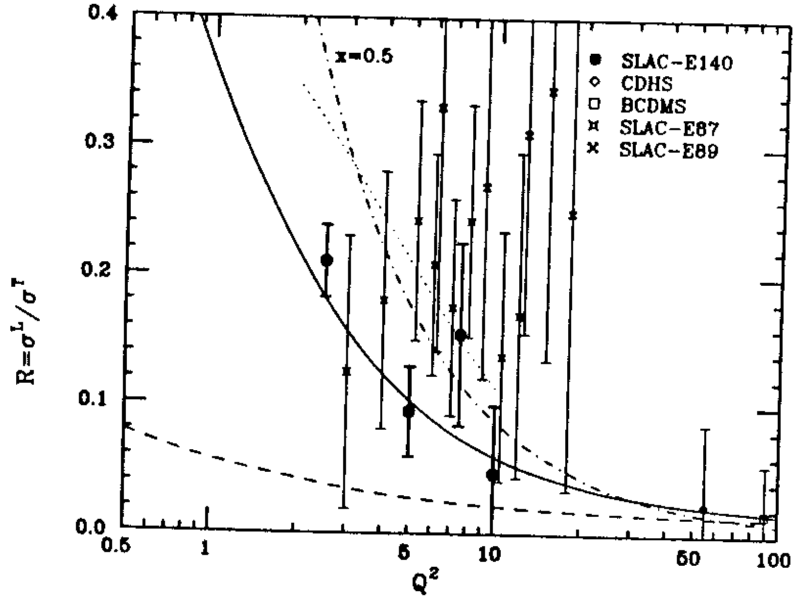

Fig. IV.4 Our data is compared to previous SLAC experiments. The theoretical predictions are the same as in Fig. IV.2a

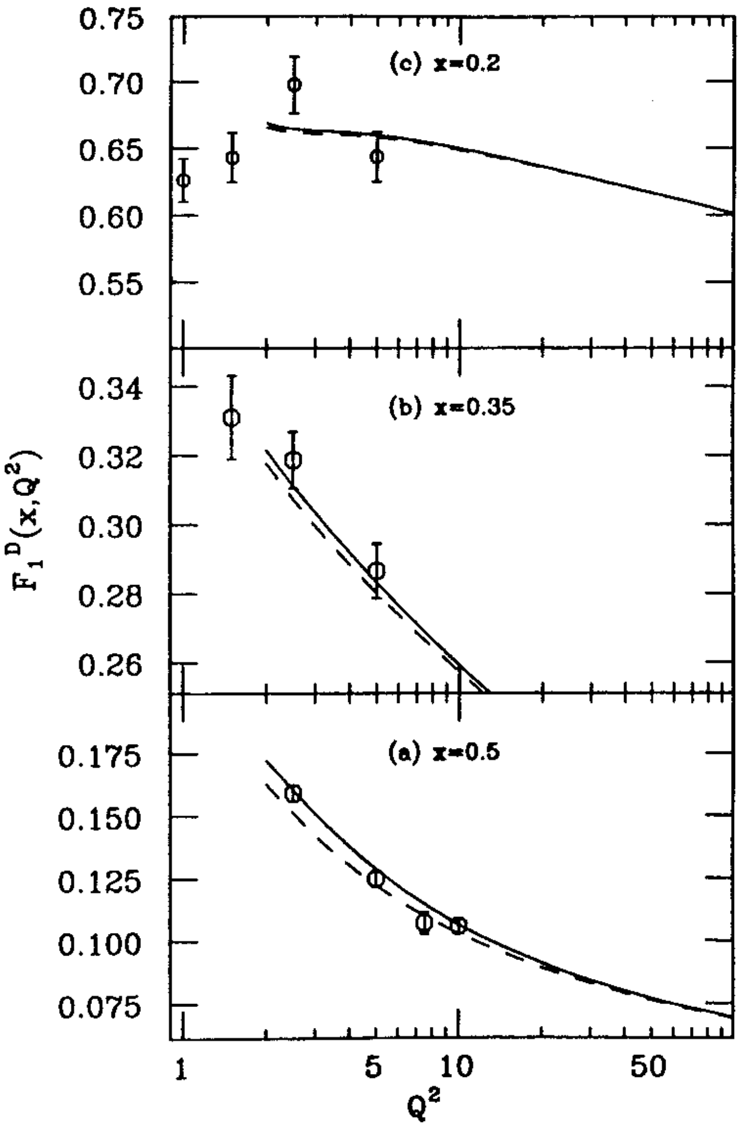

Figs. IV.5 The values of F_1^D extracted from our deuterium data at x values of 0.2, 0.35 and 0.5 are plotted versus Q^2. Only statistical and point-to-point systematic errors are shown - There is an additional normalization error of ≈ ±3.3% due to target length measurement, acceptance and radiative corrections. QCD evolution of the structure function F_1^{QCD} (dash curve), and the target mass effect corrected F_1^{QTM} (solid curve) are also plotted at each x. The effect of target mass is small for F_1.

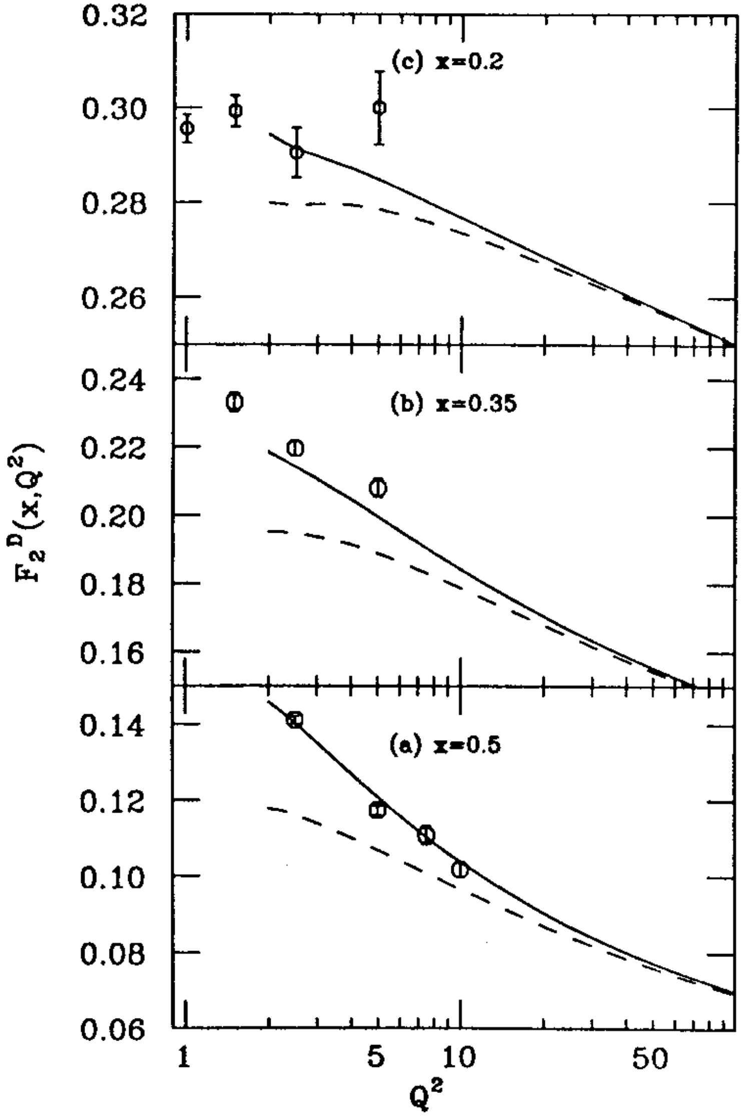

Figs. IV.6 The values of F_2^D extracted from our deuterium data at x values of 0.2, 0.35 and 0.5 are plotted versus Q^2. Only statistical and point-to-point systematic errors are shown - There is an additional normalization error of ≈ ±3.3% due to target length measurement, acceptance and radiative corrections. QCD calculation of the structure function F_2^{QCD} (dash curve), and the target mass effect corrected F_2^{QTM} (solid curve) are also plotted at each x.

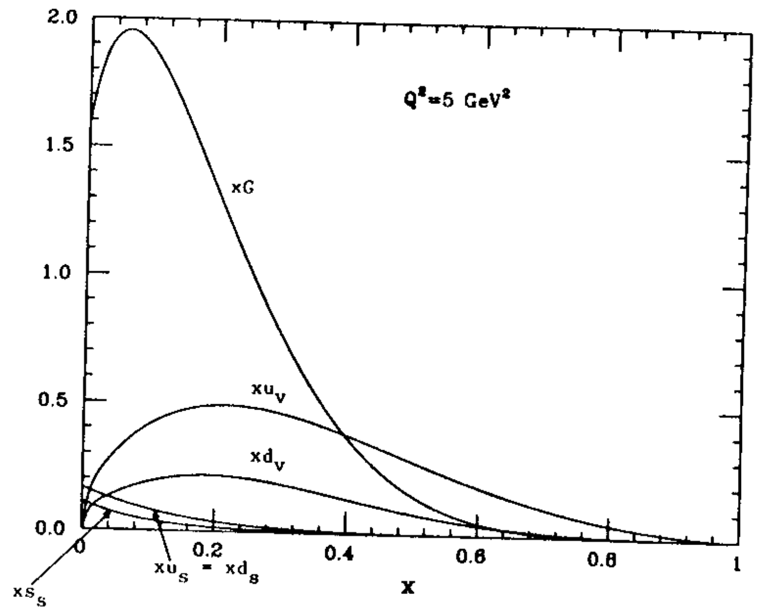

Fig. IV.7 Quark and gluon distributions from CDHS QCD evolution fits are plotted at Q^2=5 GeV^2.

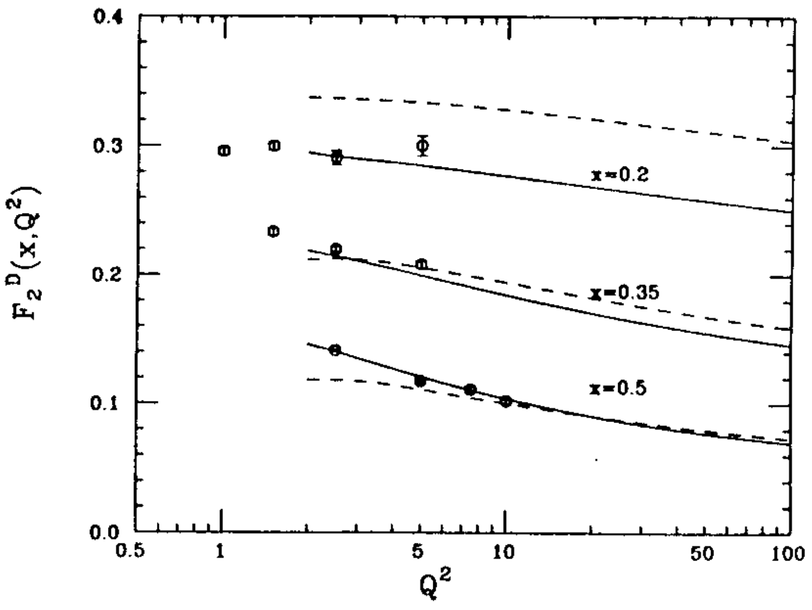

Fig. IV.8 F_2^{QTM} calculated using CDHS (solid curve), and Duke-Owens Set I (dash curve) are compared to our F_2^D data. DO results are in disagreement with our data at small x.

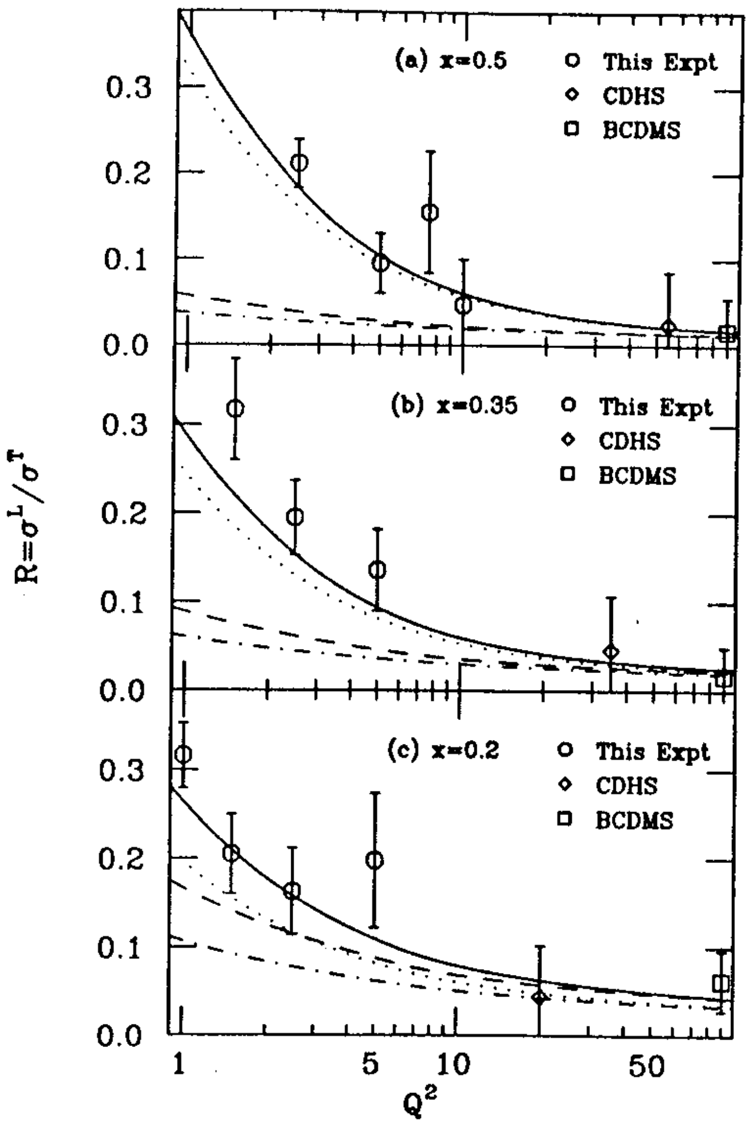

Figs. IV.9 R^{QCD} and R^{QTM} calculations using CDHS (solid and dash curves), and Duke-Owens Set I (dot and dot-dash curves) are compared to our R data. The DO results do not agree with CDHS results at low x because DO structure functions did not fit our data well.

TABLE IV.I

Values of R, F_1 and F_2 for each (x,Q^2) point and target (D_2 and Fe′ targets are of 2.6% radiation lengths each, whereas Au and Fe are of 6% rl) are tabulated. Statistical and all systematic errors are shown separately for R results. Statistical and point-to-point systematic errors are added in quadrature for F_1 and F_2.

TARGET	x	Q^2	$\Delta\epsilon$	$R=\sigma_L/\sigma_T$			F_1		F_2		χ^2/df
				value	±stat	±syst	value	± err	value	± err	
D_2	0.20	1.0	0.36	0.35	0.04	0.04	0.626	0.016	0.296	0.003	0.6
D_2	0.20	1.5	0.32	0.28	0.04	0.04	0.643	0.019	0.299	0.003	1.7
D_2	0.20	2.5	0.37	0.10	0.05	0.04	0.698	0.022	0.291	0.005	0.1
D_2	0.20	5.0	0.25	0.20	0.05	0.05	0.644	0.019	0.300	0.008	0.4
D_2	0.35	1.5	0.30	0.30	0.05	0.05	0.331	0.012	0.233	0.003	0.2
D_2	0.35	2.5	0.36	0.15	0.03	0.04	0.319	0.008	0.220	0.002	0.6
D_2	0.35	5.0	0.33	0.13	0.04	0.04	0.287	0.008	0.208	0.003	0.5
D_2	0.50	2.5	0.51	0.20	0.03	0.03	0.159	0.003	0.141	0.001	0.7
D_2	0.50	5.0	0.46	0.10	0.03	0.04	0.125	0.003	0.117	0.001	0.7
D_2	0.50	7.5	0.37	0.16	0.06	0.04	0.107	0.004	0.111	0.002	-
D_2	0.50	10.0	0.35	0.05	0.04	0.04	0.106	0.003	0.102	0.002	0.0
Fe′	0.20	1.0	0.36	0.32	0.04	0.04	0.638	0.018	0.296	0.003	0.2
Fe′	0.50	2.5	0.51	0.22	0.05	0.04	0.143	0.006	0.130	0.001	-
Fe	0.20	1.0	0.36	0.27	0.04	0.04	0.669	0.019	0.298	0.003	1.7
Fe	0.20	1.5	0.32	0.15	0.04	0.04	0.713	0.020	0.299	0.004	0.5
Fe	0.20	2.5	0.37	0.25	0.06	0.04	0.656	0.023	0.310	0.006	1.3
Fe	0.35	1.5	0.30	0.34	0.06	0.04	0.321	0.013	0.235	0.003	1.1
Fe	0.35	2.5	0.36	0.26	0.04	0.04	0.298	0.009	0.223	0.002	1.1
Fe	0.35	5.0	0.33	0.15	0.05	0.04	0.277	0.009	0.205	0.003	0.1
Fe	0.50	2.5	0.51	0.22	0.03	0.03	0.146	0.003	0.132	0.001	0.7
Fe	0.50	5.0	0.46	0.08	0.04	0.04	0.119	0.004	0.110	0.001	0.1
Au	0.20	1.0	0.36	0.32	0.04	0.04	0.647	0.019	0.300	0.003	0.3

REFERENCES

[IV.1] E. D. Bloom et al., Phys. Rev. Lett. **23**, 930 (1969);
M. Breidenbach et al., Phys. Rev. Lett. **23**, 935 (1969).
G. Miller et al., Phys. Rev. D **5**, 528 (1972)

[IV.2] A. Bodek et al., Phys. Rev. **D 20**, 1471 (1979).

[IV.3] M. D. Mesteyer et al., Phys. Rev. **D 27**, 285 (1983).

[IV.4] S. Ekelin and S. Fredriksson, Phys. Lett. **162 B**, 373 (1985).

[IV.5] G. Altarelli and G. Martinelli, Phys. Lett. **B 76**, 89 (1978).

[IV.6] H. Georgi and D. Politzer, Phys. Rev. **D14**, 1829 (1976);
A. De Rujula et al., Ann. Phys. **103**, 315 (1977);
R. Barbieri et al., Nucl. Phys. **B 117**, 50 (1976);
A. J. Buras et al., Nucl. Phys. **B 131**, 308 (1977);

[IV.7] K. Bitar et al., Phys. Lett. **83B**, 114 (1979);
P. Johnson and W. Tung, Neutrino '79 Proceedings, Bergen, Norway, (1979).

[IV.8] P. Buchholz, Report of CDHS collaboration in the Proceedings of the EPS International Conference on High Energy Physics, Bari, Italy, 1985.

[IV.9] A. C. Benvenuti et al. (BCDMS), Phys. Lett. **195 B**, 91 (1987).
A. Milsztajn, the proceedings of the International Europhysics Conference on High Energy Physics, Uppsala (1987).

[IV.10] R. P. Feynman, "Photon Hadron Interactions", (Benjamin, Menlo Park, California, 1972).

[IV.11] G. Altarelli and G. Parisi, Nucl. Phys. **B 126**, 298 (1977).

[IV.12] H. Abramowicz et al. (CDHS), Z. Phys. C 12, 289 (1982);
B. Vallage (CDHS), Ph. D. thesis, University de Paris-Sud, (July 1984).
D. W. Duke and J. F. Owens (DO), Phys. Rev. D 30, 49 (1984).

[IV.13] This factor of 1.12 brings the old CDHS structure functions into better agreement with the recent measurements of neutrino total cross sections. See P. Berge et al. (CDHS), Z. Phys. C 35, 443 (1987); and R. Blair et al. (CCFR), Phys. Rev. Lett. 51, 735 (1983).

[IV.14] M. Gluck et al., Z. Phys. C13, 119 (1982).

[IV.15] D. Gross et al., Phys. Rev. D15, 2486 (1977);
A. De Rujula et al., Phys. Rev. D15, 2495 (1977).

V. R^{Fe}-R^{D} ANALYSIS

A. Introduction

The discovery of the difference in the structure function $F_2(x)$ for iron and deuterium targets [V.1-4], known as the EMC effect, has sparked considerable activity in the theoretical study of deep inelastic lepton scattering from nuclear targets. The deuteron can essentially be viewed as composed of a free proton and a free neutron (with relative Fermi motion), whereas the nuclear binding effects appeared to be more important in heavy nuclei (Atomic mass, A>5). The effects due to the Fermi motion of bound nucleons in nuclei was expected to increase the ratio F_2^{Fe}/F_2^{D} at large x. The fall in this ratio at moderate x, the EMC effect, came as a surprise. There are numerous models [V.5] for the EMC effect which are built on a variety of ideas: Q^2-rescaling, x-rescaling (nuclear binding effects), convolution of structure functions of clusters of nuclear matter (pions in nuclei), and others. The predictions for σ^A/σ^D in all these models are in agreement with data for $x > 0.3$, but details of x dependence below $x=0.2$, and of Q^2 dependence are different. In addition some models [V.6], predict a large difference in the quantity $R=\sigma_L/\sigma_T$ for deuterium and iron ($R^{Fe}-R^{D} \approx 0.1$ to 0.15). Others [V.7], including those based on Quantum Chromodynamics (QCD), predict a negligible difference ($R^{Fe}-R^{D} \approx 0.002$). Some authors [V.8] have conjectured that higher twist effects might be different for different nuclei, and yield an atomic mass (A) dependence of R. The quantity R is a sensitive measure of point-like spin-0 constituents (e.g. tightly bound di-quarks) of the nucleus. Therefore, an A-dependence of R could alter our view of nuclear structure in terms of spin-1/2 quarks and vector gluons. An A-dependence of R ($R^{Fe}-R^{D} \approx 0.15$) was proposed [V.9], as a possible explanation for the initial experimental discrepancy at low x (see Figs. I.5 and I.7) between σ^A/σ^D as measured at CERN [V.1] and at SLAC [V.2,V.4]. There were hints in previous data [V.3] (SLAC-E139) that such a difference in R may have been observed.

B. Models of the EMC effect

The nucleon Fermi motion effects increase the ratio σ^A/σ^D for x larger than 0.4. The fall in this ratio at moderate x, beyond the systematic uncertainty of the experiments, was unexpected. The numerous theoretical models constructed to explain the EMC effect can be classified into two distinct groups a) convolution models and b) rescaling models.

Basic idea of most convolution models is to describe the structure function of a nucleus as an incoherent sum over contributions from clusters of nuclear matter. The structure function $F_2^A(x,Q^2)$ is given by a coherent sum of convolutions of the probabilities $f_c^A(y)$ (to find cluster c with momentum y in the nucleus) with the structure functions of the cluster $F_2^c(x/y)$:

$$F_2^A(x,Q^2) = \sum_c \int_x^A dy\, f_c^A(y)\, F_2^c(x/y).$$

Some examples of clusters considered are nuleons themselves with reduced mass due to binding effects or with an increased size due to different boundary conditions in the nuclear environment, extra pions which help bind the nucleus together, Δ-isobars, multi-quark clusters (6q, 9q or 12q bags) or the whole nucleus as one big bag with free quark and colour flow throughout the whole nuclear volume. The differences amongst various models are in assigning probabilities to various clusters and in the choice of the structure function F_2^c. The cluster models easily reproduce the fall in the ratio F_2^{Fe}/F_2^D at moderate x ($0.3<x<0.7$). Some of these models have used additional spin-0 contributions for nuclei as compared to nucleons to predict the small rise in the EMC ratio at small x ($x<0.3$). Due to the uncertainties in the description of the nuclear composition it is important that further studies of structure functions are made. As observed earlier the quantity R is a sensitive measure of the spin of the nuclear constituents. If the heavy nuclei have larger spin-0 cluster density compared to the free nucleons (in a deuteron), it will cause an effective increase in R for heavy nuclei, in addition to producing the rise in the ratio σ^A/σ^D at small x.

In the second class of approach, the EMC effect is explained by a change of either the Q^2-scale or the x-scale for the nuclear structure function compared to the free nucleon. In the 'Q^2-rescaling' models the EMC effect is related to a change of quark confinement volume in the nuclear environment. Naively, the argument is as follows: the strength of the strong force between quarks is not just determined by the resolution $1/\sqrt{Q^2}$ at which they are probed, but also by the size of the volume in which they are confined. The size of confinement is then varied depending on the atomic weight. In this approach both the structure functions F_1 and F_2 will be effected equally and therefore one does not expect much change in R. The 'x-rescaling' model is based on the observation that the depression of the nuclear structure function at medium x can be very well reproduced if for a nucleus the scaling variable x is replaced by a modified one $x^*=M/M_A^*$, where M_A^* is an effective mass of nucleon which is smaller than the free nucleon mass M due to binding effects. More sofisticated treatment effectively changes the Fermi motion corrections so that the the depression at medium x results. This approach again does not predict any difference in R for low and high mass nuclei.

There are others [V.6] who conjectured that the impulse approximation fails at SLAC values of energy transfer. They have calculated a kinematic modification to the impulse approximation. This model predicts that the energy transfer to the spectator nucleons in the deep inelastic scattering (a few MeV) is important. The effects due to inclusion of spectator contribution in the energy conservation equation implies large and different changes in the structure functions F_1 and F_2 as a function of A. This model produces a difference in R for heavy nuclei versus deuteron of the order 0.15 in the kinematic range of this experiment.

C. $R^{Fe}-R^D$ Results

The difference R^A-R^D was determined by making linear fits, weighted by the statistical and point-to-point (ϵ-uncorelated errors; discussed in Chapter III) systematic errors, to the ratio of cross sections,

$$\sigma^A/\sigma^D = \sigma_T^A/\sigma_T^D\ (1+\epsilon'(R^A-R^D)),$$

versus $\epsilon'=\epsilon/(1+\epsilon R^D)$. The R^A-R^D results are thus independent of absolute normalizations of target length, spectrometer acceptance, beam intensity and energy scale. They are also insensitive to changes in acceptance with ϵ, offsets in beam energy, spectrometer angle, survey errors, long term charge monitor drifts, and "internal" radiative corrections. The fits made at different (x,Q^2) points are shown in Figs. V.1a-k. The values of R^A-R^D for all (x,Q^2) points are shown in Table V.I. The average χ^2 per degree of freedom for the goodness of fit was 0.7 indicating that the estimate of systematic uncertainty is conservative. The results are also plotted against x for various Q^2 values in Fig. V.2. The average R^A-R^D is $0.001\pm0.018(\text{stat})\pm0.016(\text{syst})$, with χ^2/df for agreement with no difference equal to 1.3. The single measurement for Au (Table II) is consistent with Fe results. The agreement with the model in ref.6 is poor.

The R^A-R^D results are consistent with zero, in agreement with models predicting no A-dependence of R (e.g. QCD). We rule out models predicting a large difference $R^A - R^D$, and in particular the speculation that impulse approximation fails is not substantiated by our data. Our data indicate that possible contributions to R from nuclear higher twist effects and spin-0 constituents in nuclei are not different from those in nucleons. The σ^A/σ^D measurements can now be identified with the structure function ratios F_2^A/F_2^D and F_1^A/F_1^D (see equation IV.1) in the region $0.2 \leq x \leq 0.5$.

D. σ^{Fe}/σ^D Results

The results for the ratio σ^A/σ^D averaged over various ϵ points at each (x,Q^2) are also shown in Table V.I. The overall normalization error (Δ) in σ^A/σ^D of $\Delta=\pm1.1\%$ is dominated by the errors in target length measurement and radiative corrections. Our results for σ^{Fe}/σ^D averaged over Q^2 and ϵ are compared with data from SLAC-E139 (with our improved radiative corrections discussed in Appendix C; $\Delta=\pm1.3\%$) [V.3], SLAC-E87 ($\Delta=\pm1.1\%$) [V.2] and SLAC-E61 ($\Delta=\pm4.2\%$) [V.4] in Fig. V.3a. There is excellent agreement between all the SLAC data. In Fig. V.3b our data is compared with high Q^2 data from CERN muon experiments BCDMS ($\Delta=\pm1.5\%$) [V.10], and EMC (preliminary results; $\Delta=\pm0.8\%$) [V.11]. The lower Q^2 SLAC results are in reasonable agreement with these high Q^2 muon scattering results, although a small Q^2 dependence cannot be ruled out. All experiments show a small rise in σ^{Fe}/σ^D for $x < 0.3$, but not as large as origninal EMC data [V.1].

We conclude that the EMC effect is confirmed with very small errors and that all data are now in agreement. Because the ratio

F_1^A/F_1^D is equal to the ratio of quark distribution functions, the EMC effect is due to a non-trivial difference in the quark distributions (e.g. Q^2 rescaling) between heavy nuclei and the deuteron.[5] The models using only the nuclear binding effects do not predict a rise above unity for the EMC ratio, and are therefore not favored. However, this statement is not strong as only a limited amount of data with small errors exists at small x. A small Q^2-dependence in the EMC ratio, between SLAC and CERN energies cannot be ruled out.

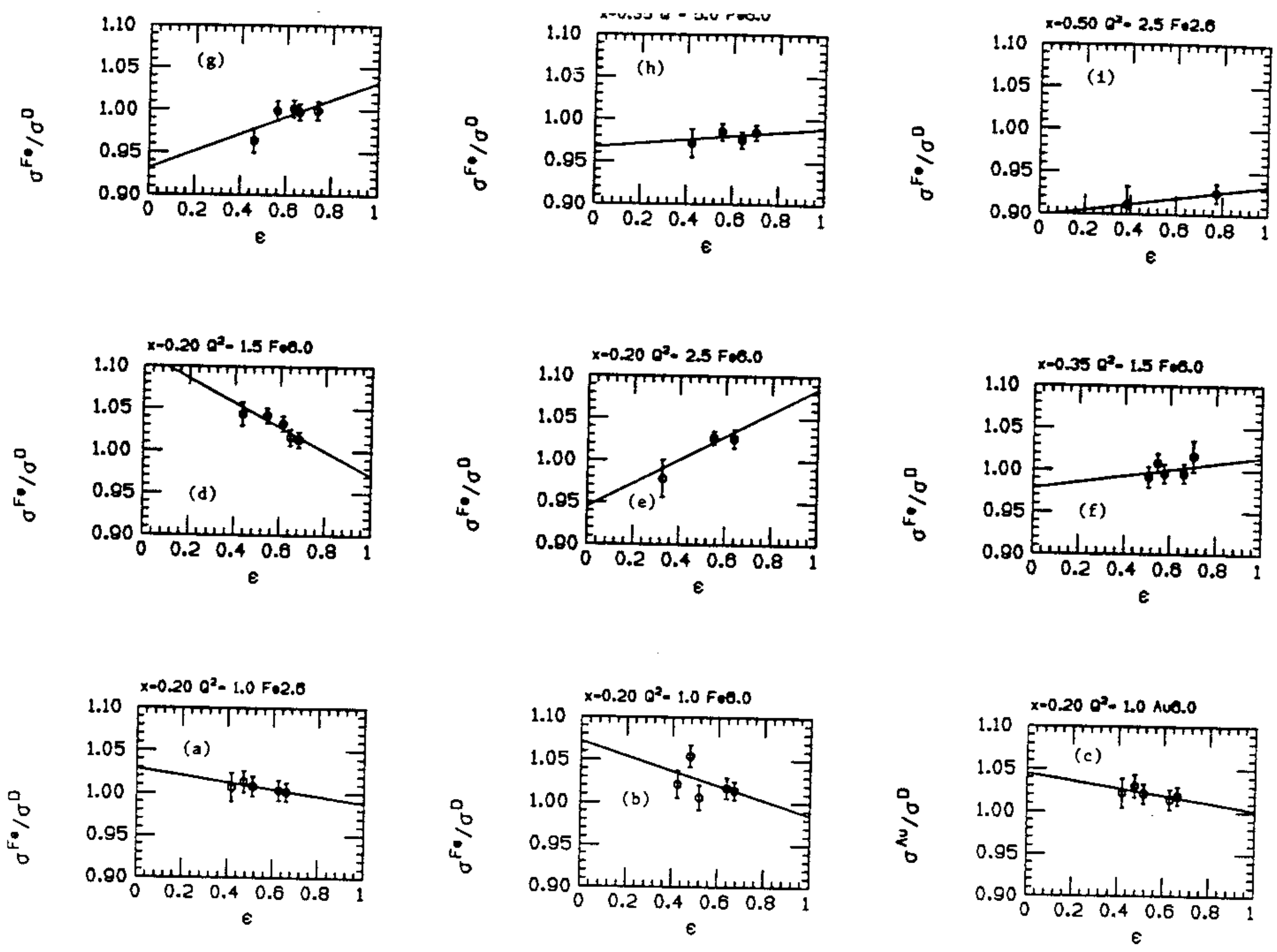

Figs. V.1 The fits to the differential cross section ratio σ^A/σ^D versus $\epsilon' = \epsilon/(1+R^D)$ are shown for each (x, Q^2) point separately for Fe (2.6% and 6% radiation length) and Au targets. The errors on the cross section include statistical and point-to-point systematic errors added in quadrature. It is to be noted that the errors radiative correction could cause an ϵ-dependent slope, which results in an overall systematic error in $R_A - R_D$ of ± 0.015.

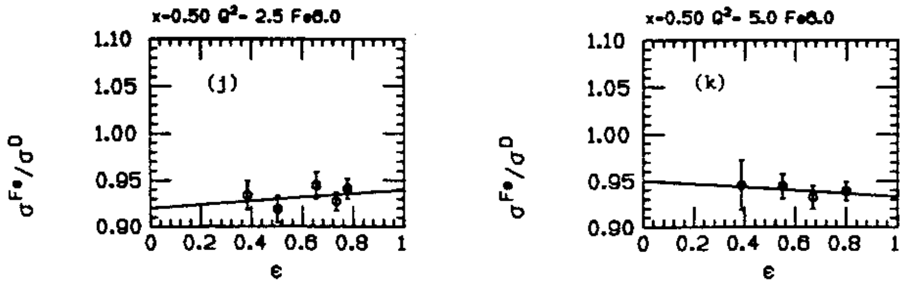

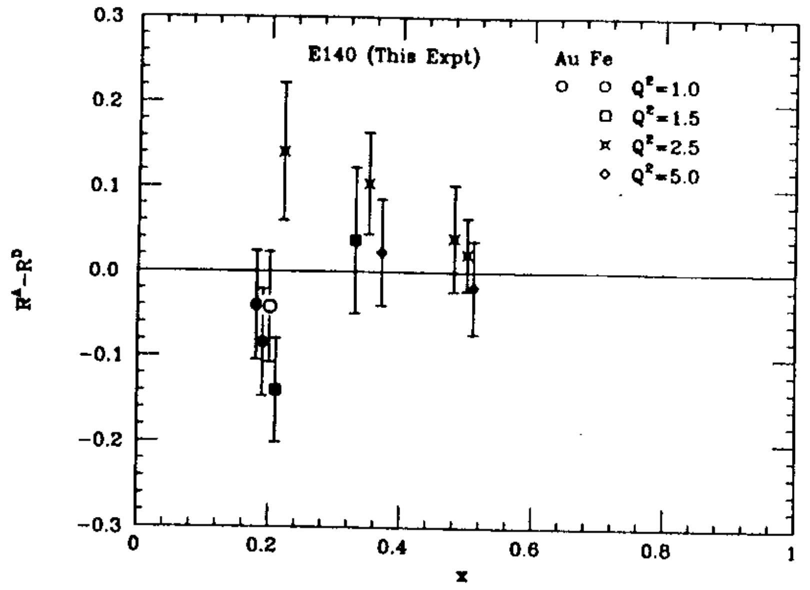

Fig. V.2 The results for R^A-R^D are plotted as a function of x; 2.6% and 6% Fe, and Au (open symbol) targets are plotted separately. Statistical and all systematic errors are added in quadrature.

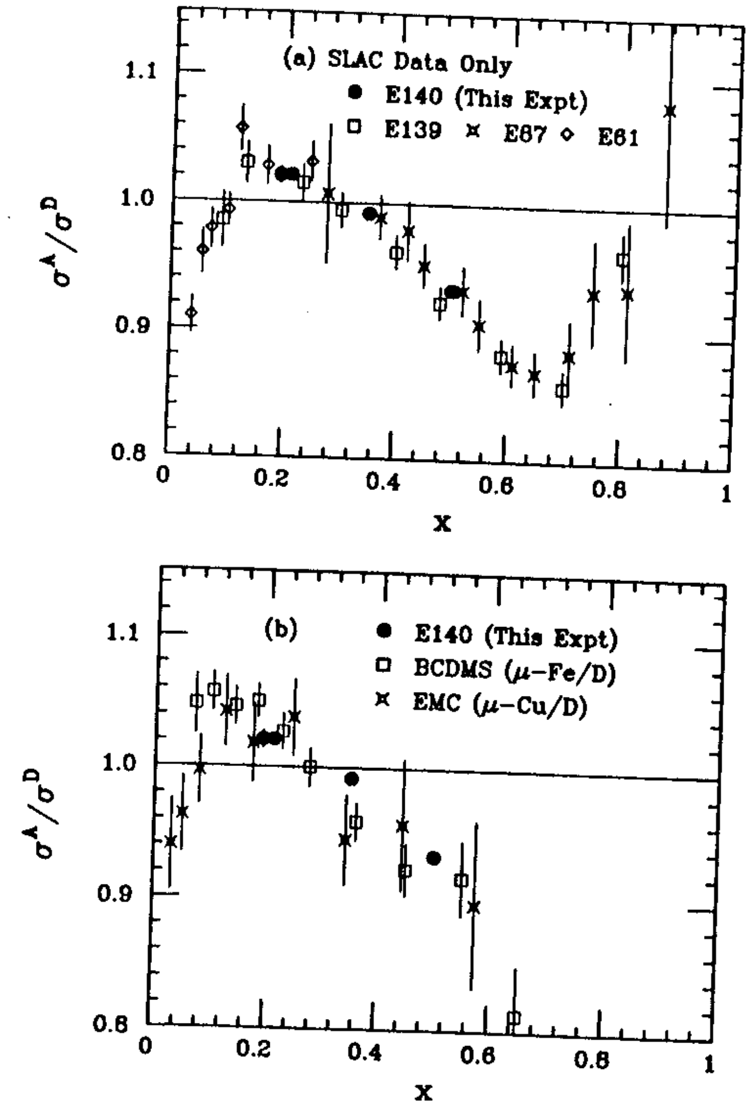

Figs. V.3 The results for σ^A/σ^D are plotted as a function of x and are compared to other (a) electron and (b) muon experiments. Our data from Fe and Au(x=0.2) targets are each averaged over ϵ and Q^2. Statistical and point-to-point systematic errors are added in quadrature for all experiments. The overall normalization errors (Δ) are discussed in the text.

TABLE V.I

Values of R^A-R^D, and σ^A/σ^D averaged over ϵ with statistical and point-to-point systematic errors. There is an additional error of ±0.015 in R^A-R^D due to radiative corrections and an overall normalization error (δ) in σ^A/σ^D of $\pm1.1\%$.

TARGET	r1	x	Q^2	$\Delta\epsilon'$	R^A-R^D value	R^A-R^D stat	R^A-R^D syst	σ^A/σ^D value	σ^A/σ^D stat	σ^A/σ^D syst
Fe	2.6	0.20	1.00	0.24	-0.040	0.059	0.021	1.006	0.005	0.004
Fe	6.0	0.20	1.00	0.24	-0.084	0.058	0.020	1.022	0.005	0.004
Au	6.0	0.20	1.00	0.24	-0.042	0.060	0.021	1.021	0.005	0.004
Fe	6.0	0.20	1.50	0.23	-0.140	0.057	0.018	1.028	0.004	0.002
Fe	6.0	0.20	2.50	0.33	0.141	0.075	0.025	1.023	0.006	0.002
Fe	6.0	0.35	1.50	0.20	0.037	0.080	0.027	1.000	0.005	0.002
Fe	6.0	0.35	2.50	0.28	0.104	0.055	0.019	0.995	0.005	0.002
Fe	6.0	0.35	5.00	0.28	0.023	0.059	0.016	0.981	0.005	0.002
Fe	2.6	0.50	2.50	0.37	0.040	0.059	0.016	0.923	0.009	0.005
Fe	6.0	0.50	2.50	0.37	0.021	0.038	0.014	0.933	0.005	0.002
Fe	6.0	0.50	5.00	0.39	-0.018	0.050	0.017	0.939	0.006	0.004

REFERENCES

[V.1] J. J. Aubert et al., Phys. Lett. B 123, 275 (1983); G. Bari et al., Phys. Lett. B 163, 282 (1985).

[V.2] A. Bodek et al., Phys. Rev. Lett. 50, 1431 (1983); 51, 534 (1983);

[V.3] R. G. Arnold et al., Phys. Rev. Lett. 52, 724 (1984); SLAC-PUB-3257 (1983); S. Rock, Proceedings of the 22nd International Conference on High Energy Physics (Leipzig, 1984).

[V.4] S. Stein et al., Phys. Rev. D 12, 1884 (1975).

[V.5] E. Berger and F. Coester, Ann. Rev. Nucl. Part. Sci. 37, 463 (1987).

[V.6] Bo-Qiang Ma and Ji Sun, Print-86-1217, Beijing University, China (1986).

[V.7] F. E. Close et al., Phys. Lett. B 129, 346 (1983) - QCD model;

R. D. Smith, Phys. Lett. B 182, 283 (1986) - convolution model.

[V.8] E. V. Shuryak, Nucl. Phys. A446, 259C (1985).

[V.9] I. A. Savin and G. I. Smirnov, Phys. Lett. B 145, 438 (1984).

[V.10] A. C. Benvenuti et al., Phys. Lett. B 189, 483 (1987).

[V.11] M. Dueren and T. Sloan, Proceedings of the International Europhysics Conference on High energy physics (Uppsala, 1987).

VI. CONCLUSIONS

We report on results for the following quantities: the ratio $R=\sigma_L/\sigma_T$ of longitudinal (σ_L) and transverse (σ_T) virtual photon absorption cross sections, the structure function F_2, the differences R^A-R^D and the cross section ratios σ^A/σ^D, measured in deep inelastic electron scattering from targets of deuterium, iron and gold.

The results for R obtained at x=0.2, 0.35 and 0.5 show a <u>clear falloff with Q^2</u>, in the range $1 \leq Q^2 \leq 10$ GeV^2, in contrast to previous results in this kinematic range, which were consistent with a constant value of R=0.2. The x and Q^2 dependence of the quantity R is inconsistent with the naive parton model, and with the perturbative Quantum Chromodynamics predictions. However, <u>when effects due to target mass, calculated by Georgi and Politzer (GP), are included with the QCD predictions the results are in good agreement</u>. The possible spin-0 diquark content of the nucleons, and any large effects of higher twist terms, beyond those from kinematic target mass effects, are therefore not required to explain our data.

The results for the structure function F_2 are also in agreement with the QCD evolution of the structure functions calculated from the high Q^2 measurements (in a ν-Fe scattering experiment by CDHS collaboration) of quark-gluon momentum distribution functions, <u>only when GP target mass effects are included</u>. The target mass effects in the scaling violations in F_2 are primarily due to the longitudinal component F_L.

The results on the differences R^A-R^D are consistent with zero, and are in agreement with the models for the EMC effect, including those based on Quantum Chromodynamics, which predict negligible difference. Models, for instance those assuming that the impulse approximation fails, which predict large differences in R^A-R^D are ruled out. These results also indicate that there are no significant spin-0 constituents or higher twist effects in nuclei as compared to free nucleons. The measurements of the ratio σ^A/σ^D can now be identified with the structure function ratios F_2^A/F_2^D and F_1^A/F_1^D unambiguously in our kinematic range ($0.2 \lesssim x \lesssim 0.5$ and $1 \lesssim Q^2 \lesssim 5$ GeV^2).

The EMC effect, i.e. the x dependence of the ratio F_2^A/F_2^D, is confirmed with very small errors and all data (electron and muon scattering) are now in agreement. This ratio is larger than unity at low x, and is therefore inconsistent with models using nuclear binding corrections alone to explain EMC effect. Our improvements in the radiative corrections calculation have increased (by ~ 1%) the old SLAC results (SLAC-E139) also to values larger than unity at small x. Because the ratio F_1^A/F_1^D is equal to the ratio of quark distribution functions, we conclude that the EMC effect is due to a non-trivial difference in the quark distribution functions between heavy nuclei and deuteron. That is, these results are in agreement with QCD based models, and some convolution models.

APPENDIX A ACCEPTANCE OF THE 8 GeV SPECTROMETER

Spectrometer Optics

The 8 GeV spectrometer optics were studied in 1967 [A.1] using low intensity electron beams, at 3, 6, 8 and 9 GeV momentum settings. The transport matrix coefficients measured in these studies describe the path of charged particles through the spectrometer magnet array. The first order transport matrix coefficients that translate the position (x_t, y_t, z_t), and the angles $(\theta_t = dx/dz, \phi_t = dy/dz)$ of the particle with momentum $p + \Delta p/p$ at the target, to the particle coordinates at the focal plane in the "hut" $(x_h, \theta_h \cdots)$ are given in ref. [A.1]. The results for our experiment were obtained using the average of the 6 and 8 GeV 1967 measurements (obtained after a reanalysis of 6 and 8 GeV data) of reverse transport matrix elements (Table A.I). These measurements are not good to 1%, and in particular a small momentum dependence of the optics coefficients was of concern in the context of R measurements. Momentum dependence of the spectrometer optics was therefore studied by a floating wire technique [A.2]. Precision measurements of the transport coefficients were made in the momentum range of 1 to 9 GeV. The product of the coefficients which determines the acceptance of the spectrometer (A)

$$A(p) = \frac{\langle \delta | y \rangle \langle \phi_t | \phi \rangle}{\langle \theta_t | \theta \rangle \langle x | x_t \rangle_n - \langle x_t | \theta \rangle \langle \theta_t | x \rangle_n}$$

where sub-script n stands for coefficients measured for a nominal momentum setting. The correction factors to the our data, which were analysed with optics measurement coefficients, is plotted versus momentum in the Fig. A.1. A correction factor to total acceptance A_{tot} (described below),

$$A_{tot}(p,\theta) = A_{tot}(6,\theta)\ \left[0.982 - 0.00035\ p\right],$$

was applied.

The precision floating wire measurements also yielded information about the absolute momentum setting of the spectrometer. A correction factor to the nominal momentum setting of the spectrometer was applied. The momentum of the electrons is estimated to be accurately known to 0.05% [A.2].

Target length dependence of Acceptance:

Acceptance of the spectrometer was studied for the long target as a function of angle using a Monte Carlo simulation of the spectrometer optics. The average of 6 and 8 GeV coefficients were used in this simulation. One million events generated with uniform illumination of the spectrometer front window were transported to the spectrometer hut, when the spectrometer angle was set at 0°,5°,10°,...50°. The total acceptance, defined as the ratio of events expected to events found, in the range $|\Delta p/p| \leq 3.5\%$, $|\Delta\theta| \leq 6$mr, and $|\phi| \leq 28$mr, was determined at each of these angles. A linear fit of the form,

$$A_{tot}(p,\theta) = A_{tot}(p,0)\left[1 - 2\times10^{-5}(L\sin\theta)^2\right],$$

where L is the length of the target in cms, fitted the data well (χ^2/df=1). This correction factor applied to the cross section was a maximum of 0.4% at the highest angle of 46°. The systematic error on the cross section due to this correction is estimated to be below 0.1% level at this highest angle.

Acceptance function $A(\delta,\Delta\theta,\phi)$

The acceptance of the spectrometer was needed as a function of $\delta=\Delta p/p$, $\Delta\theta$ and ϕ because the deep-inelastic cross section varied non-linearly over the spectrometer acceptance region by upto 5%. The acceptance function was determined using our deep-inelastic solid target data and a fit to the old SLAC data. Electron counts (n_r) for each of our runs (r) were accumulated in $\Delta p/p$,$\Delta\theta$ and ϕ bins of width 0.5%, 1mr and 10mr, in the ranges $|\delta|\le5\%$, $|\Delta\theta|\le8$mr and $|\phi|\le40$mr respectively. The acceptance was expected to be 100% for the fiducial region: $|\delta|\le1\%$, $|\Delta\theta|\le2$mr and $|\phi|\le10$mr (see Figs. A.2a-c). The fit to the old SLAC deep-inelastic data enabled an estimation of counts in outer bins $n_r^{exp}(\delta,\theta,\phi)$. The fit to the old SLAC data was for Born cross sections, therefore radiative effects and an estimate of charge symmetric backgrounds were added to determine the raw cross section variation within the acceptance. The acceptance function is given by:

$$A(\delta,\theta,\phi) = \frac{\Delta\Omega \sum_r n_r(\delta,\theta,\phi)}{\sum_r n_r^{exp}(\delta,\theta,\phi)}, \quad n_r^{exp}(\delta,\theta,\phi) = \langle n_r^{norm}\rangle \frac{\sigma_{fit}(\delta,\theta,\phi)}{\sigma_{fit}^c}$$

where $\Delta\Omega$ is the solid angle of the (δ,θ,ϕ) bin, $\langle n_r^{norm}\rangle$ is the average number of counts in the normalization region of acceptance, and σ_{fit}^c is the fit cross section at the nominal spectrometer setting. The total acceptance in the solid angle $\Delta\Omega$ is given by:

$$A_{tot}(6,0) = \frac{\Delta\Omega \sum_\delta \sum_\theta \sum_\phi \sum_r n_r(\delta,\theta,\phi)}{\sum_\delta \sum_\theta \sum_\phi \sum_r n_r^{exp}(\delta,\theta,\phi)}.$$

Figs. A.3a-f show the acceptance function as a function of δ, $\Delta\theta$ and ϕ for the "standard" acceptance region $|\delta|\le3.5\%$, $|\Delta\theta|\le6$mr and $|\phi|\le28$mr and a "narrow" acceptance region $|\delta|\le2.5\%$, $|\Delta\theta|\le4$mr and $|\phi|\le20$mr. Results obtained for cross sections and R, for both "standard" and "narrow" acceptance regions, were compared. The average cross section ratio $\sigma^{\text{"standard"}}/\sigma^{\text{"narrow"}}$ and the average difference $R^{\text{"standard"}}-R^{\text{"narrow"}}$ were 1.003 ± 0.001 and 0.000 ± 0.009 respectively.

The total acceptance calculated for liquid target data at various angles was used to check the target length dependence of the acceptance, and these results agreed with the Monte Carlo results described above.

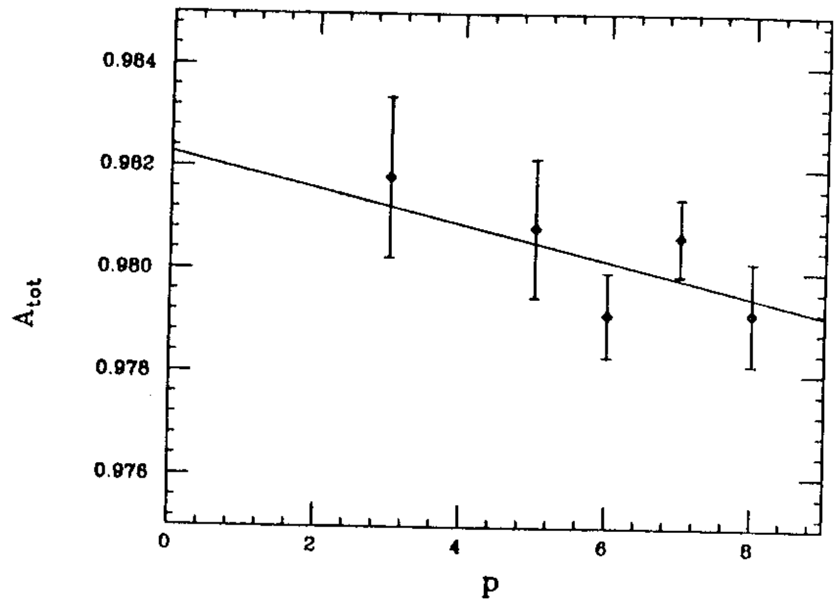

Fig. A.1 Correction to total acceptance measured in floating wire experiment is plotted versus momentum setting of the spectrometer. The data at p < 3 GeV is still under study.

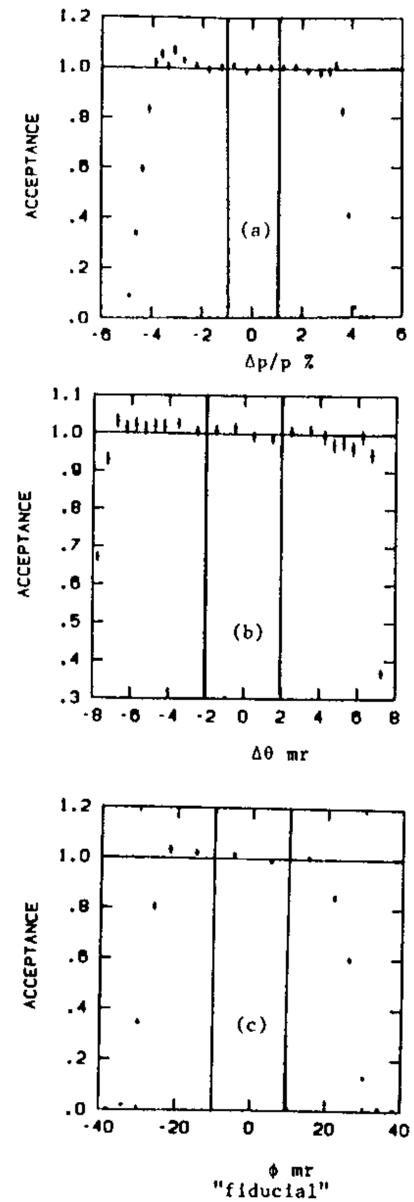

Figs. A.2 The acceptance function determined by using the solid target data is plotted for the fiducial region ($|\Delta p/p| \leq 1\%$, $|\Delta\theta| \leq 2$mr, and $|\phi| \leq 10$mr) versus (a) $\Delta p/p$, (b) $\Delta\theta$ and (c) ϕ. $\Delta p/p$ plot is cut on $\Delta\theta$ and ϕ and so on. The fiducial region cuts are shown on the figures. In the fiducial region the acceptance is 100%.

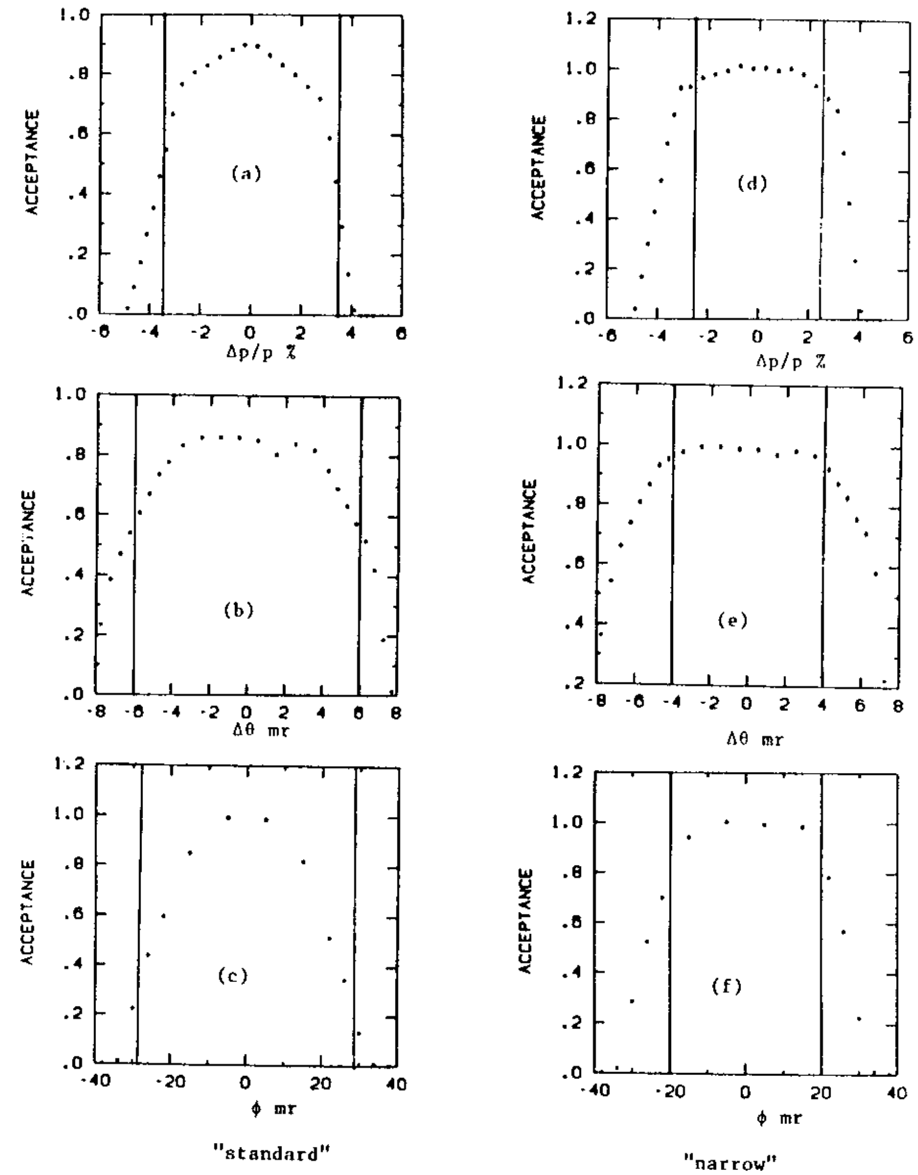

Figs. A.3 Acceptance function is plotted versus $\Delta p/p$, $\Delta\theta$ and ϕ, (a-c) for "standard" ($|\Delta p/p| \lesssim 3.5\%$, $|\Delta\theta| \lesssim 6$mr, and $|\phi| \lesssim 28$mr), and (d-f) "narrow" ($|\Delta p/p| \lesssim 2.5\%$, $|\Delta\theta| \lesssim 4$mr, and $|\phi| \lesssim 20$mr) regions. Each plot is cut on the other two kinematic quantities (cuts are shown on the figures).

TABLE A.I

Transport matrix elements used in computing kinematics of each event†.

	x_t	θ_t	ϕ_t	δ_t
x	4.55362	0.19387	-0.03694	-0.00205
θ	-4.29185	0.02408	0.03954	0.00245
y	-0.06007	0.00050	-0.02689	-0.34275
ϕ	-0.00142	-0.00419	-0.92820	0.00074
x^2	0.01756	0.00051	0.01063	-0.00013
$x\theta$	-0.03237	-0.00103	-0.01993	0.00012
xy	-0.00492	0.01485	0.00034	0.00059
$x\phi$	0.00133	-0.00098	0.00056	0.00005
θ^2	0.01543	0.00051	0.00930	0.00000
θy	0.00850	-0.01421	-0.00037	-0.00059
$\theta\phi$	-0.00106	0.00082	-0.00052	-0.00003
y^2	-0.00411	-0.00012	-0.00525	0.00020
$y\phi$	-0.00019	0.00003	-0.00083	0.00136
ϕ^2	-0.00005	0.00001	-0.00009	0.00004
offset	0.16211	0.00169	0.00171	0.00044

† $x_t = 4.55362x - 4.291858\theta \ldots\ldots -0.00005\phi^2 + 0.16211$ etc.

REFERENCES

[A.1] P. N. Kirk et al., Phys. Rev. D 8, 63 (1973).

[A.2] L. Clogher et al., SLAC-PUB (in preparation for submission to Nucl. Ins. Meth.); and L. W. Whitlow, Ph. D. thesis (in preparation), Stanford University.

APPENDIX B SHOWER ENERGY CALCULATION

The purpose of the Lead-glass shower counter used in this experiment (see Fig II.8) was to enable electron-pion separation. The electrons deposited all their energy in the shower counter, whereas the pions deposited only a fraction of their energy, and therefore the e/π separation was possible. In the shower energy computation for low energy particles ($1 \leq E' \leq 4$ GeV), only PR, TA and TB counters with total of 16.8 radiation lengths were used, whereas for higher-energy particles ($4 \leq E' \leq 8$ GeV) TC counters with 6.8 radiation lengths were used in addition. The energy deposited in the shower counter was determined in two ways (E_b^{sh} or E_t^{sh}). The first method did not use the particle track information from the wire chambers, and the energy was obtained by adding the energy deposited in each block in PR, TA and TB (and TC in case of higher-energy settings) rows:

$$E_b^{sh} = \sum_{i=1}^{6} P_i^{PR} B_i^{PR} + \sum_{i=1}^{6} P_i^{TAU} B_i^{TAU}$$

$$+ \sum_{i=1}^{6} P_i^{TAD} B_i^{TAD} + \sum_{i=1}^{6} P_i^{TB} B_i^{TB}$$

$$+ \text{(TC term for } E'>4)$$

where P_i are the pedestal subtracted ADC channels (corrected for hardware 50db attenuators put in for $E'>4$ GeV) and B_i are block calibration coefficients (in units of GeV/ADC channel). There are two drawbacks in this method: a) it is susceptible to background events as all the blocks in a row are used, and b) the resolution of the shower energy peak is not optimal as variations in pulse height with the position at which a particle enters the block is not accounted for. This calculation of shower energy was important in the study of the efficiency of the track reconstruction program. The second method used particle track reconstructed by the wire chambers to identify the hit lead glass blocks which were used in calculating the energy E_t^{sh}. The hit blocks were identified by two parameters i_{PR}=1,6 and i_T=1,3(or 4), where i_{PR} referred to the PR block hit and i_T referred to the track type. Due to segmented and staggered nature of the detector (see Fig. II.8), often particles passed through certain groups of blocks depending on the position on a PR block. The track type index enabled identifying TA and TB (and TC) blocks (see Table B.1) which had considerable energy deposition. The shower (track) energy is given by:

$$E_t^{sh} = \sum_r C(y)\, P(r,i_{PR},i_T)\, T(r,i_{PR},i_T),$$

$$r=PR,TA,TB \text{ (and TC for } E'>4 \text{ GeV)},$$

where $P(r,i_{PR},i_T)$ is the pedestal subtracted (and attenuator corrected) ADC channels for the hit blocks defined by i_{PR} and i_T in the r'th row, $T(r,i_{PR},i_T)$ is the corresponding calibration coefficient, and C(y) is the correction factor to account for attenuation of Cherenkov light in the lead glass as a function of y position on the block. The pulse height from the closest neighbour of

the hit block was also added. The calibration procedure is briefly discussed below.

The amount of Cherenkov light produced when a high-energy particle passes through matter, is directly proportional to the energy of the particle. The Cherenkov light produced in the lead-glass was collected by photo-multiplier tubes (PMT). The gains of the PMT's were adjusted (using the minimum ionizing cosmic ray muon energy deposition) such that signals from each of the tubes in a row (PR,TAU,...) were of the same magnitude when energy deposited in them was identical. However, the small differences in the PMT gains and electronic readout, and different attenuation factors for light traversal from the hit point on the block to the PMT etc. caused wide shower counter spectra (FWHM resolution = 25%/$\sqrt{E}$ GeV). The correction for y-dependence (y is the distance from the hit point on the block to the PMT) of the energy was obtained first for each block separately. Both the sets of calibration coefficients B_i^r and $T(r,i_{PR},i_T)$ were determined by minimizing the width of shower energy spectra for our inelastic data by a least squares method. In obtaining these coefficients data with different spectrometer momentum settings p were used, and therefore E_b^{sh}/p_{wc} and E_t^{sh}/p_{wc} (p_{wc} is the energy of the particle determined using the track coordinates from the wire chamber data) peaks were minimized. The final coefficients were obtained after some iterations. The track information was used in obtaining the block coefficients E_b^{sh} also to enable better calibration. The coefficients were determined for four different spectrometer energy ranges, 1-2, 2-4, 4-6 and 6-8 GeV. Fig. II.9 shows the shower energy spectrum for the worst case of π/e yields. The FWHM energy resolution attained was $18\%/\sqrt{E}$. This resolution is considerably worse than $12\%/\sqrt{E}$ expected for lead glass detectors. Poor resolution is expected due to the operating environment in the spectrometer hut which resulted in stray particles hitting PMT's directly, and due to the lead-glass blocks which were considerably old and had some radiation damage (these blocks were used in a previous experiment at the CERN ISR).

TABLE B.I

TA, TB and TC shower counter hit blocks corresponding to track type i_T and PR hit block i_{PR}

i_T	TA	TB	TC
1	i_{PR}	i_{PR}	i_{PR}
2	i_{PR}	i_{PR}	$i_{PR}+1$
3	$i_{PR}+1$	i_{PR}	$i_{PR}+1$
4	$i_{PR}+1$	$i_{PR}+1$	$i_{PR}+1$

APPENDIX C RADIATIVE CORRECTIONS

INTRODUCTION

Cross sections measured in deep inelastic scattering experiments have large contributions (upto 30% in our kinematic range) from processes other than the Born diagram shown in Fig I.1. However, the higher order contributions are dominated by modifications due to lepton-photon interactions and are calculable in the theory of Quantum Electrodynamics. The application of radiative corrections is essential to extract any information about the hadronic vertex, e.g. the structure functions. The cross section for lepton-nucleon inclusive reaction, i.e. where only the scattered electron is detected, to the order α^3 in fine structure constant can be symbolically expressed in terms of the Feynman diagrams as:

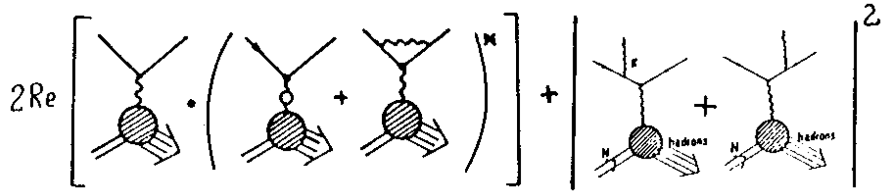

a b c d

The differential cross sections for these "internal" processes can be expressed in terms of the electromagnetic structure functions W_1 and W_2 [C.1]. The soft multiple photon emission process,

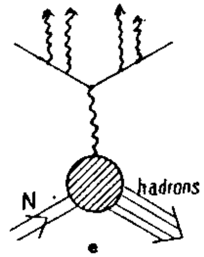

e

is important at low Q^2. The corrections due to γ-Z interference, and hadronic radiation are not discussed in detail here as they are small in our kinematic range. However, these effects are included in the procedure that was used.

For the case of electron scattering, low momentum transfer bremsstrahlung and ionization reactions in the process of electron traversal through the target material, called "external" effects, are also important.

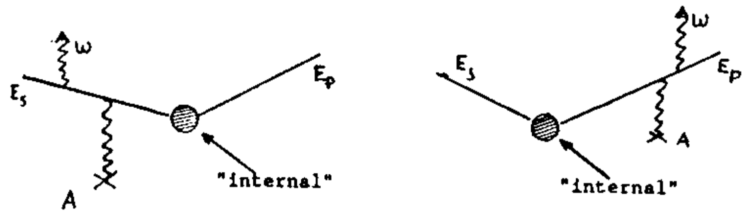

f g

The integral over the real photon four momentum (k) in the processes c and d can be reduced to integral over the photon energy ω and angle θ_k [C.2]. The well known infrared divergences in the diagrams c and d when $\omega \to 0$ are cancelled completely by the divergence in the diagram b. However, there are difficulties in numerically computing their cross sections when $\theta_k = \theta_s$ and $\theta_k = \theta_p$, where θ_s and θ_p

are angle of incident and scattered lepton, and when $\omega \to 0$. The integral over the photon energy ω requires the knowledge of the structure functions W_1 and W_2 in the deep-inelastic ($e\ N \longrightarrow e\ X$), quasi-elastic ($e\ p\ (A-1) \longrightarrow e\ p\ (A-1)$) and nuclear elastic ($e\ A \longrightarrow e\ A$) regimes and their contributions to differential cross sections are calculated separately. The ratios of radiative cross sections to Born cross section σ_{Born} are represented by δ_{inel}, δ_{qel}, and δ_{el} for these regions. Equation (I.1) gives the Born cross section in terms of W_1 and W_2. Different methods for the calculation of radiative cross sections used in this analysis are discussed below. The fit to deep inelastic structure functions W_2, measured at SLAC in earlier experiments [C.3], and the fits to elastic form factors [C.4] were used in the calculation of these cross sections. The quasi-elastic cross section was assumed to be a sharp peak centered at $W^2=M^2$ in some of the calculations, whereas in others a simple fit to the quasi-elastic peak was used.

Theoretical calculations

The lack of information about W_1 and W_2 which parameterize the hadronic vertex, in the early deep-inelastic experiments, and the limitation on numerical computing power, has caused difficulties in accurate evaluation of radiative corrections. Mo and Tsai, have therefore developed a simplified scheme which involved various peaking approximations in addition to equivalent radiator method to calculate both "internal" and "external" corrections simultaneously [C.2]. This approach, here after called "MT PEAK", was widely used in previous

experiments. The corrections calculated in this scheme were estimated to be accurate to few per cent, and were not tolerable for our experiment.

Mo and Tsai have also calculated the cross section for the "internal" bremsstrahlung diagrams c and d exactly [C.5]. This formula was used earlier to calculate quasi-elastic "internal" contribution for the SLAC experiments [C.6], and by the EMC group for the muon scattering radiative corrections [C.7]. However, the inelastic contribution in the EMC program was not calculated correctly. We have devised a scheme, called "MT EXACT", which includes some adhoc terms similar to those in "MT PEAK" method to cancel the infrared divergence in diagrams c and d, to calculate "internal" contribution completely.

We have also used a complete calculation of Mo and Tsai's formula for "external" contributions, without the energy peaking approximation. However, this approach, called "MT EQUI", continued to use the equivalent radiator approximation due to the limitation on computing power. This procedure was checked experimentally by using targets of different radiation lengths.

Bardin et al. [C.8], have calculated the diagrams a-d completely, and some additional ones to include γ-Z interference, 2-photon exchange and hadronic bremsstrahlung. The exact "BARDIN" calculations have the most sophisticated and complete treatment for the "internal" radiative corrections and were used in obtaining the results for this experiment. The purpose of "MT EXACT" was only to test the level of accuracy of "BARDIN" calculations.

Details of "MT PEAK" and "BARDIN" calculations are descibed in detail elsewhere [C.2, C.8]. Here, only the improvements made to Mo and Tsai's formalism are discussed. The notation followed in this chapter follows Tsai's publication SLAC-PUB-848 closely, and is not explained here in detail.

"INTERNAL" CORRECTIONS

Vacuum Polarization and Vertex correction

The contribution from the vacuum polarization diagram a for electron, muon and tau lepton loops can be written as [C.9]:

$\delta^{1}_{vac} = \frac{2\alpha}{\pi} f(x_1)$, where $x_1 = \frac{4m_1^2}{-Q^2}$, m_1 is the mass of lepton and

$$f(x_1) = -5/9 - x_1/3 + (1-x_1)^{1/2}(2+x_1)/6 \ \ln\left[((1-x_1)^{1/2}+1)/((1-x_1)^{1/2}-1)\right]$$

Mo and Tsai in their original work have used only electron loops for the vacuum polarization diagram. We have added muon, tau and quark loops, which together contribute as much as the electron loop even at SLAC values of Q^2. The quark loops in the vacuum polarization diagram could also be calculated using similar formula if the quark masses were known, but we have used a parameterization of hadronic vacuum polarization δ^{h}_{vac} from TASSO collaboration as used by Bardin et al. [C.10]. These contributions $\delta_{vac} = \delta^{1}_{vac} + \delta^{h}_{vac}$ are identical for all Mo and Tsai, and Bardin et al. programs.

The non-divergent contribution from the vertex correction diagram b is given by [C.11]:

$$\delta_{vert}(Q^2) = \frac{2\alpha}{\pi}\left[-1+0.75 \ln(Q^2/m^2)\right]$$

The noninfrared divergent part of the soft photon emission cross section yields [C.11]:

$$\delta_{nis}(Q^2) = \frac{\alpha}{\pi}\left[\frac{\pi^2}{6} - \Phi\left(\cos^2\frac{\theta}{2}\right)\right]$$

All the above corrections are included in the factor $F(Q^2)$,

$$F(Q^2) = \left(1 + \delta_{vac} + \delta_{vert} + \delta_{nis}\right)$$

and are applied to structure functions W_1 and W_2, or to Born cross section σ_{Born} to form effective structure functions and cross section.

Exact Mo and Tsai calculation

The contribution to radiative cross section from the internal bremsstrahlung diagrams c and d can be written suggestively as (equation A.24 of Y. S. Tsai, SLAC-PUB-848, gives the complete formula for the integrand):

$$\sigma_b = \int_1^1 d\cos\theta_k \int_0^{\omega m} d\omega \ (A + B\omega + C/\omega),$$

where A, B and C are weakly varying functions of ω. The third term in the integrand is infrared divergent. However, this divergence is unphysical and is known to be cancelled to this order by the divergent part of the vacuum polarization diagram b [C.12]. Tsai has instead chosen to include the multiple soft photon term δ_{soft}:

$$\delta_{soft}(Q^2) = \left(\frac{\omega}{E_s}\right)^{t_r} \left(\frac{\omega}{E_p+\omega}\right)^{t_r}, \text{ where } t_r = \frac{\alpha}{\pi}\left[\ln(Q^2/m^2)-1\right],$$

in the expression for σ_b to cancel the infrared divergence term, i.e.,

$$\sigma_b = \int_{-1}^{1} d\cos\theta_k \int_0^{\omega_m} d\omega\ (A + B\omega + C/\omega)\ \delta_{soft}$$

The integral is then finite but the integrand rises sharply as ω approaches 0. To enable accurate numerical computation of the integrals in this method it is necessary to separate soft and hard photons by a cutoff parameter Δ. The value of Δ is chosen such that the structure function variation below the cutoff is negligible, and is large enough so that the numerical integration above the cutoff is reliable, i.e. for $\omega < \Delta$ the contribution from the terms A and $B\omega$ are negligible, and the ω-dependence of C can be neglected. The analytic formula below the cutoff is given by:

$$\int_0^{\Delta} d\omega\ \frac{C}{\omega} \left(\frac{\omega}{E_s}\right)^{t_r} \left(\frac{\omega}{E_p+\omega}\right)^{t_r} \approx C \left(\frac{\Delta}{E_s}\right)^{t_r} \left(\frac{\Delta}{E_p+\Delta}\right)^{t_r}$$

It is to be noted that below the cutoff Δ, the angle integral still remains. It was <u>crucial</u> to perform the angle integration numerically to get reasonable results in this method. The structure functions W_1 and W_2 in the expressions for A, B and C were replaced by $F(Q^2)W_1$ and $F(Q^2)W_2$ to include the factorized contributions from vacuum polarization and vertex corrections. The continuum radiative cross section thus computed is semi-exact as the infrared divergent term was not cancelled correctly by the divergent part in the vertex diagram calculation. The dependence of cross section on the cutoff parameter

Δ was studied, and the best value of Δ=10 MeV was used in our calculations. For the quasi-elastic and elastic radiative tail contributions, the photon energy integral was evaluated analytically assuming that cross section is sharply peaked, and then the θ_k integral was evaluated numerically.

Bardin et al. calculation

Bardin et al. formulas for internal corrections are given in the references [C.8]. "BARDIN" method involved the most complete calculation of radiative cross section, including the infrared divergent terms of diagram b. The "internal" correction in "BARDIN" program is split into following terms,

$$\delta^B = \frac{\sigma^i(\text{"BARDIN"})}{\sigma_{Born}} = \delta_s^B + \delta_h^B + \delta_v^B + \delta_t^B + \delta_q^B + \delta_4^B + \delta_Z^B$$

The "inelastic continuum" contribution from diagrams b and c is given by the sum $\delta_s^B+\delta_h^B$, in which the infrared divergence is cancelled without the use of soft photon cutoff parameter Δ. The soft photon part of the inelastic correction δ_s^B was exponentiated in early versions of the programs using the "variant 1" from the reference C.13. But for the results presented here exponentiation procedure for soft photon term was <u>NOT</u> used. The vacuum polarization contribution δ_{vac} was computed as described above for "MT EXACT" scheme, and was then "exponentiated" as $\delta_v^B=[2/(1-\delta_{vac}/2)-2]$ to include higher order corrections. The term δ_t^B corresponds to the bremsstrahlung correction from the elastic and quasi-elastic tails. This term was corrected for the effect of smeared quasi-elastic cross section using the calculations from "MT EQUI" method. The hadronic part of the correction δ_q^B calculated within the quark-parton model, the higher order electromagnetic corrections δ_4^B, and the weak interaction effect δ_Z^B are described briefly in reference [C.8] (c). The contributions δ_q^B, δ_4^B and δ_Z^B are all typically less than 1% each, in our kinematic range. The theoretical uncertainties at this stage are from the adhoc inclusion/neglect of higher order corrections by the various "exponentiation" procedures. Bardin et al. have supplied FORTRAN code to calculate the radiative corrections based on their theoretical work. The code was checked carefully by our group. Since "BARDIN" calculations are based on better theoretical ground, and since they have become world standard, we have used them exclusively for our "internal" calculations.

"EXTERNAL" CORRECTIONS

The measured cross section in deep-inelastic scattering experiment including the straggling of electrons in the target material (with atomic mass A, atomic number Z, and unit radiation lengths x_0 gm/cm^2, and thickness T in units of x_0) is given by [C.15],

$$\sigma_{exp}(E_s,E_p) = \int_0^T \frac{dt}{T} \int_{E_{s\,min}}^{E_s} dE_s' \int_{E_p}^{E_{p\,max}} dE_p' \; I(E_s,E_s',t)$$

$$\sigma_i(E_s',E_p')\; I(E_p',E_p,T-t) \qquad \text{(C.1)}$$

where $\sigma^i(E_s',E_p')$ is "internal" radiative cross section. The limits of

integration (see Fig. C.1) are

$$E_{p\,max} = \frac{E_s'}{1+E_s'(AM)^{-1}(1-\cos\theta)} \quad \text{and} \quad E_{s\,min} = \frac{E_p}{1-E_p(AM)^{-1}(1-\cos\theta)}.$$

The electron incident and final energies in this section are corrected for most probable energy losses Δ_s and Δ_p after passing through a target material of thickness T/2 (in units of x_0), i.e.

E_s denotes $E_s-\Delta_s$, and E_p denotes $E_p+\Delta_p$,

where $$\Delta_{s,p} = \frac{\xi}{2}\left[\ln\frac{3\times10^9\,\xi\,E_{s,p}^2}{2m^2Z^2} - 0.5772\right] \text{ and } \xi = 1.54\times10^{-4}\,\frac{ZTx_0}{A}$$

$I(E,\epsilon,t)$ denotes the probability for an electron of energy E to lose an energy ϵ while traversing material of radiation lengths t due to bremsstrahlung (W_b) and ionization (W_i) losses, and is given by,

$$I(E,E-\epsilon,t) = \frac{bt}{\Gamma(1+bt)}\left(\frac{\epsilon}{E}\right)^{bt}\left[\,W_b + W_i\,\right],$$

where $$W_b = bt\,\frac{\phi(\epsilon/E)}{\epsilon},\quad W_i = \frac{\xi}{\epsilon^2}\left(1+\frac{\epsilon^2}{E(E-\epsilon)^2}\right)^2,$$

$$\phi(v)\approx 1-v+0.75v^2,\quad b = \frac{4}{3}\left\{1+\frac{1}{12}\left[(Z+1)/(Z+\eta)\right]\left[\ln(184.15\,Z^{-1/3})\right]^{-1}\right\},$$

$$\eta = \ln(1194\,Z^{-2/3})/\ln(184.15\,Z^{-1/3}),$$

and Z is atomic number of material.

The angle peaking approximation was used in deriving these equations, i.e. the change in the angle of the electron after bremsstrahlung was neglected in the above expressions. The complete calculation of "internal" radiative cross section already involved a double integral, and therefore the full evaluation of measured cross section σ_{exp} with three additional integrations is impractical. In the evaluation of this integral alone, an equivalent radiator method was used to estimate σ^{i}. The inelastic continuum contribution to the measured cross section was also calculated using a parameterization of σ_i calculated in a peaking approximation "BARDIN" method. These results agreed to better than 0.5% with the equivalent radiator method, which was used to obtain results presented in this thesis

Mo and Tsai equivalent radiator method

Equivalent radiator method, used for "external" corrections only, involves using the shape of "external" bremsstrahlung (diagrams f and g) in calculating the cross section for "internal" bremsstrahlung (diagrams d and e). This method asserts that the effect of "internal" bremsstrahlung can be calculated by using two hypothetical radiators each of thickness $t_r = b^{-1}(\alpha/\pi)\left[\ln(Q^2/m^2)-1\right]$ radiation lengths, one placed before and one after the scattering point. That is in the equation (C.1), (a) the "internal" radiative cross section was replaced by:

$$\sigma_i(E_s',E_p') \approx F(Q^2)\,\sigma_{Born}(E_s',E_p'), \qquad Q^2=4E_s'E_p'\sin^2(\theta/2),$$

and, (b) target radiation lenghts t in the expression for W_b was replaced by $t+t_r$.

Our method involved evaluating the triple integral in equation (C.1) with the above replacements numerically. Analytic integration

was performed in the edges of kinematic region, i.e. regions A, B and C in Fig C.1. The "internal" contribution in this method was evaluated by setting T=0 and dropping the radiation length integral. For the quasi-elastic region Q, calculations were done with and without a smearing correction to the input cross section (in the y-scaling formalism). The effect of smearing correction was applied to the exact "BARDIN" calculations to obtain final results.

The original method of Mo and Tsai involved further approximations of the equation (C.1), which reduced the surface integral over the "triangle" to line integrals along E_s' and E_p' axes. This approximation called the energy-peaking approximation was essential to enable calculation of radiative corrections when the fits to Born cross sections was not available. The data was then taken in a mesh of points along E_s and E_p axes, at fixed angles. In the recent SLAC experiments, these approximate calculations were used although a global fit to old SLAC data was available.

COMPARISION OF VARIOUS METHODS

The radiative corrections were calculated for all of our kinematic points using the four procedures described above. A comparision of these calculations enabled an estimation of the systematic error on our results.

"Internal" corrections

"MT EXACT" calculations of δ_{inel} and $\delta_{qel}+\delta_{el}$ are compared to

"BARDIN" results in Figs. C.2a-c and C.3a-c respectively. "BARDIN" results in these comparison alone did not include γ-Z interference and hadronic terms, as they were not calculated in "MT EXACT" program. The results for δ_{int} agreed to better than 1% at all of our kinematic points. A systematic error of 1% was assigned to account for the ϵ-dependent uncertainties in the "internal" corrections. Additional support for the accuracy of these calculations comes from the exclusive muon scattering experiment, where the bremsstrahlung photons were detected [C.16].

The differences between "MT PEAK" and "BARDIN" internal contributions, were large and highly ϵ-dependent as shown in Figs. C.4a-c. The peaking approximations are indeed expected to fail at small ϵ and x values, where hard photon emission becomes significant. The "MT EQUI" method corrects for the neglect of the triangular region D in Fig. C.1, but the failure of angle peaking approximation is not accounted for (see Figs. C.5a-c for differences between the results from "MT EQUI" and "BARDIN" methods). These values of δ_{int} were upto 4% off from the exact calculations. However, the effect of the ratio $\sigma_{exp}/\sigma_{int}$ calculated for targets of different radiation lengths enabled testing the "external" effects directly.

"External" corrections

To test the validity of the "external" corrections, cross section data for Fe targets of 2.6% and 6% radiation lengths were used. The cross section ratio $\sigma^{Fe6}/\sigma^{Fe2.6}$ averaged over all kinematic points was consistent with unity (ratio=1.017 ± 0.005 (stat) ± 0.015 (syst)) (see

Figs. C.6a,b). The average difference $R^{Fe6}-R^{Fe2.6}$ was -0.04 ± 0.04 ± 0.02. Additional tests of the calculations were done using data from an earlier SLAC experiment E139 which measured cross sections from targets of 2%, 6% and 12% radiation lengths. The 12% data did not agree with the 2% data at small x when "MT PEAK" radiative corrections were applied [C.17]. These data were radiatively corrected using "MT EQUI" method, and better agreement was found at all x within errors as shown Figs. C.7a-c.

We have assigned a systematic error on the ratio σ^{Fe}/σ^{D} of 0.5%, to account for the difference in the radiation lengths of Fe and D targets. The estimate of error on $R^{Fe}-R^{D}$ due to "external" corrections is 0.015 assuming that all the error on the ratio could be ϵ-dependent.

Total radiative correction

The total radiative correction applied to the experimental cross sections was given by:

$$\delta = \frac{\sigma^{i+e}(\text{"MT EQUI"})}{\sigma^{i}(\text{"MT EQUI"})}\,\frac{\sigma^{i}(\text{"BARDIN"})}{\sigma_{Born}} .$$

Table C.I lists individual contributions to the "Total" radiative correction δ. The error on cross sections due to these corrections is estimated at 1% for ϵ-dependence, and an additional ±1% for any normalization errors. The error on R comes from the ϵ-dependence of the error on radiative corrections, and is estimated at ±0.03.

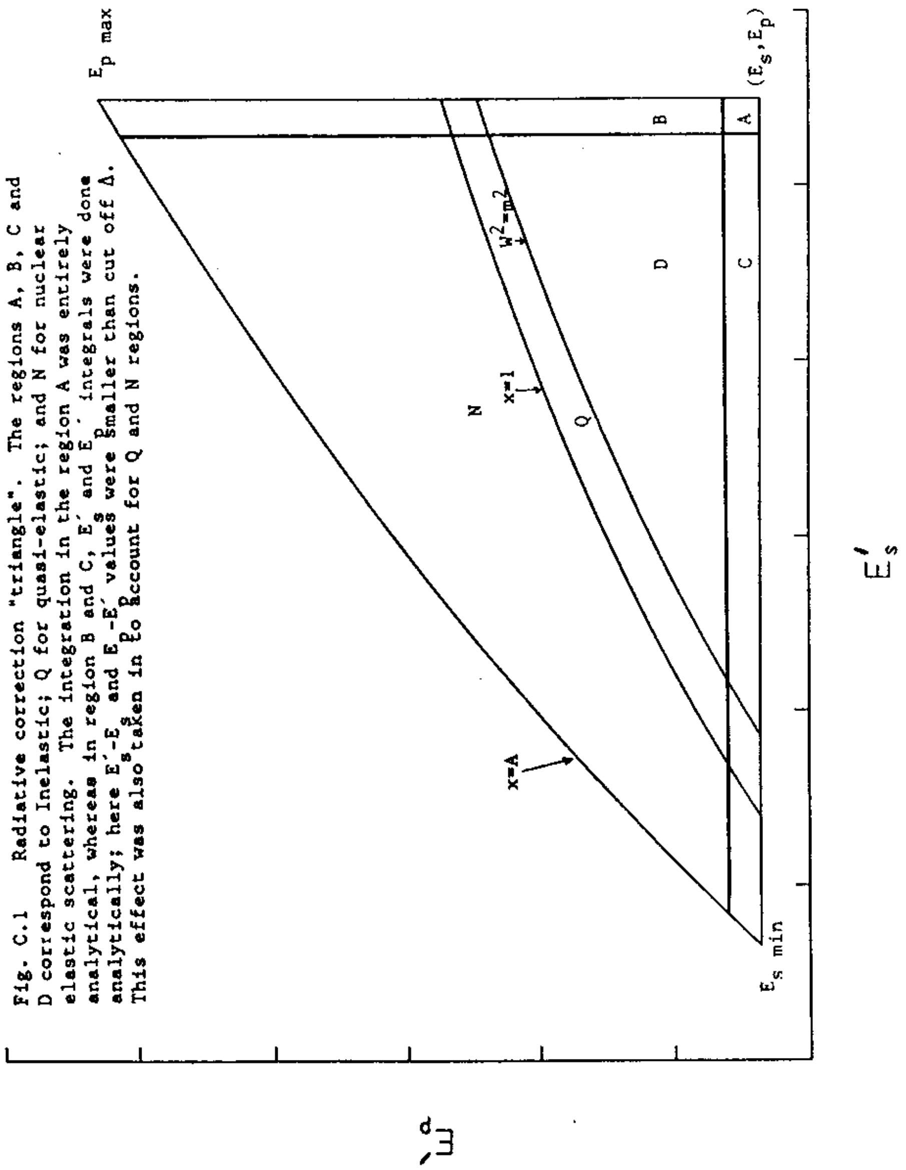

Fig. C.1 Radiative correction "triangle". The regions A, B, C and D correspond to Inelastic; Q for quasi-elastic; and N for nuclear elastic scattering. The integration in the region A was entirely analytical, whereas in region B and C, E'_s and E'_p integrals were done analytically; here E'_s-E_s and $E_p-E'_p$ values were smaller than cut off Δ. This effect was also taken in to account for Q and N regions.

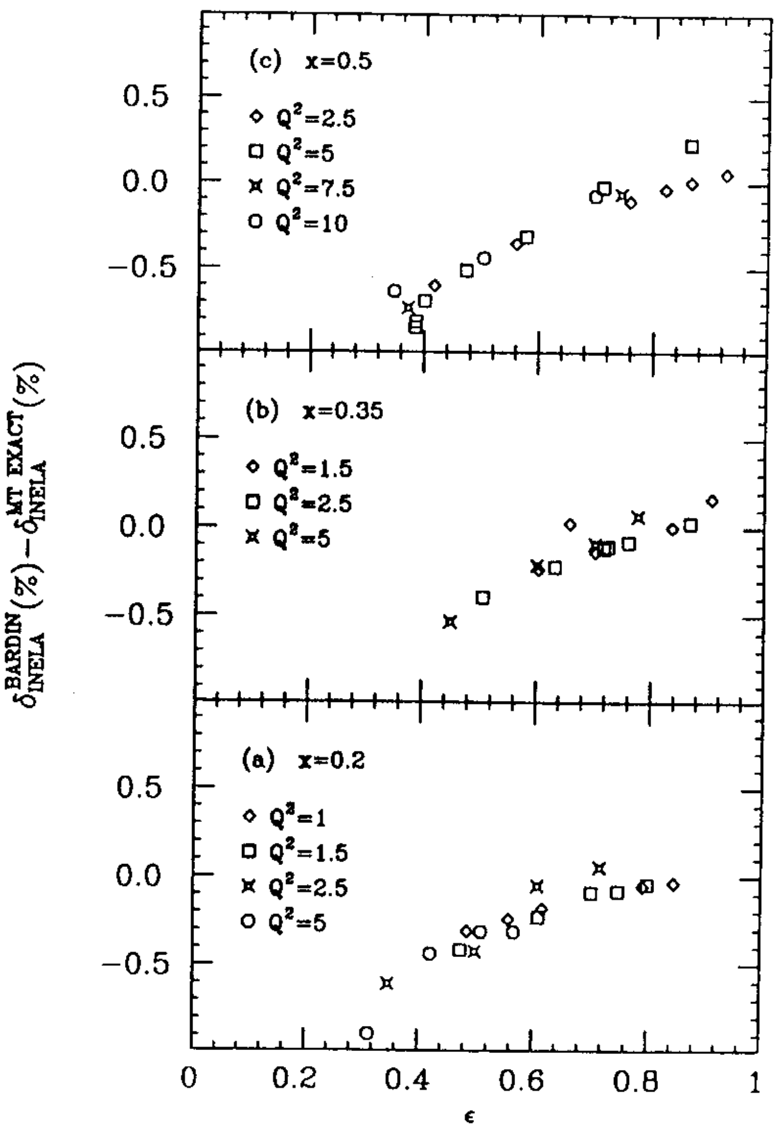

Figs. C.2 "Bardin" and "MT EXACT" inelastic "internal" δ's are compared. Difference in δ's (both in %) are plotted versus ϵ for all x,Q^2 points of our data set. The agreement is better than 0.8%.

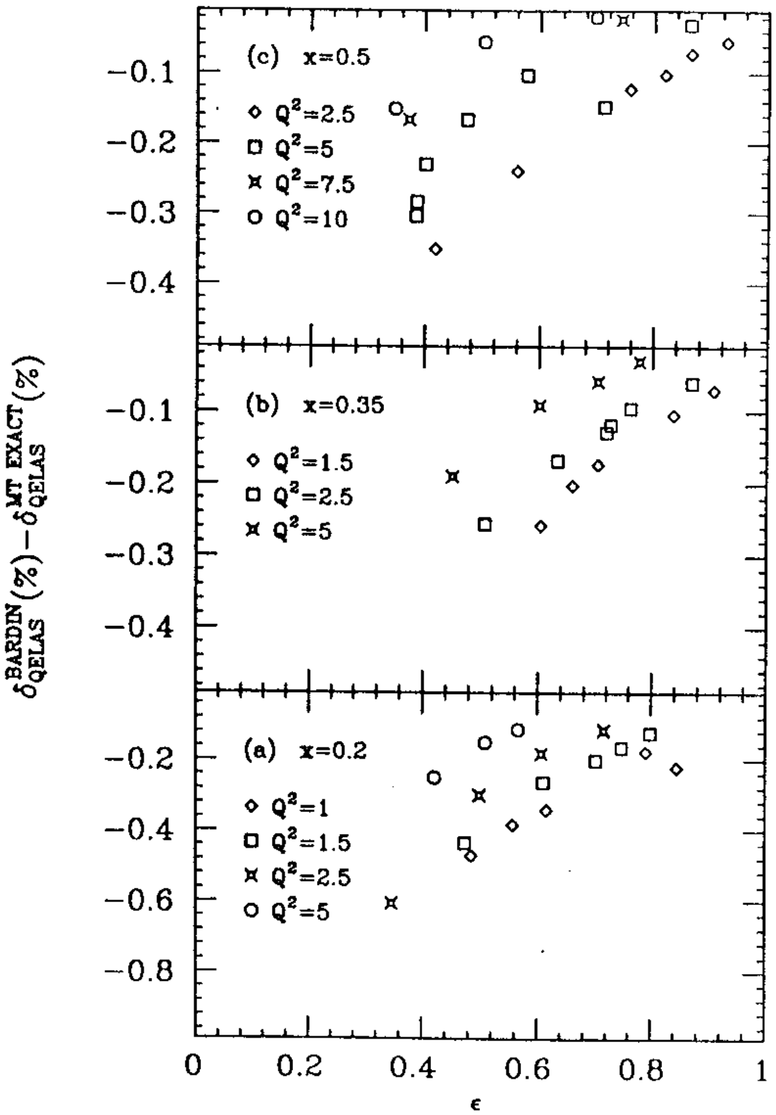

Figs. C.3 "Bardin" and "MT EXACT" quasi-elastic "internal" δ's are compared. Difference in δ's (both in %) are plotted versus ϵ for all x,Q^2 points of our data set. The agreement is better than 0.6%.

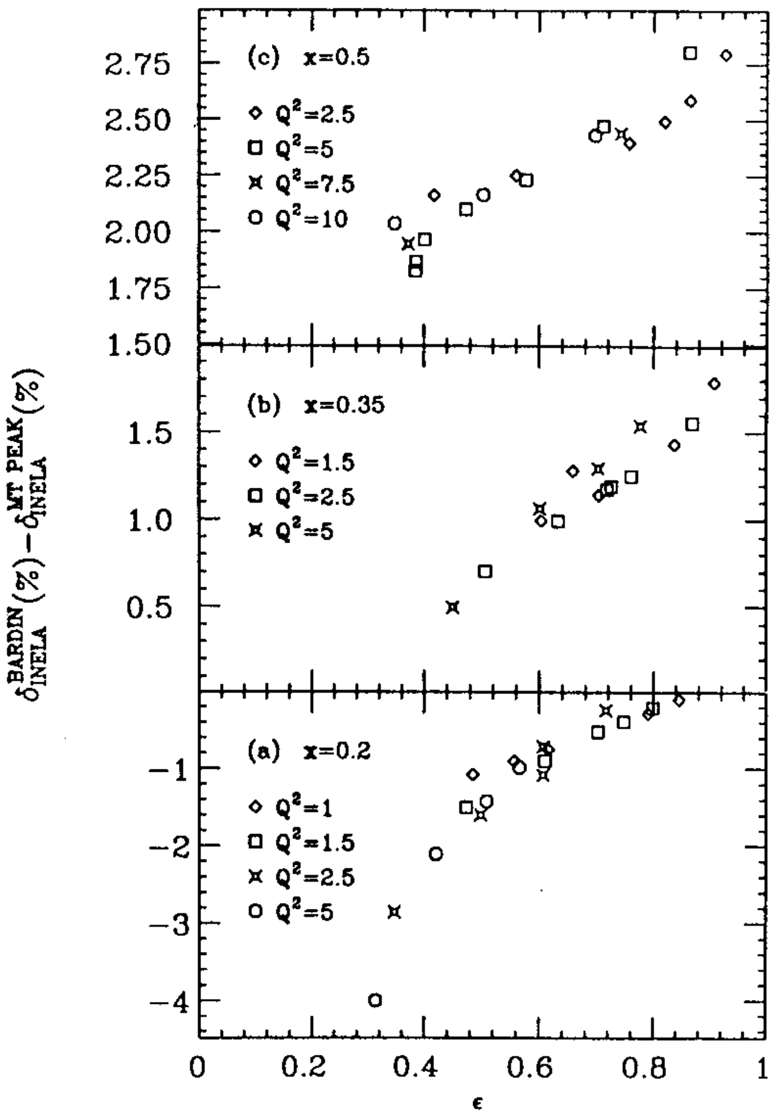

Figs. C.4 "Bardin" and "MT PEAK" inelastic "internal" δ's are compared. Difference in δ's (both in %) are plotted versus ϵ for all x,Q^2 points of our data set. The disagreement is upto 4% and is ϵ dependent. Note the x dependence of the difference.

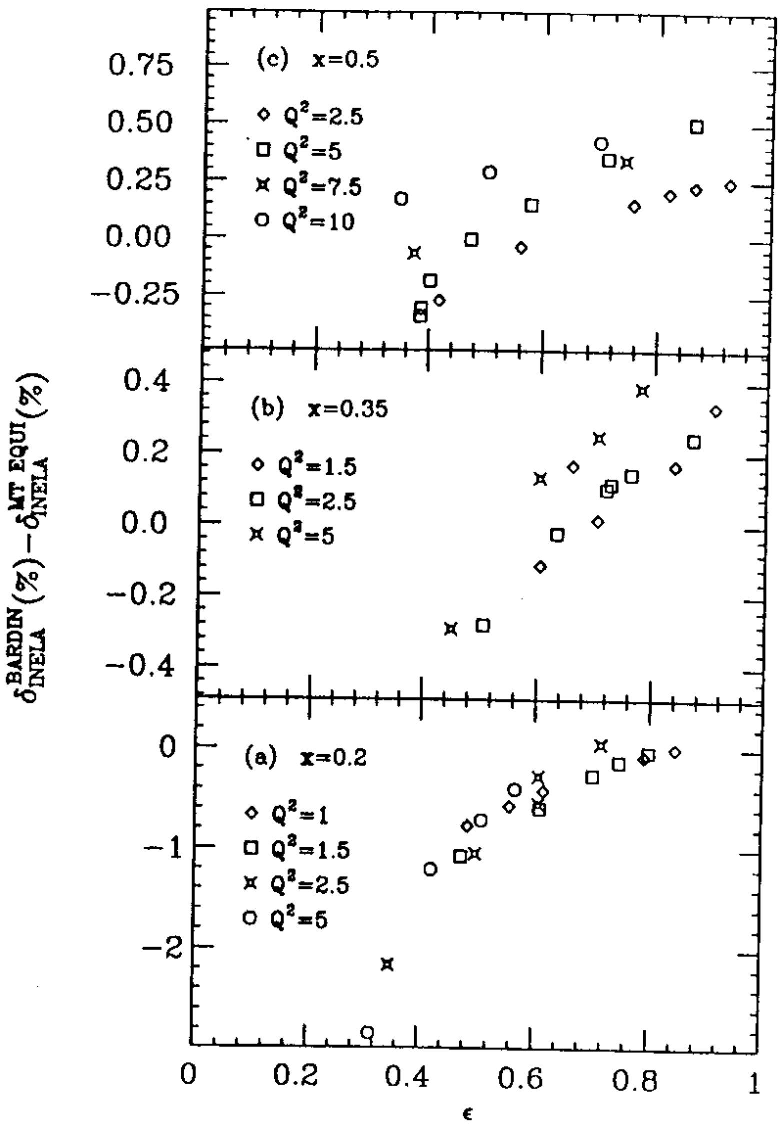

Figs. C.5 "Bardin" and "MT EQUI" inelastic "internal" δ's are compared. Difference in δ's (both in %) are plotted versus ϵ for all x,Q^2 points of our data set. The agreement is better than for "MT PEAK" calculations, for instance the strong x dependence of the differences are reduced. This effect is due to the inclusion of region D of Fig. C.1 in the integration. This effect should be more pronounced in "external" corrections, and therefore our modification of Tsai's original peaking approximations are an improvement.

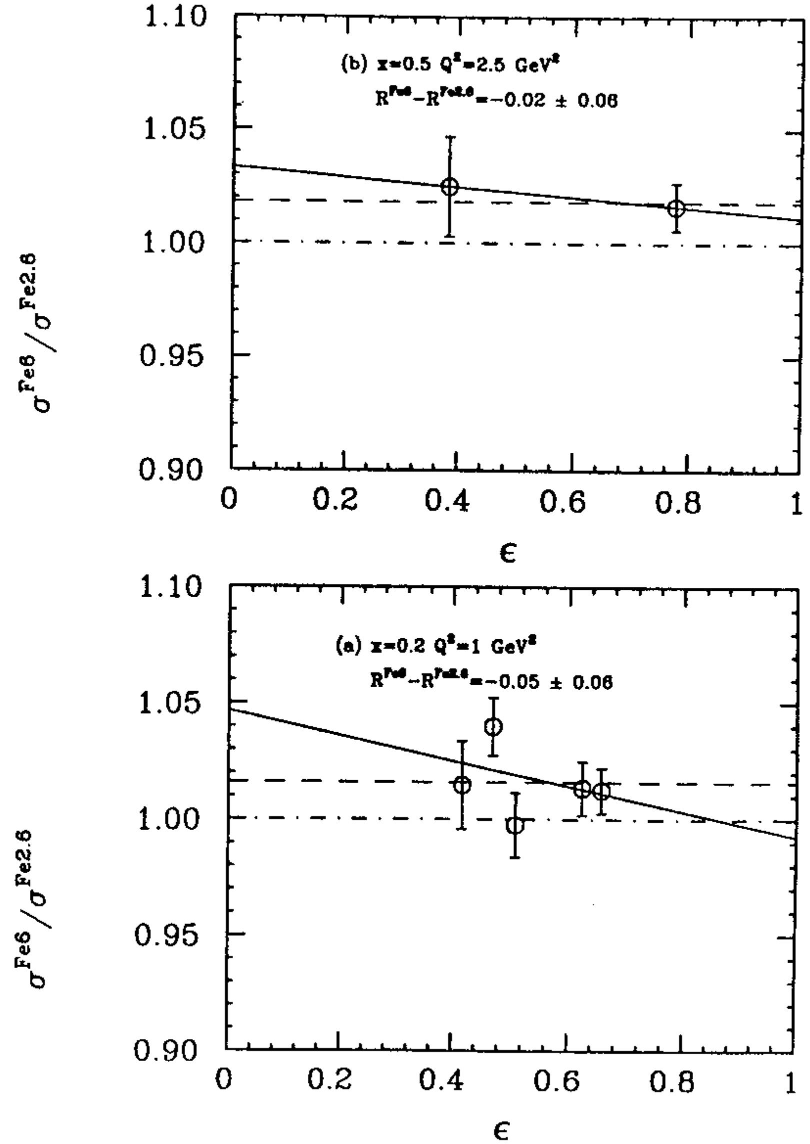

Figs. C.6 Our fits to ratio of cross sections for 6% and 2.6% radiation length Fe targets versus ϵ' are plotted. Only statistical errors are shown. On including a systematic uncertainty of ±1.5%, the results are consistent with unity. The R difference is consistent with zero. So we conclude that within our errors on this data we do not see any failure of "external" correction calculation program.

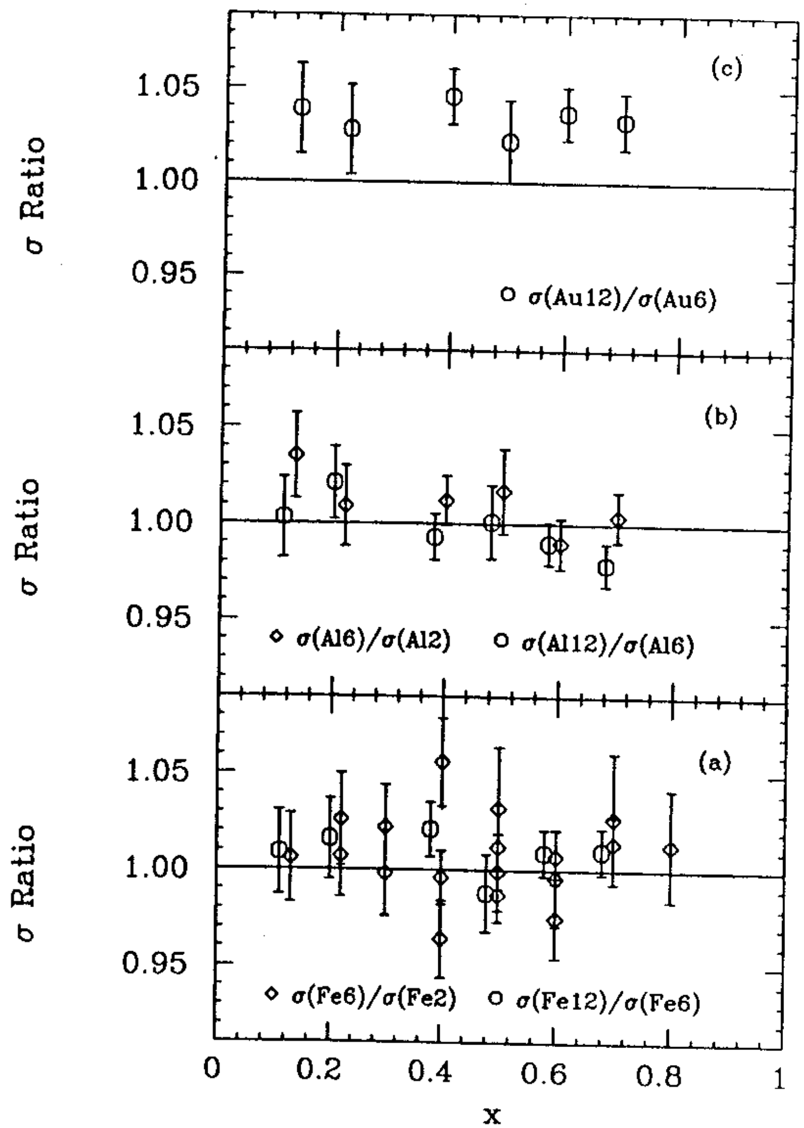

Figs. C.7 The ratios of SLAC-E139 cross sections for 6% to 2%, and 12% to 6% radiation length (a) Fe, (b) Al and (c) Au (only 12% to 6%) targets are plotted versus x. Results are consistent with unity. Only statistical errors are shown. Note that there is an additional uncertainty due to target thickness error (about 3% on Au data).

TABLE C.I

Magnitude of individual contributions to radiative corrections

D_2 target (2.6% radiation lengths) values only

Minimum and maximum values of $\delta=\sigma^{rad}/\sigma^{Born}$ are shown

QUANTITY	Minimum (%)	Maximum (%)
$\delta_{vac}=\delta^{l}_{vac}+\delta^{h}_{vac}$ †	3.301	5.076
"BARDIN"		
"Internal" corrections		
$\delta_{inel}=\sigma_{rad}/\sigma_{Born}-1$	-8.105	20.706
$\delta_{qel}+\delta_{el}$	0.190	8.420
δ_{had}	-1.560	-0.060
δ_{α^4}	-0.120	1.170
$\delta_{i}=\sigma_{i}/\sigma_{Born}$ (not in %)	0.926	1.262
"MT EQUI"		
"Internal" corrections		
δ_{inel}	-8.354	23.553
$\delta_{qel}+\delta_{el}$	0.048	9.550
"External" corrections		
δ_{inel}	-18.508	32.530
δ_{qel}	0.070	15.315
$\delta_{i+e}=\sigma_{i+e}/\sigma_{i}$ (not in %)	0.895	1.098
"Total" "BARDIN" + "MT EQUI"		
$\delta=\delta_{i}\ \delta_{i+e}$ (not in %)	0.828	1.383

†δ_{vac} is already included in δ_{inel}, δ_{qel} and δ_{el} values.

REFERENCES

[C.1] R. Von Gehlen, Phys. Rev. **118**, 1455 (1960); M. Gourdin, Nouvo Cimento **21**, 1094 (1961).

[C.2] (a) L. W. Mo and Y. S. Tsai, Rev. Mod. Phys. **41**, 205 (1969); (b) Y. S. Tsai, SLAC-PUB-848.

[C.3] A. Bodek et al., Phys. Rev. D **20**, 1471 (1979).

[C.4] M. Gari and W. Krumpelmann, Z. Phys. **A322**, 689 (1985).

[C.5] Y. S. Tsai, in Proceedings of the International Conference on Nuclear Structure, (1963), (Stanford University Press, Stanford, Ca, 1964) p.221.

[C.6] S. Stein et al., Phys. Rev. D **12**, 1884 (1975); R. G. Arnold et al., Phys. Rev. Lett. **52**, 724 (1984).

[C.7] J. J. Aubert et al., Phys. Lett. **121B**, 87 (1983).

[C.8] (a) A. A. Akhundov, D. Yu. Bardin and N. M. Shumeiko (ABS), Sov. J. Nucl. Phys. **26(6)**, 660 (1978);
(b) ABS, JINR preprint No. E2-10205;
(c) A. A. Akhundov, D. Yu. Bardin and W. Lohmann, JINR preprint No. E2-86-104;
(d) D. Yu. Bardin and N. M. Shumeiko, JINR preprint No. P2-10873.

[C.9] Y. S. Tsai, Proceedings of the Asia Pacific Physics Conference, (World Scientific Publishers, Singapore, 1983).

[C.10] See ref [C.8] (c). A model for hadronic scattering was taken from TASSO collaboration TASSO Note 192, (1982).

[C.11] Equations (2.8) of ref. [C.2](b)

[C.12] Ref. [C.8](b) gives a prescription for such cancellation.

[C.13] N. M. Shumeiko, Sov. J. Nucl. Phys. **29(6)**, 807 (1979).

[C.14] D. Yu. Bardin et al. Nucl. Phys. **B175**, 435 (1980); Nucl. Phys. **B197**, 1 (1982);

[C.15] Equation C.1 of ref. [C.2](b). See also Y. S. Tsai, Rev. Mod. Phys. **46**, 815 (1974) for radiation length definitions.

[C.16] J. J. Aubert et al., Z. Phys. **C22**, 341 (1984).

[C.17] J. G. Gomez, Ph. D. thesis, American University, (1987). The 12% radiation length data is unpublished, it has been used only for the "external" radiative corrections checks.

APPENDIX D TARGET MASS CORRECTIONS

Georgi and Politzer (GP) in their classic paper of 1976 [D.1], have made an attempt, within the framework of operator product expansion (OPE), to analyze deep inelastic structure functions at moderate values of Q^2 ($1 \leq Q^2 \leq 10$ GeV^2). The lowest order contribution to the expansion of the OPE coefficients, i.e. the free-field OPE leads to an approximate scaling of the structure functions in the variable ξ. Some of the important steps involved in their calculation are: (1) operator-product expansion of forward Compton amplitude, and keeping only terms with twist-2 operators, i.e. using bilinear combinations of quark fields only, (2) relate the appropriate coefficients of the OPE with the Nachtman moments of the structure functions, and (3) taking the the inverse Mellin transform of the moments to obtain structure functions. In the twist-2 calculation the step (2) leads to ξ-scaling feature. There has been a controversy regarding the step (3), which stems from the fact that the kinematic range of ξ is less than that of x at finite Q^2. The GP ξ-scaling formalism has been critisized [D.2] and defended [D.3] over the years.

Johnson and Tung [D.4] have suggested improvements to the ξ-scaling scheme which resolve mathematical inconsitencies in the original equations of Georgi and Politzer. Their equations for structure functions [D.4] are given by:

$$\tilde{F}_1^{JT}(x,Q^2) = \frac{\tilde{G}_1(\xi,Q^2)}{1+\xi^2 M^2/Q^2}, \tag{D.1}$$

$$F_2^{JT}(x,Q^2) = x^2 \frac{\partial^2}{\partial x^2}\Big[\zeta \int_\xi^{\xi_{th}} \frac{du}{u}\left(\frac{u}{\xi}-1\right) G_2(u,Q^2)\Big] \tag{D.2}$$

$$= x^2 \Big[\frac{\zeta}{\xi^2}\left(\frac{\partial\xi}{\partial x}\right)^2 \frac{G_2}{\xi} + \frac{\partial^2}{\partial x^2}\left(\frac{\zeta}{\xi}\right)\int_\xi^{\xi_{th}} du\, G_2(u,Q^2) - \frac{\partial^2\zeta}{\partial x^2}\int_\xi^{\xi_{th}} du \frac{G_2(u,Q^2)}{u}\Big], \text{ and} \tag{D.3}$$

$$R^{JT}(x,Q^2) = \frac{F_2}{2xF_1}(1+4M^2x^2/Q^2) - 1, \text{ where}$$

$$2x\tilde{F}_1^{JT}(x,Q^2) = 6xF_1^{JT} - \left(1+4M^2x^2/Q^2\right) F_2^{JT} \text{ and similarly for } \tilde{G}_1,$$

$$\zeta = \frac{x}{1+\xi^2M^2/Q^2}, \text{ Nachtman var. } \xi(x) = \frac{2x}{1+(1+4M^2x^2/Q^2)^{1/2}}, \text{ and } \xi_{th}=\xi(1).$$

These equations are identical to the Georgi and Politzer equations given in Chapter IV, with the replacement of the upper limits, in the expressions for the target mass integrals I_1 and I_2 on page 87, with ξ_{th}. The naive identification of the functions G_1 and G_2 with the QCD structure functions, $F_1^{QCD}(u,Q^2)$ and $F_2^{QCD}(u,Q^2)/u$ analogous to the GP scheme leads to very small modification of the final structure functions F_1 and F_2, because the contribution from the unphysical region $\xi_{th} \leq u,v \leq 1$ for the integrals I_1 and I_2 is small (See Fig. 1) Our data for F_1, F_2 and R are plotted on Figs. D.2-4, along with JT calculations (with this identification of functions $G_{1,2}$ with QCD structure functions), and the original GP calculations. As expected the Johnson and Tung results with this identification are not significantly different from Georgi and Politzer calculations, and are also in good agreement with our data.

However, Johnson and Tung identify the QCD structure functions with different functions $H_{1,2}$, which are functions of $\eta=\xi/\xi_{th}$. The relation between $H_{1,2}$ and $G_{1,2}$ is given by:

$$G_1(\xi,Q^2) = \theta(\xi_{th}-\xi)\ \tilde{H}_1(\eta,Q^2) \qquad (D.4)$$

Change of variables from u to $\eta'=u/\xi_{th}$ for the integral in (D.2) and use of (D.4) yields:

$$\tilde{F}_1^{JT}(x,Q^2) = \frac{\tilde{H}_1(\eta,Q^2)}{1+\xi^2M^2/Q^2}\ , \qquad (D.5)$$

$$F_2^{JT}(x,Q^2) = x^2\frac{\partial^2}{\partial x^2}\Big[\ \zeta\int_\eta^1\frac{du}{u}\left(\frac{u}{\eta}-1\right)H_2(u,Q^2\ \Big] \qquad (D.6)$$

where $\tilde{H}_1$ is defined in the same way as $\tilde{G}_1$. The identification of the functions $H_{1,2}$ with the QCD structure functions yield totally different results, and are also illustrated in Figs. 2-4. The reason such a drastic difference is due to the value of η, which is significantly larger than x and ξ for $Q^2 < 20\ \mathrm{GeV}^2$ (see Fig. 1). If the identification of $H_{1,2}$ with QCD structure functions is indeed the correct approach, these results seem to suggest that the dynamical effects, which could modify the above equations, are important.

Further theoretical studies of twist-2, and higher twist terms is needed to understand our data, and most other SLAC data for which power law violations of scaling are significant.

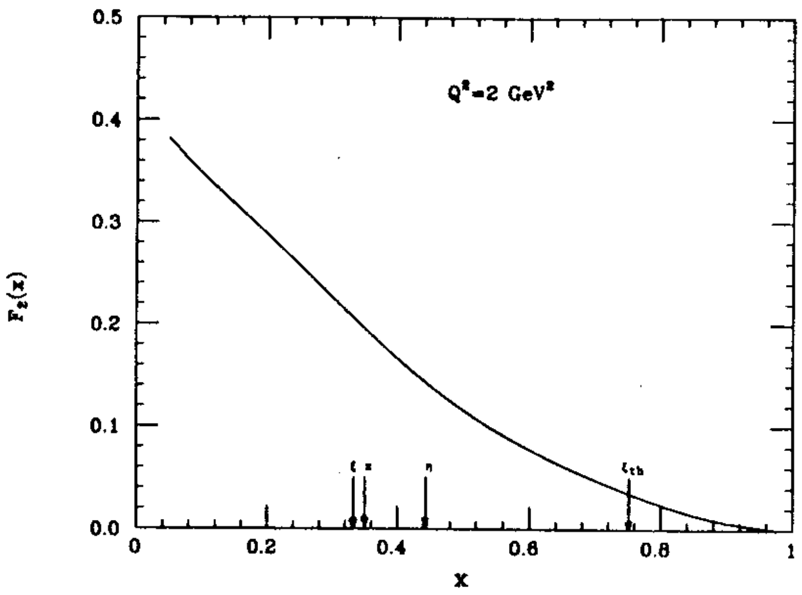

Fig. D.1 The QCD structure function F_2^{QCD} is plotted versus Bjorken x at $Q^2=2$ GeV^2. For x=0.35, the corresponding values of Nachtman variable ξ, the kinematic limit of ξ, i.e. ξ_{th}, and the Johnson-Tung variable $\eta=\xi/\xi_{th}$ are indicated. The integration in Georgi and Politzer's original method ranges from $\xi\longrightarrow 1$, whereas the correct limits of ξ are from $\xi\longrightarrow\xi_{th}$. The identification of the QCD structure function with the functions $G_{1,2}$ does not change the predictions for R, F_1 and F_2 because a) ξ is not significantly different from x, and b) the contribution from the region $x>\xi_{th}$ is small. Whereas the identification according to Johnson and Tung results in large differences because a) η is significantly larger than x, and therefore the constant term in the target mass expressions is small, and b) the integrals are also small.

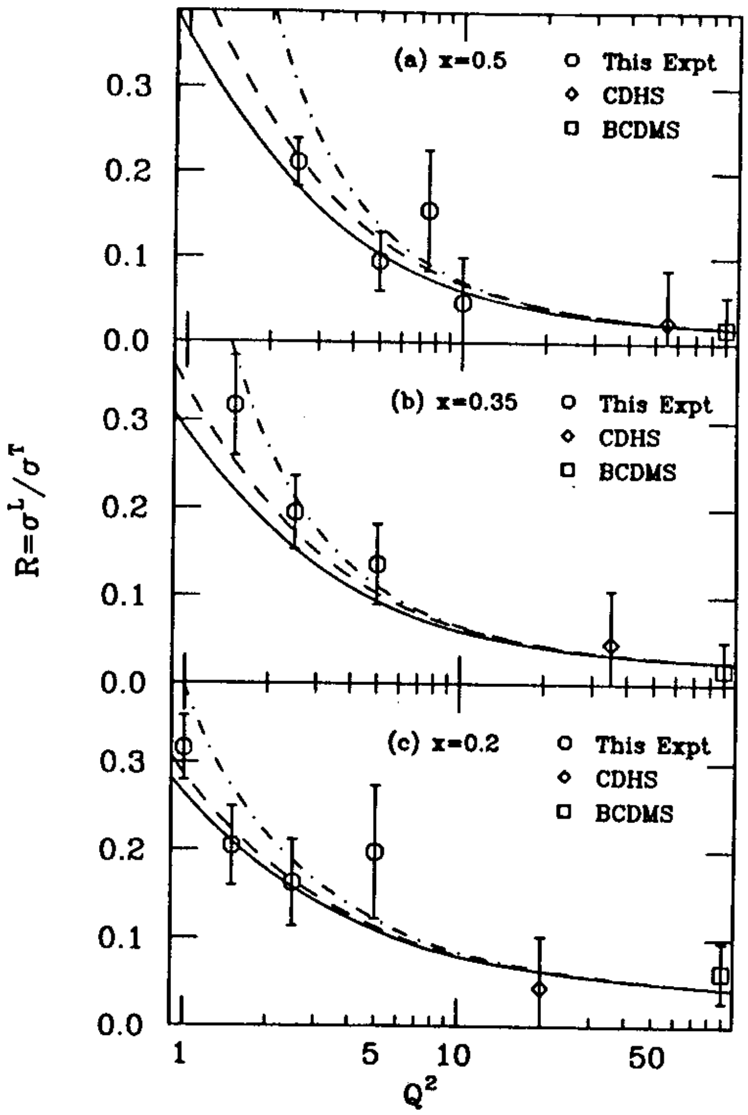

Figs. D.2 Georgi and Politzer (smooth curve), and Johnson and Tung calculations of target mass effects for R are compared to our data, where in the latter calculations QCD functions were identified with (i) $G_{1,2}$ (dash curve) and (ii) $H_{1,2}$ (dot-dash line).

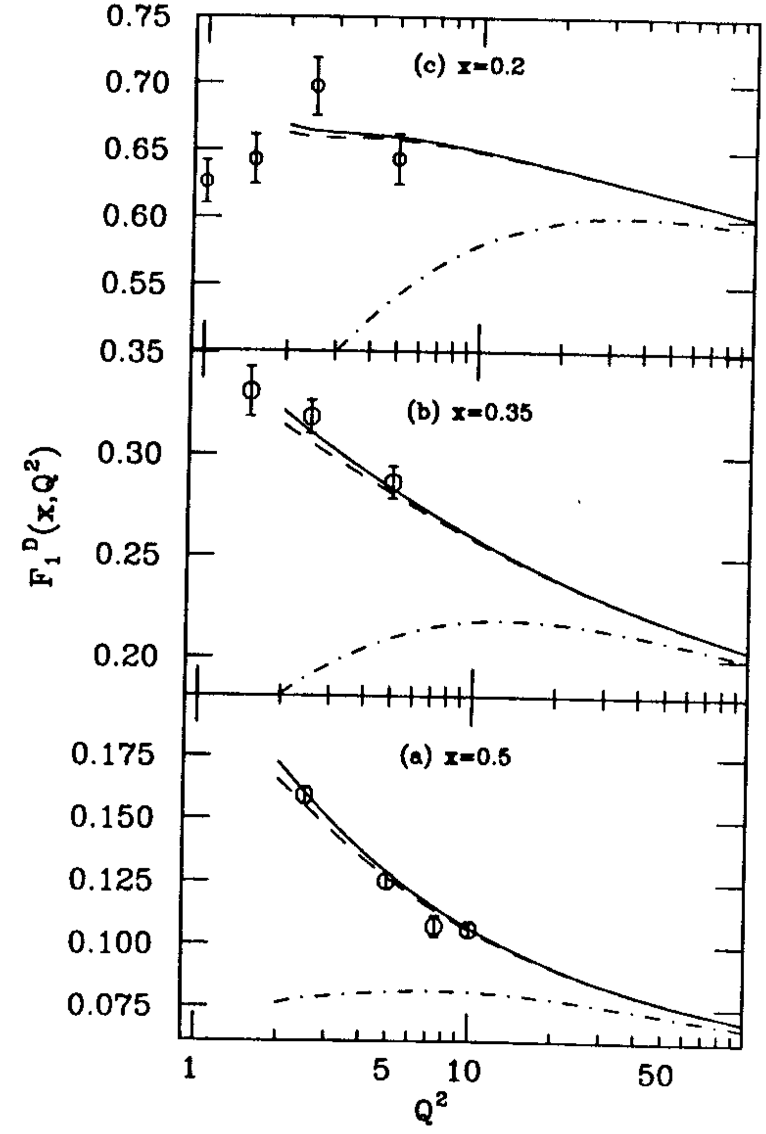

Figs. D.3 Georgi and Politzer (smooth curve), and Johnson and Tung calculations of target mass effects for F_1 are compared to our data, where in the latter calculations QCD functions were identified with (i) $G_{1,2}$ (dash curve) and (ii) $H_{1,2}$ (dot-dash line). The identification of QCD functions with $H_{1,2}(\eta,Q^2)$ results in a deviation of predictions from our data.

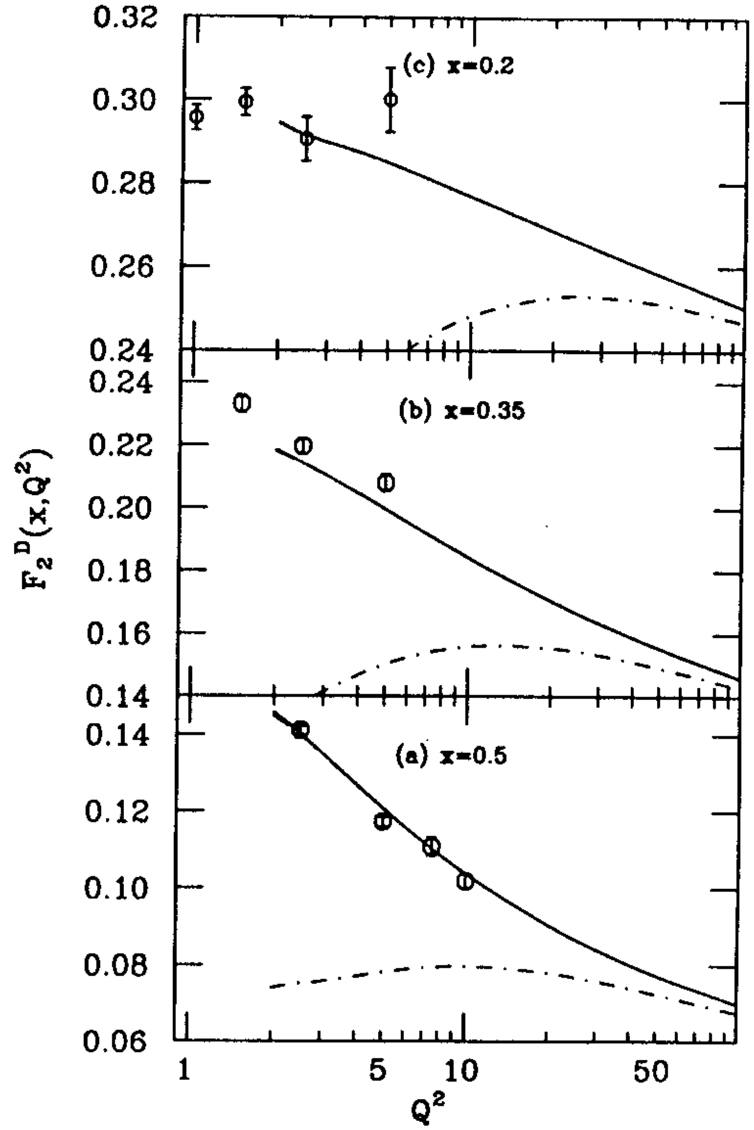

Figs. D.4 Georgi and Politzer (smooth curve), and Johnson and Tung calculations of target mass effects for F_2 are compared to our data, where in the latter calculations QCD function F_2^{QCD} was identified with (i) G_2 (dash curve) and (ii) H_2 (dot-dash line). The identification of QCD functions with $H_{1,2}(\eta,Q^2)$ results in a deviation of predictions from our data. The difference between GP and JT (i) curves is invisible in this scale.

REFERENCES

[D.1] H. Georgi and D. Politzer, Phys. Rev. **D14**, 1829 (1976).

[D.2] D. Gross et al., Phys. Rev. D15, 2486 (1977);

K. Bitar et al., Phys. Lett. **83B**, 114 (1979);

J. Miramontes and J. Sanchez Guillen, University of Santiago de Compostela (Spain) preprint no. US/FT-1/88 (1988).

[D.3] A. De Rujula et al., Phys. Rev. D15, 2495 (1977).

[D.4] P. Johnson and W. Tung, Neutrino '79 Proceedings, Bergen, Norway, (1979).